Title
Modeling and Simulations of electroenzymatic sensors in vitro and in the brain

Author
Clay, Mackenzie

Publication Date
2021

Peer reviewed|Thesis/dissertation

UNIVERSITY OF CALIFORNIA

Los Angeles

Modeling and Simulations of electroenzymatic sensors *in vitro* and in the brain

A dissertation submitted in partial satisfaction of the

requirements for the degree of Doctor of Philosophy

in Chemical Engineering

by

Mackenzie Simon Clay

2021

ABSTRACT OF THE DISSERTATION

Modeling and simulations of electroenzymatic sensors *in vitro* and in the brain

by

Mackenzie Clay

Doctor of Philosophy in Chemical Engineering

University of California, Los Angeles, 2021

Professor Harold Monbouquette, Chair

Mathematical modeling and simulations were employed to guide successfully the optimization of electroenzymatic biosensors for glutamate and for choline and to clarify how well such sensors can monitor rapid neurotransmitter signaling in the brain. Improvements in methods for accurate neurotransmitter detection in behaving animals are vital for the study of many neurological processes. However, the spatial and temporal resolution of even the most optimized sensors will be insufficient to record neurotransmitter dynamics directly *in vivo*, thereby causing potential confusion in the analysis of sensor data. Much of this confusion arises from the effects *in vivo* of both neurotransmitter mass transport and clearance on sensor recordings. These effects historically have been considered too complex or insignificant to investigate but must be included in the proper analysis of sensor data. Surprisingly, a chemical engineering approach for the analysis of mass transfer-influenced sensor kinetics has remained largely unexplored until now, where the value of the chemical engineering perspective is demonstrated through the study of electroenzymatic sensor performance *in vivo*.

To increase spatial and temporal resolution and minimize uncertainties in data analysis, a model of an electroenzymatic glutamate sensor was used to reveal the theoretical limits of sensor performance and to suggest biosensor modifications that led to a six-fold increase in sensitivity to 320 nA μM^{-1} cm^{-2} and an order-of-magnitude reduction in intrinsic response time (in the absence of external mass transfer limitations) to 80 ms while maintaining excellent selectivity. However, the improved response times were still an order of magnitude slower than the simulated response time at optimal sensitivity. Due to the importance of sensor response times for the proper analysis of data collected from measurements of transient glutamate release events in the brain, the difference in these response times was investigated with an adapted mathematical model that accounts for noncatalytic, reversible binding of glutamate to the proteins within the sensor immobilized enzyme coating. With reasonable parameter estimates, the new model was shown to fully resolve the prior discrepancy in sensor response time, and a set of future experiments was proposed to confirm the significance of this phenomenon.

The sensor apparent K_m, which is a measure of the linear calibration range, was shown to be influenced by O_2 diffusion into the enzyme coating at relatively high glutamate concentrations rather than to be reflective of the immobilized enzyme kinetics, as was commonly believed. Such oxygen limitation is observed when bulk O_2 concentrations are less than 33% of the local glutamate concentration. Similar simulations of choline sensors led to highly selective choline sensors with the improved sensitivity and intrinsic response time of 660 $\pm$ 40 nA μM^{-1} cm^{-2} and 360 ± 50 ms, respectively. It also was determined that O_2 may become limiting for bulk O_2 concentrations <60% of the local choline concentration.

Simulations of glutamate sensor response to glutamate transients showed that optimized sensors would have difficulty resolving Gaussian shaped transient glutamate concentrations present for <40 milliseconds *in vitro* and that optimized sensors *in vivo* may provide improved

temporal resolution, although they are not likely to respond to glutamate concentration changes >30 μm from the sensor surface due to diffusional mass transfer limitations and glutamate uptake from the brain extracellular space. Detailed analysis of sensor response *in vivo* showed that variability in the possible rate of H_2O_2 clearance from brain extracellular space could result in a sensor recording that exceeds by 300% the value expected from sensor calibration *in vitro*. It was also shown that apparent response times could be significantly slower *in vivo* than *in vitro* due primarily to slow diffusion in the brain and that the decay in sensor response is not reflective of glutamate uptake rates in any meaningful way without extensive contextual details. Three-dimensional models additionally served to provide insight into the role of electrode size and enzyme deposition area in adequately detecting glutamate release from precisely defined and localized increases in neuronal activity, representative of typical changes in neuron firing frequencies. These results highlighted the benefits of sensor miniaturization and suggested probe design modifications to improve spatial resolution and detect glutamate release from smaller populations of active synapses.

Modeling and simulations of electroenzymatic sensors *in vivo* have demonstrated the value in bringing a chemical engineering approach to bear on the optimization of such sensors and on the interpretation of sensor recordings. Further, detailed mathematical modeling that includes descriptions of chemical dynamics with mass transfer equations could prove broadly valuable in future neuroscience research.

The dissertation of Mackenzie Simon Clay is approved.

Nigel Maidment

Yi Tang

Samanvaya Srivastava

Harold Monbouquette, Committee Chair

University of California, Los Angeles

2021

Table of Contents

LIST OF FIGURES

LIST OF TABLES

ACKNOWLEDGEMENTS

Foremost, I would like to acknowledge my advisor, Professor Harold Monbouquette, for all of the contributions he made to this work as well as for all of the guidance, support, and opportunities he gave me over the past number of years. I struggled early in my doctoral studies and would not be completing this Ph.D. if not for his faith in me and his compassion. In time, I learned from him how to maintain my excitement for academic research and how to write with a more honed, scientific precision that I will carry with me into my future academic career. I am also grateful to have been given the opportunities to TA for him in multiple courses, which greatly inspired me as a researcher and teacher, and for being given the opportunities to attend multiple scientific conferences with his support and example to guide me.

I would also like to acknowledge the rest of my doctoral committee, both current and past, Professors Nigel Maidment, Yi Tang, Samanvaya Srivastava, and James Liao, for helping to guide my doctoral studies, for supporting me after conference presentations, and for supporting me in funding applications and in applying for future research positions. Each of them, at different times, helped me feel welcome and appreciated on campus, which I also feel very thankful for.

The other professors I worked under as a TA also have my gratitude: professors Carissa Eisler and Dante Simonetti. I have greatly enjoyed my time as a TA and learned a great deal about teaching along the way.

I'd also like to acknowledge my fellow lab members, Brenda Huang, Bo Wang, Bonhye Koo, Zhenrong Zheng, Yan Cao, Allison Yorita, and Lili Feng, for their support and contributions to this work.

I would additionally like to thank my friends and close caregivers who have gone to extraordinary lengths to help me in my time as a graduate student: Dominic Syracuse, Tom Oberhofer, Gary Murakami, Jenn Smith, Dominique Mhoon, Nick Knutson, and Justin Smalls.

Finally, I am most deeply grateful for the support my family has given me. Making it to this point in my career feels unreal to me, and I cannot imagine having gotten here without their tremendous support. Part of my gratitude comes from knowing how much I asked of them; living with a spinal cord injury, especially one like mine, is not easy. Mostly, I am thankful for their unwavering support and presence in my life. Spending the last year (the COVID-19 pandemic) with my parents, Carol and Mike, my twin brother Cam, and his wife Ahna in Seattle has been an unexpected blessing and I am especially thankful for their support and encouragement as I worked to complete my Ph.D. and apply for faculty positions and postdoctoral scholarships. I am also thankful for my sister Alexis, her husband Sam, and their daughter Anaïs, who were welcome sights on zoom calls over the past year.

VITA

2011 B.Sc., Chemistry, Minor in Mathematics
Seattle University
Seattle, WA

2012-2021 Graduate Student Researcher
UCLA Department of Chemical and Biomolecular Engineering
Los Angeles, CA

2015-2021 Teaching Assistant
UCLA Department of Chemical and Biomolecular Engineering
Los Angeles, CA

PUBLICATIONS AND PRESENTATIONS

M. Clay, H.G. Monbouquette. "Simulated performance of electroenzymatic glutamate biosensors *in vivo* illuminates the complex connection to calibration *in vitro*" (to be submitted to *ACS Chem. Neurosci*. 2021)

I.W Huang,* **M. Clay**,* H.G. Monbouquette. 2020. "Electroenzymatic choline sensing at near the theoretical performance limit" *Analyst **2021,** 146 (3), 1040-1047*. *co-authors

I.-W. Huang, **M. Clay**, S. Wang, Y. Guo, J. Nie, H.G. Monbouquette. 2020. "Electroenzymatic glutamate sensing at near the theoretical performance limit" *Analyst* **145**, 2602-2611

M. Clay, H.G. Monbouquette. 2018. "A detailed model of electroenzymatic glutamate biosensors to aid in sensor optimization and in applications *in vivo*" *ACS Chem. Neurosci.* **9**(2):241–51

Langenhan, J. M.; McLaughlin, R. P.; Loskot, S. A.; Rozal, L. M.; **Clay, M. S**.; Alaimo, P. J. 2016. "Using density functional theory to calculate the anomeric effect in hydroxylamine and hydrazide derivatives of tetrahydropyran" *J. Carbohydr. Res. **35***, 106-117.

M. Clay, "Simulation of Chemical Transport and Signaling in the Brain," Meet the Faulty Candidates Poster Session, *AIChE Annual Meeting: San Francisco (online)*, 2020

M. Clay, H.G. Monbouquette, "Optimization of electroenzymatic biosensors for neurotransmitters & Simulation of sensor response in vivo to enable proper interpretation of data," Sensors Session, *AIChE Annual Meeting: San Francisco (online)*, 2020

M. Clay, H.G. Monbouquette, Poster Session, *Monitoring Molecules in Neuroscience Biennial Meeting*, Oxford UK, 2018

M. Clay, H.G. Monbouquette, “Model of Electroenzymatic Glutamate Biosensors to Aid in Sensor Optimization and in Applications in vivo,” Biosensors, Biodiagnosis and Bioprocess Monitoring II (oral), *AIChE Annual Meeting: Minneapolis, MN,* 2017

M. Clay, I.-W. Huang, H.G. Monbouquette, “Simulation-Guided Optimizations of Electroenzymatic Biosensors to Monitor Glutamate in Vivo,” *UCLA BRI Neuroscience Poster Session*, 2017

M. Clay, H.G. Monbouquette, “Model of Electroenzymatic Glutamate Biosensors to Aid in Sensor Optimization and in Applications in vivo,” UCLA Chemical Engineering 4th Year Symposium, 2017

M. Clay, H.G. Monbouquette, “Mathematical Model to Optimize Electroenzymatic Microbiosensors for the Monitoring of Glutamate Signaling in the Brain,” *Analytical Neuroscience Session* ACS Annual Meeting: San Francisco, CA, 2017

AWARDS AND DISTINCTIONS

2011	Outstanding Senior Chemistry Major, Seattle University
2012	UCLA Eugene Cota-Robles Fellowship *Promoting diversity in PhD students pursuing academic careers.*
2018	UCLA Inaugural Eudaimonia Award *One of 7 awards given to UCLA community members for exemplifying lives of purpose and meaning.*

Chapter 1: Introduction

1.1 Motivation

The brain employs a fascinating and complex system of coordinated chemical and electrical signals that originate from the interplay of chemical transport and reaction rates. Much remains unknown about these signaling pathways, particularly within the contexts of neurological damage or disease, which has prompted the invention of numerous electrical, chemical, and optical sensing techniques.[1-5] Each technique and design is intended to measure a particular aspect of neurotransmission, which is necessary considering the complexity of neurological systems; resolution is often desired at micrometer length scales and millisecond time scales.[6-8] Electroenzymatic biosensors, which rely on enzymes for selective neurochemical analyte recognition and on electrochemical signal transduction, provide the best spatiotemporal resolution for chemical sensing but have been limited to electrode sizes >6000 μm^2 (large enough to maintain distinguishable responses) and reported response times of ~1 s.[2] Improvements to these sensors are needed for the electrochemical sensing of prominent neurochemicals to reach desired levels of accuracy and resolution, and understanding the theoretical performance limits of such sensors is instrumental in developing optimized designs. With non-ideal spatiotemporal resolution, these sensors are still tremendously useful,[9] although it has remained unclear how well they record the actual chemical dynamics in the brain due to their present spatiotemporal resolutions. Improper analysis of data collected by sensors with non-ideal spatiotemporal resolution can lead to underestimates of transient concentrations and to a distorted picture of their concentration time-course in the brain. These concerns have not been addressed rigorously in the literature to date, limiting the conclusions that can be definitively drawn from experimental studies.

Both sensor optimization and analyses of *in vivo* performance can be greatly aided by detailed mathematical modeling and simulations based on fundamental mass transport equations, which historically have been constrained to simplified studies of glucose sensors,

often without modeling time dependence (including sensor response time) or considering the dynamic environment in which the sensor is used. With commercial partial differential equation solvers based on the finite element technique, sensor performance can be simulated by modeling chemical transport and reaction rates with full control over model parameters and in unprecedented detail. This control enables theoretical optimization to sensor design and simulations of sensor responses to be done under any environmental conditions, including simulations of sensor calibrations (*in vitro*) and after implantation (*in vivo*). The work presented here has the potential to revolutionize how the biological data gathered by numerous types of sensors is analyzed, in many cases where neuroscientists working with sensors have not attempted to consider how mass transport influences sensor response. This will provide a much clearer understanding of actual neurochemical dynamics and the processes governing them. Improving our understanding of the chemical processes of the brain and nervous system is fundamental to understand the brain in neurological development, deteriorative aging, motor and sympathetic functions, and also in cases of neurological damage and disease.

1.2 Sensor operation and characterization

When a neurotransmitter is released into a synapse or the extracellular space of the brain it joins a complex mixture of compounds and macromolecules, and its concentration quickly diminishes due to a combination of diffusion through the tortuous extracellular space and the biological uptake and clearance mechanisms present in brain tissue. To detect released neurotransmitters, sensors must be placed close to the location of their release so that they may be detected after minimal reductions in concentration due to diffusion, they must have high sensitivities and low detection limits to distinguish between sensor signal and noise, they must be selective against the many other compounds in the extracellular fluid, and they must have a fast enough response time to measure the neurotransmitter concentration before it dissipates, is taken up by nearby cells, or is degraded. Multiple types of electrochemical sensors and

operation procedures have been used, although in many cases electroenzymatic sensors operated under constant potential amperometry offer the best resolution and specificity, further being able to detect non-electrooxidizable compounds through the clever use of an immobilized enzyme. Electroenzymatic sensors are often designed as single wire probes or as microelectrode arrays,[2] with arrays having an advantage in spatial resolution, in the possibility of monitoring multiple neurochemicals in roughly the same location, and in the option to include an on-probe reference electrode, which removes the need for a separate reference electrode probe thereby significantly reducing noise.[10]

Electroenzymatic sensors, including those for glutamate (Glut) and choline (Chol), operate as specialized electrochemical sensors that can be placed anywhere in the brain where probes can be inserted and can continuously monitor concentrations when operated with constant potential amperometry. Immobilized enzyme and polymer coatings are deposited on the sensor surface and are fundamental to the mechanism of sensing neurochemicals with specificity. Immobilized oxidase enzymes, e.g., glutamate oxidase, are bound to the sensor in an outer coating and will specifically catalyze the oxidation of the analyte of interest. This produces a quantifiable byproduct, e.g. H_2O_2 in the case of glutamate oxidase, that can be readily oxidized by the underlying electrode to produce a current, thereby allowing for the sensing of a non-electrooxidizable species such as Glut. Under ideal circumstances, the current produced is proportional to the initial analyte concentration. Sensor response is often converted to a concentration measurement through the use of a pre-determined calibration factor unique to the sensor; an accurate calibration factor or calibration curve (if response is within a non-linear regime) is vital for data analysis. Since other biomolecules may be electroactive and may react with the underlying electrode to give a current signal, permselective polymers generally are deposited first on the electrode surface (under the immobilized enzyme layer) to improve selectivity through size and charge exclusion of these potentially interfering species.

Sensors are characterized by their sensitivity, selectivity, detection limit, response time, and lifetime or stability, although these properties are not always reported in entirety or in the same manner. Generally, characteristics are determined *in vitro* at (~37° C). Sensitivity can be defined in units of nA/μM/cm^2, although sensitivities are often given in equivalent units or as the calibration factor itself (in units analogous to nA/μM). The detection limit is defined as the analyte concentration that results in a signal that is 3x that of the background noise, meaning that reported values of detection limits can be misleading (noise filtering methods could affect the detection limit, and this is not necessarily a property of the sensor itself). Response times are typically measured as the time required for sensor response to climb to 90% of the maximum sensor response to a step-change in analyte concentration. Selectivity refers to the response of a sensor to the target analyte relative to potentially interfering species.

All of these properties depend on the polymer and enzyme coatings. Differences in the porosities, effective diffusivities, thicknesses, and concentration of active enzyme in the coatings can have a large effect on sensor characteristics, and many polymer films and immobilization techniques have been employed to improve sensors through trial-and-error processes.[2] The state-of-the-art technique in the Monbouquette Group involves electrodeposition of poly-phenylenediamene followed by dip-coating in Nafion and enzyme immobilization using a PDMS stamp or manual deposition of droplets onto sensor sites (immobilization is accomplished using a bis(sulfosuccinimidyl)suberate or glutaraldehyde crosslinker).[11-14] Polymer coatings must be thick enough to block interferents from reaching the underlying electrode and enzyme coatings must be thick enough (and with a high enough concentration of immobilized enzyme) to turnover analyte at a rate sufficient to generate a measurable signal. Thicker coatings lead to higher selectivity and are less dependent on maintaining the functionality of the enzyme over time, making them more durable. However, thicker coatings lead to an increased mass transfer resistance, which reduces sensitivity and increases response time. Optimized sensors will have high sensitivities so that sensing sites can be miniaturized (improving spatial resolution) and fast

response times (improving temporal resolution), requiring a careful balancing of layer thicknesses.

1.3 Modeling electroenzymatic sensors *in vitro*

Partial differential equations can be used to describe the diffusion and reaction of the important chemical species within the porous spaces in the sensor coatings that underlies the sensing of neurotransmitters. We assume that the approximations required for the use of Fick's law of diffusion are valid. This includes the assumption that concentrations are dilute, that the pores are large enough that molecular mean free paths are not affected by pore walls, and that the coating can be considered homogeneous. Models must describe Glut, O_2, and H_2O_2 for Glut sensors and Chol, O_2, and H_2O_2 for Chol sensors. Concentrations of these species provide the minimum number of dependent variables needed to simulate Glut and Chol sensor performance in terms of the enzymatically catalyzed production of H_2O_2 from Glut or Chol and O_2 and the electrooxidation of H_2O_2 on platinum electrodes. Equation 1.1 is the 1-dimensional description of the relevant diffusion and reactions, with dependent variables representing the concentrations of each chemical species C_i (i = Glut or Chol, O_2, and H_2O_2) within the void space of coating j. Each term (the accumulation, diffusion, and reaction terms) in the equations has units describing the change in concentration over time in the coating (μM/s), prompting the inclusion of the void fraction parameters ε_i to properly relate the overall volume concentration in terms of the void space concentration. The tortuosity and porosity of the coatings reduces effective diffusion coefficients within the coating, requiring the inclusion of α_j parameters to modify the molecular diffusivity in aqueous solution D_i to represent the effective diffusivity within the coating for driving forces related to gradients in C_i. These α_j parameters can be found experimentally or approximated by theoretical relations to known parameters, such as a random pore model.[15] If there is a reaction within the coating, such as the enzymatic turnover of Glut or Chol, it is given

by $r_{i,j}$ with the appropriate adjustment to ensure the term represents the concentration change over time within the volume of the sensor coating.

$$\varepsilon_j \frac{\partial C_i}{\partial t} = -\alpha_j D_i \frac{\partial^2 C_i}{\partial x^2} + r_{i,j} \quad (1.1)$$

Numerical solutions to these sets of partial differential equations provide concentration profiles over the spatial domains of the coatings as a function of time. Spatial concentration profiles at specific times provide insight into the factors affecting sensor response (such as the effect of diffusive resistance within a sensor coating), the efficiency of the sensor in detecting the H_2O_2 produced, and the current produced at the electrode surface (depending on the flux of H_2O_2 at the electrode surface is defined by Equation 1.2, where *F* is Faraday's constant, *A* is the electrode area, and the factor of 2 accounts for the two electrons generated for each molecule of H_2O_2 electrooxidized). Solving the partial differential equations for the time-dependent sensor response and concentration profiles also requires boundary conditions within the sensor coatings and at the enzyme/solution boundary and initial conditions that define what process is being simulated. Between coatings, equal flux conditions are appropriate given the conservation of mass constraint along with equal or partitioned concentrations, as appropriate. Initial conditions and the condition at the enzyme/solution boundary may vary depending on what is to be simulated. For a step-increase in exogenous analyte concentration outside the sensor from 0 to 10 μM within a well-stirred beaker, appropriate initial conditions within the sensor would specify the bulk solution values and the outer boundary condition would specify convective mass transfer in the form of Equation 1.3. It can be useful to estimate mass transfer coefficients for certain species based on the value of a well-known species coefficient, as described by Equation 1.4.[16]

$$\text{current} = 2FA\alpha_j D_{H_2O_2} \frac{\partial C_{H_2O_2}}{\partial x} \quad (1.2)$$

$$\alpha_j D_i \frac{\partial C_i}{\partial x} = m_i\left(C_{i,s} - C_i\right) \quad (1.3)$$

$$m_i = \left(\frac{D_i}{D_{H_2O_2}}\right)^{2/3} m_{H_2O_2} \quad (1.4)$$

Mathematical models of this type have rarely been constructed for the analysis of biosensors for neurotransmitters, and have often been based on significant assumptions that limit the accuracy and informativeness of model simulations. Further description of previous modeling efforts is provided in Chapter 2, along with the preliminary results of a much more comprehensive 1-dimensional model of electroenzymatic sensors for Glut. Chapter 3 details a refinement of the model with the experimental verification of numerous parameters and the successful application of it towards Glut sensor optimization, resulting in unprecedented improvements to sensitivity and response time. Chapter 4 presents a hypothesis to explain better both theoretical and experimental sensor responses by considering reversible adsorption of neurotransmitters to the proteins constituting the sensor's enzyme coating. Chapter 5 extends the sensor model to simulate Chol sensors, showing the broad applicability of the model for simulating multiple types of sensors and in the subsequent optimizations of such sensors.

1.4 Modeling electroenzymatic sensors *in vivo*

Perhaps the most useful application of an electroenzymatic sensor model is in simulating how well sensors perform in response to real neurological dynamics within the environmental conditions of the brain. Due to differences in the temporal resolution of a Glut sensor and the temporal resolution required to measure synaptic Glut release, it can be inferred that sensor

response will be less than or equal to what it might be *in vitro*, when responding to the same bulk Glut concentration. The extent to which signal is reduced and resolution is lost has remained unspecified, leading to the current operating method of ignoring such complications when interpreting data and considering sensor response only in comparison to responses at different times; thus quantitative measurements are difficult to justify and are often not reported with properly validated accuracy. To realistically model Glut sensor response to *in vivo* conditions, a detailed mathematical description of the brain volume exogenous to the sensor must be included, which introduces a large number of unknown parameters and complications which require additional, careful assumptions about neurotransmitter dynamics. These assumptions require referencing (in great depth) the previous findings of experimental studies and cleverness in mathematically describing neurotransmitter release and in considering how spatiotemporal inconsistencies in diffusion parameters and reaction rates (also depending on the region of the brain) can be simulated.

General modeling of chemical transport in the extracellular space of the brain follows the pioneering works of Nicholson and Hrabetova, who have firmly established the concept of using diffusion, reaction, and convection equations to model the brain.[17] Continued work with these equations to study sensor recordings of neurological dynamics is a natural extension of this work. Our ever-increasing ability to model complex systems (due to the continued development of the hardware and software used to find numerical solutions to partial differential equations) makes this a promising direction for sustained, future research. The diffusion and reaction equations developed by Nicholson et al. are similar to those in Equation 1.1, although the effective diffusivity in the brain is defined using the void fraction in the brain ($\varepsilon_b = 0.2$) and tortuosity ($\lambda = 1.6$). Since Glut and H_2O_2 are naturally removed from extracellular space, it is necessary to include the relevant Glut uptake and H_2O_2 clearance rates, possibly as first-order reactions as described by Equation 1.6.

$$\varepsilon_b \frac{\delta C_i}{\delta t} = \frac{\varepsilon_b}{\lambda^2} D_i \frac{\delta^2 C_i}{\delta x^2} + \varepsilon_b r_i(C_i) \quad (1.5)$$

$$r_i(C_i) = k_i C_i \quad (1.6)$$

Initial methods to simulate sensor response *in vivo* and to address the challenges in modeling neurological systems are explained in full detail in Chapter 6. The initial goals of this work are to quantify sensor response to differences in environmental conditions *in vitro* and *in vivo* and to provide an estimation of sensor spatial resolution. Further development of the model to 3 dimensions is detailed in Chapter 7, where different enzyme immobilization strategies (droplet-coating *vs* stamping) and sensor miniaturizations are investigated for optimal sensor performance in response to precisely defined increases in neuronal activity within regions of varied sizes, localized near the sensor surface.

1.5 References

1. Hong, G. S.; Lieber, C. M., Novel electrode technologies for neural recordings (vol 20, pg 330, 2019). *Nat Rev Neurosci* **2019,** *20* (6), 376-376.
2. Weltin, A.; Kieninger, J.; Urban, G. A., Microfabricated, amperometric, enzyme-based biosensors for in vivo applications. *Anal Bioanal Chem* **2016,** *408* (17), 4503-4521.
3. Clark, H.; Monaghan, J.; Yang, H. R.; Xia, J. F.; Mu, M.; Lovely, A.; Micovic, N., SPARC_A DNA-based optical nanosensor for in vivo imaging of acetylcholine in the peripheral nervous system. *Faseb J* **2020,** *34*.
4. Di, W. J.; Clark, H. A., Optical nanosensors for in vivo physiological chloride detection for monitoring cystic fibrosis treatment. *Anal Methods-Uk* **2020,** *12* (11), 1441-1448.
5. Marvin, J. S.; Borghuis, B. G.; Tian, L.; Cichon, J.; Harnett, M. T.; Akerboom, J.; Gordus, A.; Renninger, S. L.; Chen, T. W.; Bargmann, C. I.; Orger, M. B.; Schreiter,

E. R.; Demb, J. B.; Gan, W. B.; Hires, S. A.; Looger, L. L., An optimized fluorescent probe for visualizing glutamate neurotransmission. *Nat Methods* **2013,** *10* (2), 162-170.

6. Scimemi, A.; Beato, M., Determining the Neurotransmitter Concentration Profile at Active Synapses. *Mol Neurobiol* **2009,** *40* (3), 289-306.
7. Ribrault, C.; Sekimoto, K.; Triller, A., From the stochasticity of molecular processes to the variability of synaptic transmission. *Nat Rev Neurosci* **2011,** *12* (7), 375-387.
8. Keighron, J. D.; Wang, Y.; Cans, A. S., Electrochemistry of Single-Vesicle Events. *Annu Rev Anal Chem (Palo Alto Calif)* **2020,** *13* (1), 159-181.
9. Wassum, K. M.; Tolosa, V. M.; Tseng, T. C.; Balleine, B. W.; Monbouquette, H. G.; Maidment, N. T., Transient Extracellular Glutamate Events in the Basolateral Amygdala Track Reward-Seeking Actions. *J Neurosci* **2012,** *32* (8), 2734-2746.
10. Tolosa, V. M.; Wassum, K. M.; Maidment, N. T.; Monbouquette, H. G., Electrochemically deposited iridium oxide reference electrode integrated with an electroenzymatic glutamate sensor on a multielectrode array microprobe. *Biosens Bioelectron* **2013,** *42*, 256-260.
11. Huang, I. W.; Clay, M.; Wang, S.; Guo, Y.; Nie, J.; Monbouquette, H. G., Electroenzymatic glutamate sensing at near the theoretical performance limit. *Analyst* **2020,** *145* (7), 2602-2611.
12. Wang, B.; Koo, B.; Huang, L. W.; Monbouquette, H. G., Microbiosensor fabrication by polydimethylsiloxane stamping for combined sensing of glucose and choline. *Analyst* **2018,** *143* (20), 5008-5013.
13. Wang, B.; Koo, B.; Monbouquette, H. G., Enzyme Deposition by Polydimethylsiloxane Stamping for Biosensor Fabrication. *Electroanal* **2017,** *29* (10), 2300-2306.
14. Huang, I. W.; Clay, M.; Cao, Y.; Nie, J.; Guo, Y.; Monbouquette, H. G., Electroenzymatic choline sensing at near the theoretical performance limit. *Analyst* **2021,** *146* (3), 1040-1047.

15. Wakao, N.; Smith, J. M., Diffusion in Catalyst Pellets. *Chem Eng Sci* **1962,** *17* (11), 825-834.

16. Bird, R. B.; Stewart, W. E.; Lightfoot, E. N., *Transport phenomena*. 2nd, Wiley international ed.; J. Wiley: New York, 2002; p xii, 895 p.

17. Nicholson, C.; Hrabetova, S., Brain Extracellular Space: The Final Frontier of Neuroscience. *Biophys J* **2017,** *113* (10), 2133-2142.

Chapter 2: A detailed model of electroenzymatic glutamate biosensors to aid in sensor optimization and in applications *in vivo*

Reproduced with permission from:

Clay, M.; Monbouquette, H. G., A Detailed Model of Electroenzymatic Glutamate Biosensors To Aid in Sensor Optimization and in Applications in Vivo. *ACS Chem Neurosci* **2018,** *9* (2), 241-251.

Abstract

Simulations conducted with a detailed model of glutamate biosensor performance describe observed sensor performance well, illustrate the limits of sensor performance, and suggest a path toward sensor optimization. Glutamate is the most important excitatory neurotransmitter in the brain, and electroenzymatic sensors have emerged as a useful tool for the monitoring of glutamate signaling *in vivo*. However, the utility of these sensors currently is limited by their sensitivity and response time. A mathematical model of a typical glutamate biosensor consisting of a Pt electrode coated with a permselective polymer film and a top layer of crosslinked glutamate oxidase has been constructed in terms of differential material balances on glutamate, H_2O_2 and O_2 in one spatial dimension. Simulations suggest that reducing thicknesses of the permselective polymer and enzyme layers can increase sensitivity ~6-fold and reduce response time ~7-fold, and thereby improve resolution of transient glutamate signals. At currently employed enzyme layer thicknesses, both intrinsic enzyme kinetics and enzyme deactivation likely are masked by mass transfer. However, O_2 dependence studies show essentially no reduction in signal at the lowest anticipated O_2 concentrations for expected glutamate concentrations in the brain, and that O_2 transport limitations *in vitro* are anticipated

only at glutamate concentrations in the mM range. Finally, the limitations of current biosensors in monitoring glutamate transients is simulated and used to illustrate the need for optimized biosensors to report glutamate signaling accurately on a subsecond timescale. This work demonstrates how a detailed model can be used to guide optimization of electroenzymatic sensors similar to that for glutamate and to ensure appropriate interpretation of data gathered using such biosensors.

2.1 Introduction

The rapid and selective sensing of neurotransmitters including dopamine,[1-3] acetylcholine,[4-7] and glutamate[8-12] with high spatial resolution has demonstrated usefulness for the study of neurological disorders as well as normal brain function in a variety of systems.[13] Electrochemical devices based on carbon fibers or on microelectrode arrays (MEAs) on silicon or ceramic microprobes have proven particularly well suited for selective neurotransmitter monitoring at subsecond resolution with less tissue damage than that associated with typical microdialysis probes, although not all analytes are amenable to facile electrochemical detection.[3, 13-17] Nevertheless, the sensing of multiple analytes on MEAs *in vivo* promises to be a powerful approach for study of the neurochemistry underlying normal and abnormal brain function and associated behaviors. Yet, the optimal construction and use of the various sensing sites of differing modality on these MEAs will require adequate mathematical simulations both to guide sensor optimization and to interpret properly the data gathered with such sensors.

Glutamate (Glut) sensors, for example, most commonly are electroenzymatic biosensors operated in constant potential amperometry mode. Typically, glutamate oxidase (GlutOx) serves as the molecular recognition element that catalyzes the oxidation of Glut to α-ketoglutarate in the presence of molecular oxygen to give ammonia and H_2O_2.

$$\text{L-glutamate} + H_2O + O_2 \rightarrow \alpha\text{-ketoglutarate} + NH_3 + H_2O_2$$

This selective recognition event is transduced, usually by electrooxidation of H_2O_2 at a platinum electrode held at a constant positive potential, to provide a measurable current signal that is correlated to Glut concentration. However, a variety of species exist in brain extracellular fluid (ECF) that may be oxidized directly at a platinum electrode at positive potential, therefore one or more permselective polymer films are deposited underneath or in conjunction with the immobilized GlutOx to prevent electrooxidizable species other than H_2O_2 from accessing the electrode surface.[10, 18-22] Such species, including ascorbic acid and dopamine, which typically are the most problematic for such Glut sensors, would otherwise cause a false current signal. A variety of polymeric materials have been used as permselective films including polypyrrole (PPY), polyethylenediamine (PPD), and Nafion.[10, 18] GlutOx has been immobilized in or on these various polymer films through methods entailing dip coating, manual spreading, or electrodeposition.[21, 23-25] Most commonly, GlutOx is immobilized on electrodes by spreading a mixture of enzyme and bovine serum albumin (BSA) on the electrode surface and crosslinking with glutaraldehyde.[23, 24] However, the many variations of methods used produces layers of different thicknesses and compositions that directly affect the sensitivity, response time, stability, and selectivity of the sensor.

Synaptic neurochemical signaling is thought to occur on the millisecond timescale, which is much faster than the reported response times of Glut sensors to date, yet more responsive sensors would be important to correlate neurochemical signaling with action potentials. In addition, the ideal Glut sensor would be able to resolve Glut signals at much less than 1 μM in order to address the controversy regarding Glut concentrations in the brain and to enable use of smaller sensing sites similar in area to those used for electrophysiological recordings. These important sensor attributes must be exhibited by an implantable device that can operate with high selectivity in the complex chemical and biological environment of the brain. There is a clear need for detailed simulations of transient conditions that can establish the theoretical

performance limits of an electroenzymatic Glut biosensor and that can facilitate its optimization.[26]

Many mathematical modeling studies of electroenzymatic biosensors based on numerical solutions of a modified diffusion equation have been published,[27-41] although frequently these solutions rely on simplified kinetics or a partial analytical solution,[33, 34, 37, 39] are limited to the steady state,[27, 30-34] and/or do not include the detail necessary (*e.g.*, an additional, enzyme-free permselective layer) to guide typical biosensor optimization.[27, 30-35, 38] Further, we are aware of no published, detailed modeling efforts of electroenzymatic Glut biosensors in particular. Glut sensors for neuroscience applications should be optimized for sensitivity, detection limit, selectivity, stability, and response time. Fortunately, modern, commercially available software has made the solution of the applicable partial differential equations more straightforward.

A new transient model of an electroenzymatic Glut biosensor operated in constant potential amperometry mode has been formulated and is described here. The model incorporates an oxygen-dependent rate model for GlutOx and explicit H_2O_2 electrooxidation kinetics,[42] as well as a description of internal and external mass transfer of Glut, oxygen and H_2O_2. In addition, the model describes the immobilized enzyme layer composition and thickness, and the effects of permselective films on Glut sensing performance. Detailed simulations using the model show the limits of sensor performance, the impact of controllable sensor design parameters on sensor attributes, and how the sensor response relates to actual external transients in Glut concentration. Finally, the mathematical model and accompanying assumptions show the contextual relevance of these results and can provide insight for similar electroenzymatic sensor devices.

2.2 Results and Discussion

2.2.1 Model Simulates the Sensitivity and Response Time of Existing Glutamate Biosensors

Numerical solutions of the linked sets of PDEs and boundary conditions that constitute the mathematical model (see below and Supporting Information for model details) provide the concentrations of Glut, O_2 and H_2O_2 at all points within the sensor surface coatings over chosen periods of time. This information can in turn be used to determine the response of the simulated sensor. To best represent recent Glut biosensor fabrication methods on arrayed microelectrodes,[3, 18, 25] initial simulations were conducted to describe the response of base-case sensors (with a 10-μm-thick permselective layer, a 20-μm-thick enzyme layer, and a GlutOx protein mass fraction, f_{glutox}, in the enzyme layer equal to 0.5) to a 0 to 10 μM step in sample Glut concentration at time zero. Such conditions are common for *in vitro* calibrations. Fig. 2.1 shows the temporal current response and the steady-state (SS) H_2O_2 concentration profile. The model predicts a corresponding sensitivity of 60.7 nA/μM/cm^2, consistent with experimental values of 51.3, 63.2, and 152.1 nA/μM/cm^2 for sensors made using a Nafion layer, and enzyme immobilization using BSA and glutaraldehyde.[24, 43, 44] The simulated response time, 0.73 s, also matches very closely with experimental response times (0.8 ± 0.2 s).[24] Here, response time was calculated as the time from the initial step-change in boundary concentration until the current reaches 90% of its steady-state (SS) value as is customary for these sensors used in neuroscience applications.

These initial results also provided some important observations regarding the sensor response time and the efficiency of H_2O_2 capture at the electrode surface. As shown in Fig. 2.1A, there is a time lag in current response from when Glut is introduced at t = 0 until current begins to increase due to the time required for initial Glut turnover and penetration of H_2O_2 to the electrode surface. This time lag contributes significantly to the overall response time, which demonstrates that response time cannot accurately be determined from the current rise time alone.

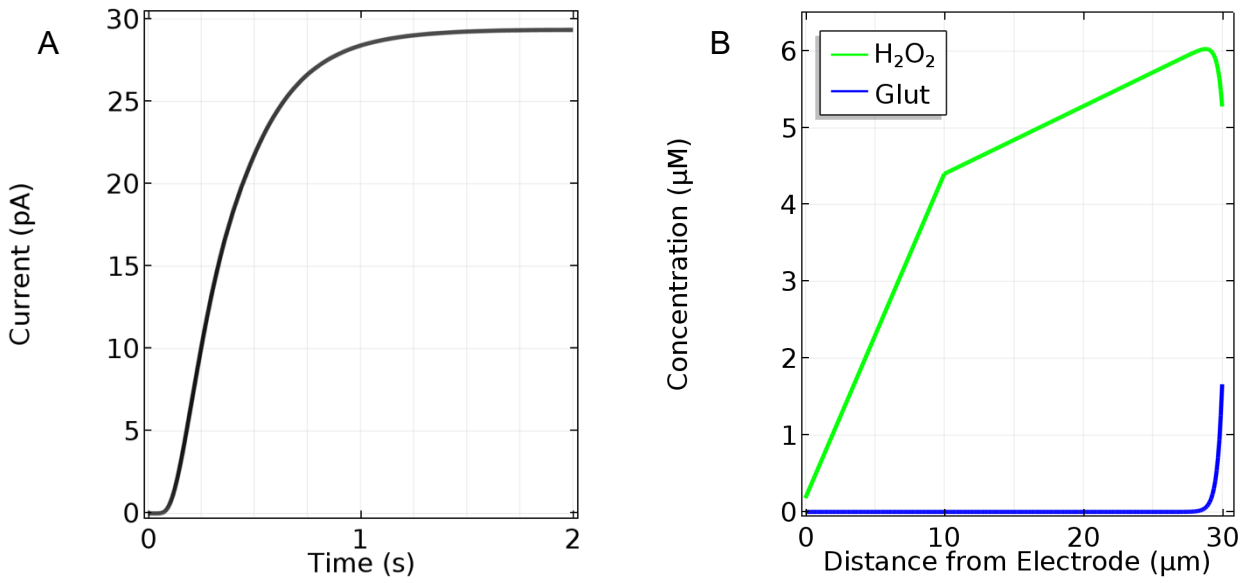

Figure 2.1. A. Temporal response of a base-case sensor (10 μm Nafion layer, 20 μm GlutOx layer) to a 10 μM step in bulk sample Glut concentration with sample O_2 concentration at 270 μM and B. the corresponding steady-state H_2O_2 concentration profile within the sensor layers. Note that the outer edge of the Nafion layer is at 10 μm and the outer edge of the sensor is at 30 μm.

In addition, the SS H_2O_2 concentration profile (Fig. 2.1B) shows that much of the H_2O_2 generated in the enzyme layer is lost back to the sample bulk solution. Calculations based on the flux toward the electrode surface compared to that toward the sample solution, indicate that only 3.6% of the H_2O_2 generated is electrooxidized at the electrode and contributes to the current signal. The concentration profile also shows that most H_2O_2 is produced within the first few microns into the enzyme layer. In agreement with this peak in the H_2O_2 profile near the sensor surface, the accompanying data for Glut shows that virtually all the analyte is consumed in the first few microns into the enzyme layer. These results strongly suggest that thinner enzyme layers could result in better performing sensors.

2.2.2 Thinner Permselective Films and Enzyme Layers Are Shown to Give Better Performing Sensors

Optimization of sensor fabrication generally entails incorporating enough enzyme and permselective resistance to ensure high sensitivity and selectivity without applying coatings so thick that they cause elevated mass transfer resistance and long response time. Efforts to balance these effects have resulted in numerous enzyme immobilization procedures and variations of permselective coatings,[45] but a theoretical treatment considering both permselective and enzyme layer characteristics can illustrate how a given sensor construct may be expected to perform relative to its theoretical limits. Fig. 2.2 shows that by reducing the Nafion and enzyme layer thicknesses, the sensitivity and response time theoretically can be improved an order of magnitude or more from the base case. However, the results also show that the enzyme layer thickness goes through an optimum for the various Nafion film thicknesses investigated. In general, sensitivity drops sharply for enzyme layer thicknesses less than a micron, which corresponds to ~45 enzyme monolayers. This result is consistent with published experimental results showing that enzyme immobilization through electropolymerization of ultra-thin layers produces sensors with lower sensitivity.[22, 46, 47] The decrease in sensitivity for thicker enzyme layers is consistent with the results shown in Fig 2.2 and is due to diffusional mass transfer limitations and the loss of the vast majority of H_2O_2 generated in the enzyme layer back to the sample solution.

Based on results displayed in Fig. 2.2 for an immobilized enzyme concentration corresponding to an f_{glutox} of 0.5, sensors with enzyme layer thicknesses less than ~5 μm show the greatest potential for improved sensitivity and response time. At ~5 μm and less, the sensitivity increases most sharply with reduced enzyme layer thickness, and the response times converge for Nafion layer thicknesses ranging from 0.1 to 5 μm. For what may be practical layer thicknesses of 1 and 3 μm (permselective layer and enzyme layer, respectively), the model predicts that sensitivity to Glut increases 6-fold over the base case and that the response time is

reduced to 33 ms. The highest sensitivity (780 nA/μM/cm^2) and fastest response time (10 ms) was observed for a sensor with a 0.1 μm thick layer of Nafion and a 0.5 μm thick layer of enzyme, although for layers this thin, assumptions concerning Nafion continuity (and ability to block interfering species such as ascorbate) and enzyme activity (see below) may need further consideration and experimental support. Based on a recent review article,[26] the best sensitivities achieved are in the vicinity of ~200 nA/μM/cm^2, which likely is due to a lack of experimental methods to generate very thin layers of active enzyme at high density on electrodes. The very fast theoretical response times for an optimized biosensor are consistent with characteristic times for enzyme-catalyzed reaction, based on k_{cat}, and for species mass transport, based on diffusivities and diffusion lengths; yet current experimental response times are in the ~1 s range, also due to overly thick enzyme and polymer layers. It is important to recognize here that these theoretical optima for sensitivity and response time are subject to the modeling assumptions described below and may not be experimentally attainable, however these simulation results do support the subjective conclusion that the performance of Glut biosensors can be improved significantly.

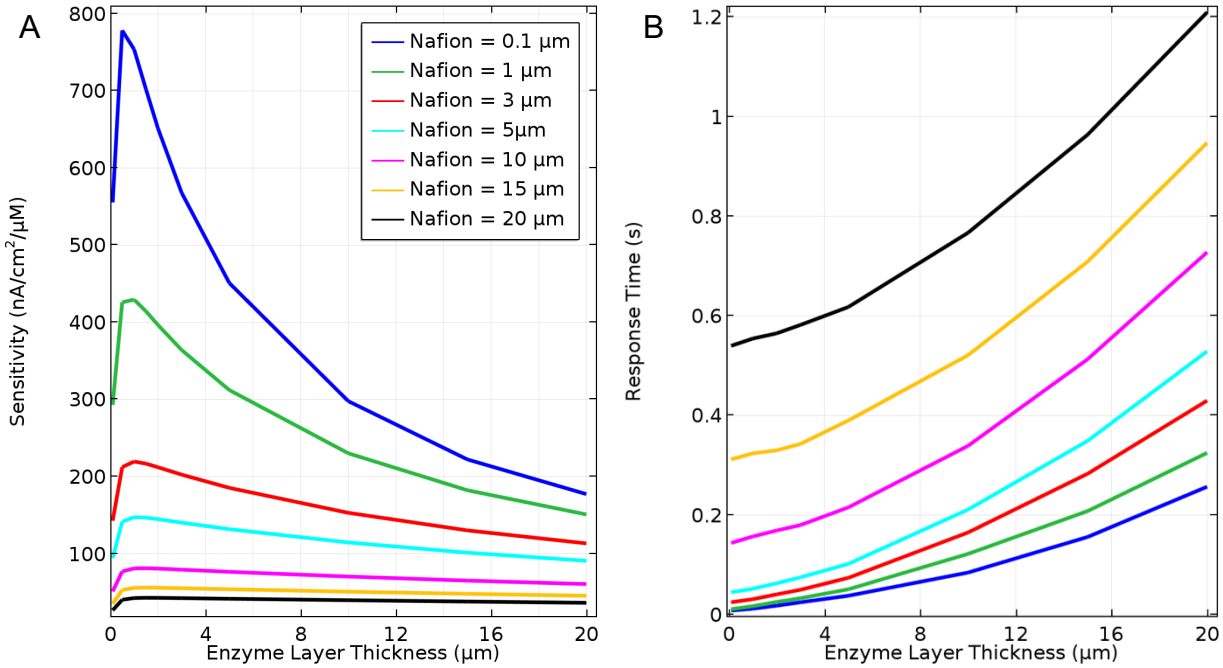

Figure 2.2. A. Sensor sensitivity based on steady-state response to a 10 µM Glut step change as a function of Nafion and enzyme layer thicknesses, and B. sensor response time (bottom) also as a function of layer thicknesses. In all cases, f_{glutox} = 0.5 and sample O_2 concentration equal to 270 µM.

2.2.3 Effect of Enzyme Loading and Activity

Improvements to electroenzymatic glutamate sensors also have been accomplished through fabrication procedures that have increased the amount of enzyme deposited on the sensor sites, and efforts to do this have been analyzed experimentally through studies that measure enzyme loading and functionality indirectly.[48] The modeling approach used here enables direct investigation of the effect of deposited enzyme concentration on sensor performance and thereby shows what can be expected when enzyme loading has been optimized experimentally.

For existing sensor designs, an easy design modification to investigate a change in enzyme loading without impacting catalytic layer thickness would be to mix a different proportion of GlutOx with BSA, thereby increasing or decreasing f_{glutox} and producing a different enzyme

concentration in the deposited layer. To test independently the effect of varied active enzyme concentration in the catalytic layer, f_{glutox} was varied from 0.01 to 0.9 for the base case sensor.

Interestingly, the current versus time plots in response to a 10 μM Glut step change show almost no difference over the broad range of f_{glutox} examined (Fig. 2.3A). The corresponding SS concentration profiles of Glut and H_2O_2 give insight into these results (Fig. 2.3B). As enzyme concentration decreases, more Glut diffuses farther into the enzyme layer before being oxidized to give H_2O_2, a phenomenon also observed in the simulation of similar glucose biosensors.[38] Even at low enzyme concentrations corresponding to f_{glutox} = 0.10, Glut is completely consumed within about 3 μm of the outer edge of the sensor, suggesting that the fraction of active enzyme has little to no effect for enzyme thicknesses much greater than a few microns. These results also suggest that the actual rate of GlutOx deactivation may be masked by mass transfer effects in sensors with thick enzyme layers,[49] since GlutOx deactivation essentially results in a decrease in f_{glutox} with time. If the lifetime of an implanted, electroenyzmatic Glut sensor is limited by GlutOx deactivation upon immobilization or by later exposure to H_2O_2, for example, these simulations also indicate that it may not be beneficial to construct sensors with the thinnest enzyme layers predicted to be optimal (Fig. 2.2).

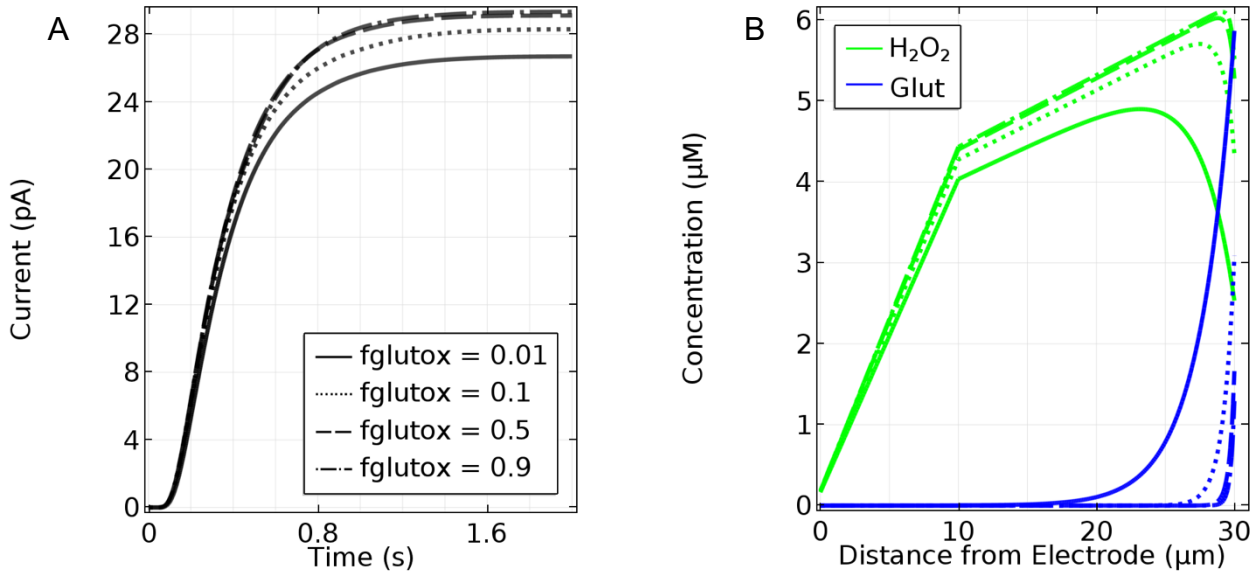

Figure 2.3. A. Current response to a 10-μM step change in Glut for sensors with 10-μm-thick Nafion and 20-μm-thick enzyme layers, where the f_{glutox} is varied from 0.01 to 0.9, and the sample O_2 concentration equals 270 μM. B. Corresponding plots of SS Glut and H_2O_2 concentration profiles in the Nafion and enzyme layers. Note that the outer edge of the Nafion layer is at 10 μm and the outer edge of the sensor is at 30 μm.

2.2.4 Mass Transfer Resistance and Oxygen Limitations Complicate Analysis of Immobilized Enzyme Kinetics

In the development of optimized electroenzymatic sensors, sensor performance is often tested over a range of substrate (*i.e.*, analyte) concentrations, and the measured signal commonly follows a trend resembling Michaelis-Menten kinetics (the apparent K_m represents the concentration of analyte that produces half of the maximum response, and the apparent k_{cat} is related to the maximum response). Thus, sensor performance is often evaluated using apparent sensor Michaelis-Menten parameters. Mass transfer resistance and oxygen limitations may explain in large part (enzyme crowding, crosslinking and deactivation may also contribute) the observed differences between sensor and intrinsic enzymatic values for K_m and k_{cat}, although the detailed physical basis for these differences have not been fully explored. Nevertheless, it might

be expected that the apparent kinetic parameters describing performance of an electroenzymatic sensor are shifted in a similar, straightforward manner away from the intrinsic, free solution values of the immobilized enzyme for all biosensors due to mass transfer effects and O_2 limitations, but the simulations of Glut biosensors shown below demonstrate that simple generalizations cannot be constructed. It is noteworthy here that the range of substrate concentrations that must be explored in order to estimate a sensor K_m typically extends up to an order of magnitude or more beyond that observed *in vivo*. Also, for these relatively high concentrations of Glut, levels of H_2O_2 near the electrode surface begin to affect the electrooxidation rate, further justifying the use of explicit electrooxidation kinetics in our model.

To investigate the apparent K_m of Glut biosensors and any complications due to mass transport resistance or O_2 limitations, the model was used to simulate the SS response to Glut ranging from 0.1 to 30 mM for biosensors with varied enzyme layer thicknesses. In order to highlight the effect of the enzyme coating, the permselective (Nafion) film was reduced to 10 nm in thickness so that its mass transfer resistance could be ignored.[34, 50] It may be expected that a sensor with a thinner enzyme deposit (and therefore reduced mass transfer resistance) would display apparent kinetics that more closely correspond to the intrinsic kinetics of GlutOx. However, Fig. 2.4 shows that even for enzyme layers 1 μm thick, the sensor K_m (0.6 mM) is considerably larger than that reported for the free enzyme in oxygen-saturated solution (0.173 mM), and even for layers 0.1 μm thick, the sensor K_m is 0.3 mM. It is important to note that these K_m values were generated under conditions affected by oxygen concentration (since the O_2 concentration at saturation is well below the intrinsic $K_{m,O2}$ and do not represent intrinsic enzyme kinetics, although mass transfer influence and oxygen limitation are more evident for the immobilized enzyme. An additional consequence of the oxygen transport limitations is a reduced apparent k_{cat}, which further complicates analysis of the immobilized enzyme kinetics underlying biosensor performance. Construction of biosensors with thinner immobilized enzyme layers might be expected to bring apparent k_{cat} values more in line with the free enzyme, but sensors with the

thinnest enzyme coatings display a further reduced apparent $k_{cat,}$ since a greater fraction of the produced H_2O_2 is swept into the bulk solution due to shorter diffusion distances to the sensor surface.

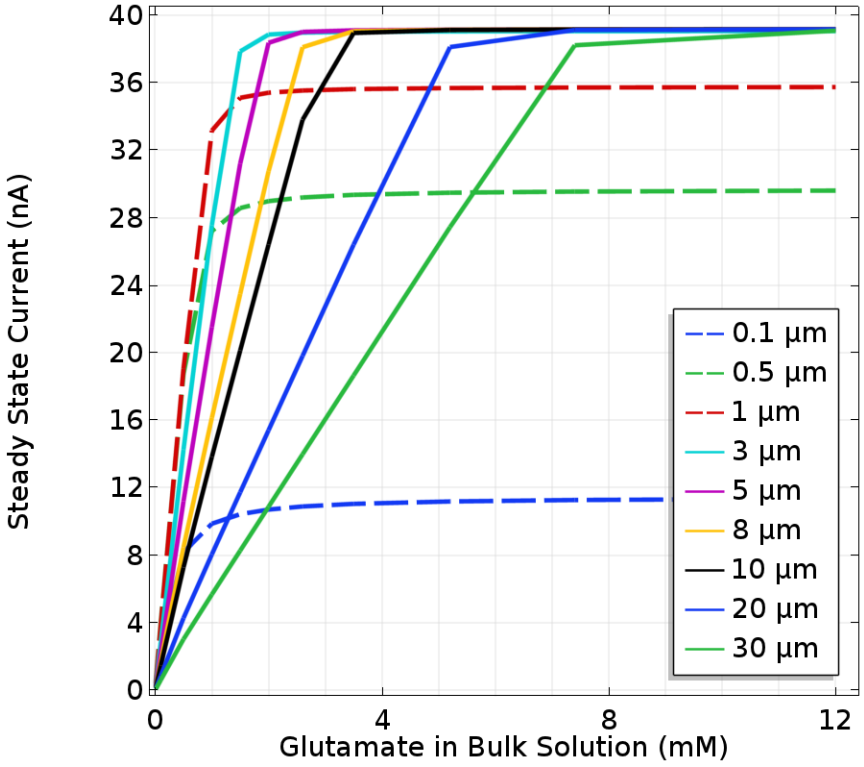

Figure 2.4. Modeled SS response of sensors with varied enzyme layer thicknesses and a permselective layer of negligible transport resistance. In all cases, f_{glutox} = 0.5 and the sample O_2 concentration equals 270 µM.

For thicker immobilized enzyme coatings, the sensor current response is linear to a higher Glut concentration until the maximum current at which O_2 becomes fully limiting (Fig. 2.4). The thickest layers, with a correspondingly greater mass transfer resistance, might be expected to have a lower maximum current response. However, since oxygen is produced at the electrode surface when H_2O_2 is electrooxidized, Glut that has diffused deep into the enzyme layer can be turned over to produce H_2O_2 much closer to the electrode surface. This mitigates the increased mass transfer resistance present in thicker deposits, and causes sensors to operate in a

fundamentally different manner at high Glut concentrations. This is best understood by examining first the concentration profiles of O_2, H_2O_2, and Glut in the thickest enzyme layers (> ~3 μm) at saturating Glut concentration (Fig. 2.5). Under these circumstances, it is evident that O_2 does not penetrate from the bulk to the electrode surface and is essentially depleted to near zero in a broad zone in the center of the layer where the GlutOx-catalyzed reaction rate must be near zero as well. When the bulk Glut concentration is sufficiently high that the concentration at the inner edge of the enzyme coating is much greater than $K_{m,glut}$, the enzyme kinetics are independent of Glut concentration, and H_2O_2 and O_2 are cycled in a zone close to the electrode. This condition corresponds to the maximum current observed for sensors with thick enzyme layers and is identical for all these sensors, since the enzyme kinetics driving the sensor response are independent of Glut concentration. However, as the enzyme deposit is made thinner (but still greater than ~3 μm), the Glut transport resistance is reduced and higher currents at lower Glut concentrations are observed, which corresponds to lower sensor K_m values. For enzyme layers somewhat less than 3 μm in thickness (Fig. 2.5), increased H_2O_2 loss to the bulk with progressively reduced thicknesses limits both the maximum concentration of H_2O_2 attained in the enzyme layer and the maximum current, despite the fact that greater O_2 penetration is achieved such that Glut turnover occurs throughout the enzyme layer. Yet importantly, Glut transport resistance also is reduced, and optimal performance in terms of current signal at physiological Glut concentrations is observed (as described earlier). Based on this analysis, it should be clear that inferences about the state of the enzyme upon immobilization cannot be made straightforwardly based on sensor K_m and maximum current measurements alone, rather the influence of O_2 limitations and other mass transfer effects must be considered carefully as well.

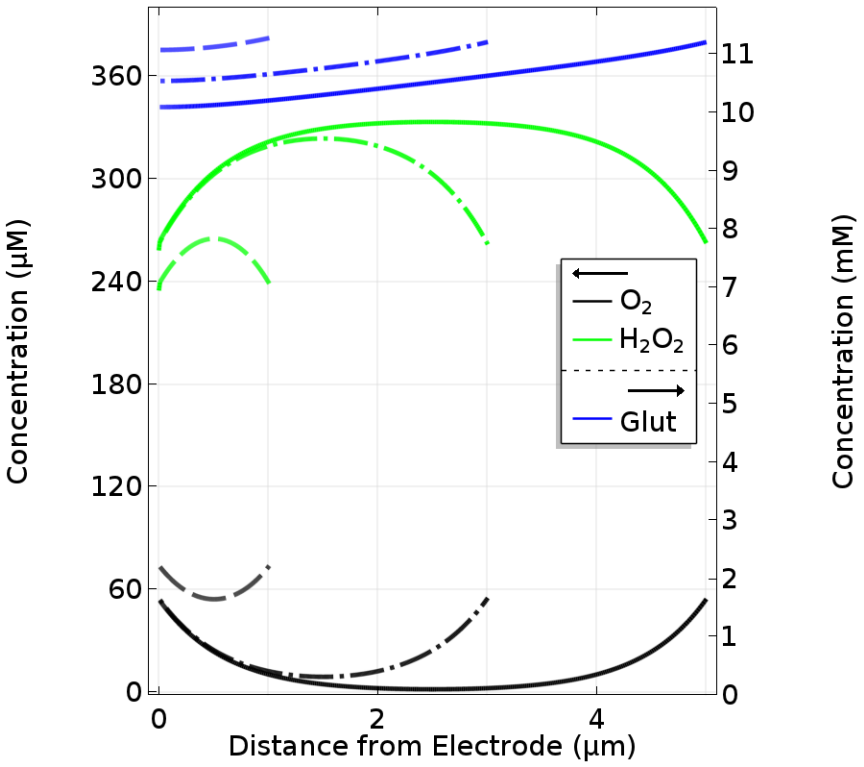

Figure 2.5. Concentration profiles of O_2, H_2O_2, and Glut for sensors with 1, 3, or 5 μm thick enzyme coating after reaching a steady state with saturating Glut (12 mM). In all cases, f_{glutox} = 0.5 and the sample O_2 concentration equals 270 μM.

2.2.5 Oxygen is Not Expected to Limit Glutamate Sensing in the Brain Under Normal Conditions

In brain extracellular fluid (ECF), Glut concentrations are expected to be ≤10 μM under normal circumstances where significant trauma has not occurred.[51] Sensor response to this range of Glut concentrations *in vitro* should not be influenced by O_2 concentrations, since the saturating concentration of O_2 in water from air at 25° C is ~270 μM. However, O_2 concentrations in ECF can be far lower, commonly 5-50 μM.[52] To investigate whether O_2 limitations would be a problem at the lower expected O_2 concentrations *in vivo*, simulations were generated using base-case thickness parameters (10 μm Nafion and 20 μm enzyme layers) and otherwise identical boundary conditions as those used for Fig. 2.4. The results presented in Fig. 2.6 show that

sensors respond linearly, as expected, until O_2 is depleted within the enzyme layer, at which point a sensor cannot discern differences in Glut concentration and the response flattens. At the lowest O_2 concentration examined (5 μM), the sensors could discern differences in Glut concentration up to 15 μM, and for O_2 at 25 μM, they could differentiate between Glut concentrations well beyond expected ECF levels (Fig. 2.6). Improved sensors with thinner Nafion and enzyme layers behave similarly at the low O_2 concentrations expected in the brain. Thus, these Glut biosensors are expected to be useful at relatively low O_2 concentrations *in vivo*.

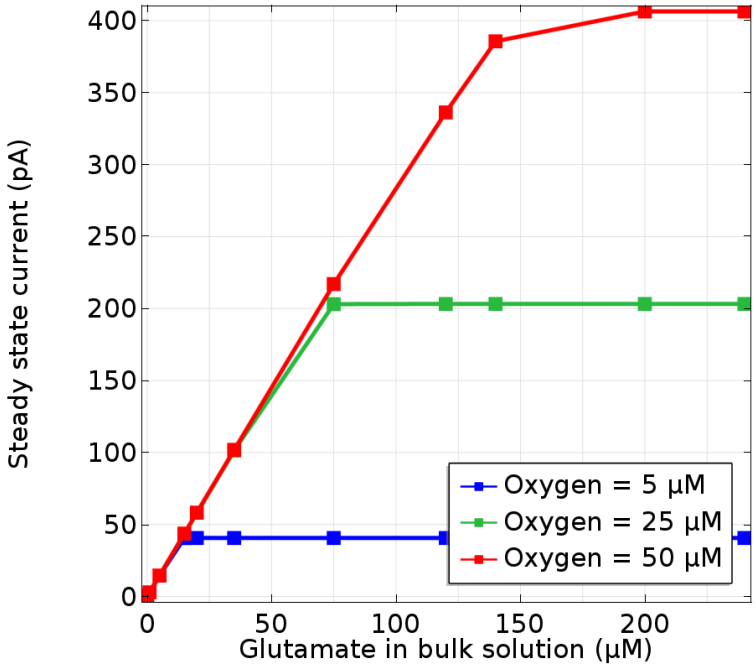

Figure 2.6. Steady-state response of a base-case sensor to increasing Glut concentrations over the range of O_2 concentrations typical in brain ECF.

2.2.6 Mass Transfer Limitations Cause Distortion of Sensor Output Relative to Pulsed Glutamate Signal Input

One of the advantages of constant-potential amperometric methods as opposed to other methods of detection, including fast cyclic voltammetry, is its potential for near continuous

sampling and very rapid response times as illustrated above.[53] However, the simulations above focused on sensor response to an instantaneous step change in Glut concentration, whereas for studies *in vivo*, the Glut signals commonly would take the form of signal pulses. A key issue, therefore, is the relationship between sensor output and the transient signal input. A further step, which is beyond the scope of this work, would additionally consider how release from synapses and diffusion through brain tissue results in a transient concentration at the surface of the sensor. As an illustrative preliminary investigation into the ability of the electroenzymatic Glut biosensor to track concentration transients in the brain, simulations were run to approximate the case where Glut release takes place right at the surface of a sensor (*i.e.*, the outer edge of the enzyme layer). The results illustrate the ability of a sensor to describe a Glut signal input, and likely represent the best possible signal resolving ability to be expected for these sensors *in vivo*.

In this modeling study, the Glut concentration at the surface of the sensor was changed from zero to a maximum in a Gaussian-shaped pulse with respect to time, $C_{glut}(t) = C_{max} \mathrm{e}^{-\left(t-t_p\right)^2 / 2\sigma^2}$, where C_{max} is the maximum bulk sample concentration (taken as 10 μM), t_p is the center of the pulse (0.5 s), and σ is its standard deviation. The value of 4σ represents the approximate time that Glut is potentially measurable. The simulated distortion in the base-case sensor signal relative to the imposed concentration pulse at the sensor surface is shown in Fig. 2.7 for pulses of σ = 0.25 s and σ = 0.05 s with the pulsed Glut concentration normalized relative to its maximum and the sensor current signal normalized relative to its previously modeled, SS response to the maximum Glut concentration of the pulse, C_{max}. As expected, the peak sensor response is time shifted relative to that for the input Glut transient, which is representative of the sensor response time. The simulated sensor output also is broadened and skewed relative to the symmetric input peak, and the maximum current observed is well short of that expected for 10 μM Glut, based on the SS response. Thus, the base case sensor might not prove reliable for estimation of peak Glut concentrations *in vivo* based on SS calibration data *in vitro*. Also, the less steep and asymmetric

output signal obtained relative to the input can make the use of such sensor data for determination of Glut release and uptake kinetics problematic. Similar issues have been described in a frequency response analysis of glucose biosensors.[38]

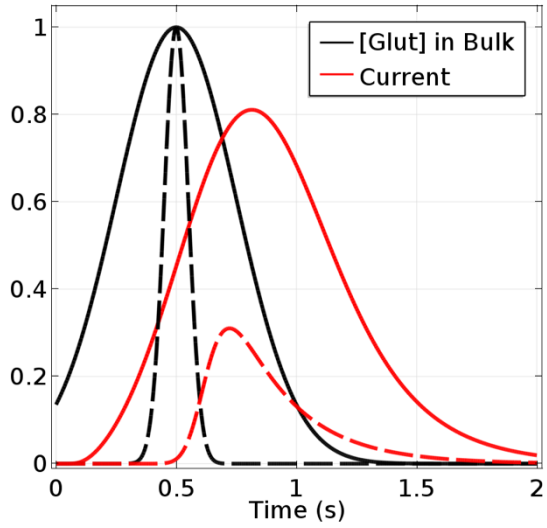

Figure 2.7. Glut concentration at sensor edge (relative to its maximum concentration) and observed current signal (relative to the SS current for the maximum Glut concentration). The solid curves correspond to an input pulse and output signal for a Gaussian input with σ = 0.25 s and C_{max} = 10 μM, and the dashed curves correspond to an input with σ = 0.05 s and C_{max} = 10 μM.

Fig. 2.8A shows the predicted response of the base-case Glut sensor to Glut concentration pulses (10 μM peak concentration) of varied σ centered at 0.5 s, as well as the response to a step change in Glut to 10 μM. The simulations show that if pulsed Glut is present in solution for less than 1 s (σ < 0.25 s), the sensor will show less than 75% of the maximum concentration reached. If the goal is to observe multiple Glut signals, maintaining full resolution of transients present for less than a second is ideal. Fortunately, simulations suggest that a sensor with thinner coatings (1 μm Nafion and 3 μm enzyme) and a response time of 0.03 s, would show little delay, distortion, or reduction of response relative to the input signal, and would be able to distinguish between instantaneous step changes in concentration as well as concentration pulses (Fig. 2.8B). These

results indicate that sensors with thinner layers can not only have greatly increased sensitivities but also could be well suited to measure rapid Glut transients.

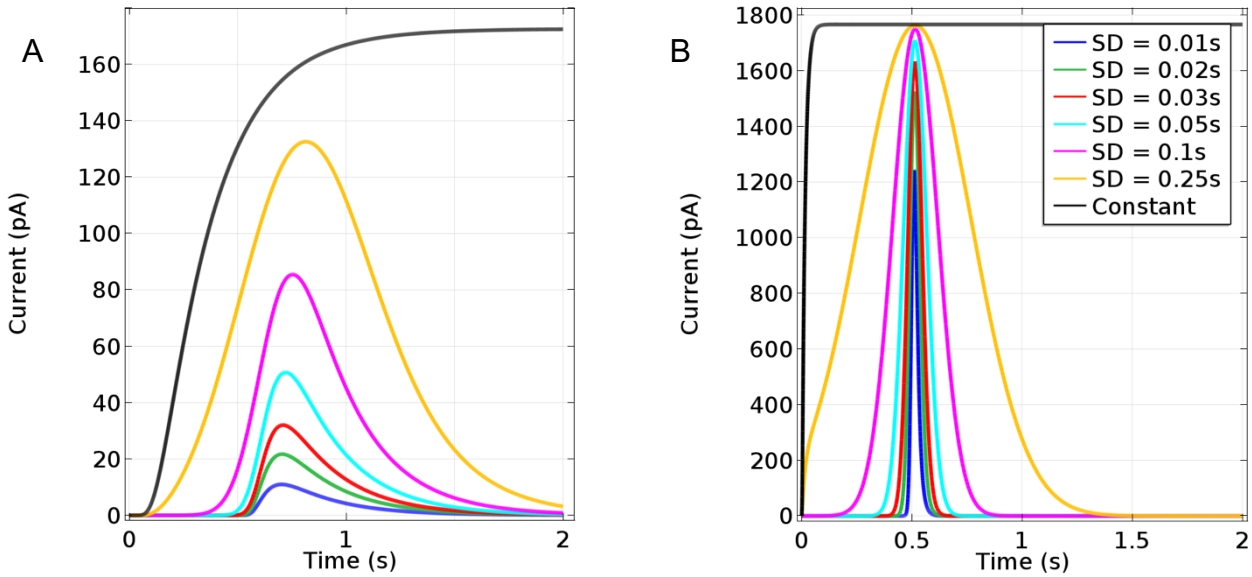

Figure 2.8. A. Modeled base-case sensor response to a single pulsed Glut concentration reaching maximum glutamate concentration (C_{max} = 10 μM) at 0.5 s and with standard deviations ranging from 0.01-0.25 s and to a step change in bulk sample Glut concentration to 10 μM for reference. B. Responses of a sensor with 1 μm Nafion and 3 μm enzyme layers to the same inputs.

2.2.7 Mass Transfer Resistances Limit Resolution of Sequential Glutamate Signals

Based on the simulations above, the increased breadth of the base-case sensor output relative to the actual Glut pulse width is expected to be problematic for resolution of a rapid train of Glut signals *in vivo*. When considering this, it also is important to account for noise that can obscure currents within 1 pA[16, 24] of each other. Fig. 2.9 shows how multiple pulses of σ = 0.1 s separated by 0.3, 0.35, 0.4, and 0.5 s (Fig. 2.9) would be reported by the base-case sensor (Fig. 2.9A). Based on these simulations, such concentration peaks in solution must be separated by at least 0.35 s seconds to be resolved clearly. In contrast, sensors with thinner coatings (1 μm

Nafion and 3 μm enzyme), and thus faster response times, maintain clear resolution of the same pulses (Fig. 2.9B).

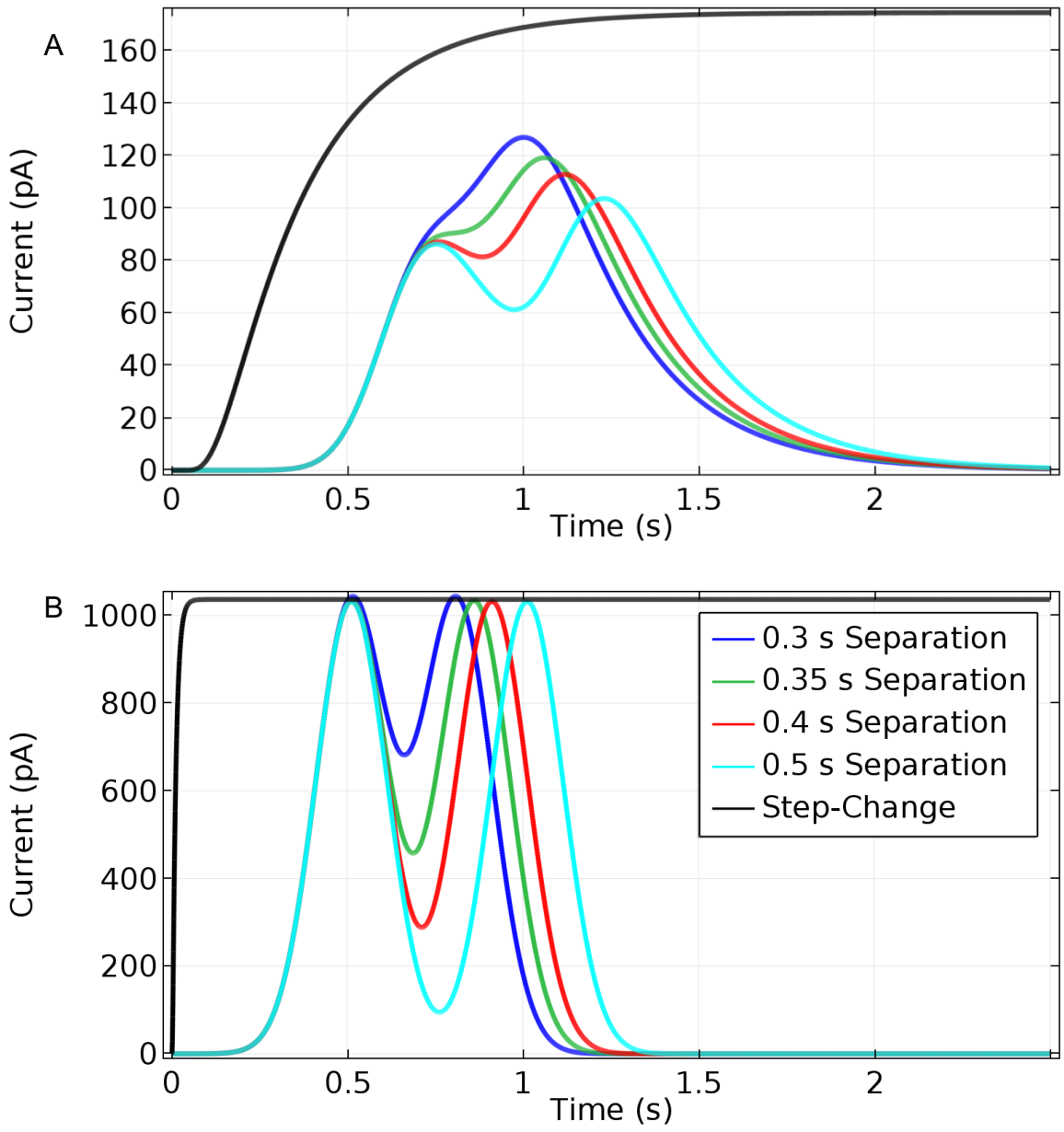

Figure 2.9. Sensor response to a Glut concentration step change to 10 μM and to two Glut pulses of σ = 0.1 s and C_{max} = 10 μM, separated by 0.3, 0.35, 0.4, and 0.5 s. A. Base-case sensor response. B. Response of a sensor with 1 μm Nafion and 3 μm enzyme layers.

2.3 Mathematical Model

2.3.1 Differential Mass Balances and Boundary Conditions

The model was developed to represent existing electroenzymatic Glut sensors based on an immobilized GlutOx layer deposited on a permselective polymer film atop a Pt electrode held at constant potential (Fig. 2.10).[24] Three chemical species are of particular interest in modeling these Glut biosensors, Glut, H_2O_2, and O_2; and the rates at which they are transported and participate in reactions determine the limits of how well a sensor can function. Transport of and reactions involving each of these three species were modeled with time-dependent mass balance equations of the general form below,

$$\varepsilon \frac{\partial C_i}{\partial t} = -D_{eff} \frac{\partial^2 C_i}{\partial x^2} + r_i$$

where ε is the porosity of the enzyme or permselective layer; C_i is the pore concentration of each species (i), *e.g.*, Glut, O_2 or H_2O_2; t is time; D_{eff} is the effective diffusivity; x is the distance from the Pt electrode surface; and r_i is the volumetric reaction rate, which is zero for all species in the permselective layer (see Supporting Information for a complete listing of mass balance equations, boundary conditions, parameters and parameter values). The enzyme and permselective polymer layers were modeled as separate mathematical domains where equality of fluxes as well as solute partitioning were described in appropriate boundary conditions at the interface between the layers. As described above, the enzyme layer typically consists of co-deposited GlutOx and BSA, which are crosslinked with glutaraldehyde. Although the permselective layer commonly consists of an electrodeposited film of polypyrrole (PPY) or of polyphenylenediamine (PPD) and a dip-coated layer of Nafion,[24] this model treated these coatings as one layer of Nafion, since the Nafion layer is generally much thicker and poses the dominant mass transfer resistance. At the Pt electrode surface, H_2O_2 electrooxidation kinetics were modeled explicitly in boundary

conditions, equating species transport to the consumption and generation of H_2O_2 and O_2, respectively, since H_2O_2 electrooxidation results in the generation of O_2 as well as protons. In contrast, the Glut flux at this solid boundary was set equal to zero. At the outer edge of the enzyme layer, which is in contact with the sample environment, transport of the species was modeled using appropriate mass transfer coefficients (see below) or the concentration was described by a time-dependent function. Depending on the values of the mass transfer coefficients used or the imposition of a time-dependent expression for the concentration of species at the enzyme layer/sample interface, the model may be representative of a probe in a flow cell used to measure sensor response characteristics or of a probe implanted in brain tissue where transients in Glut concentration at the sensor surface might be expected. Finally, the current produced by the sensor was modeled based on the expression for H_2O_2 electrooxidation, which includes a parameter that accounts for reduced Pt surface area due to electrodeposited polymer and the influence of local O_2 concentration on the electrooxidation rate.[42]

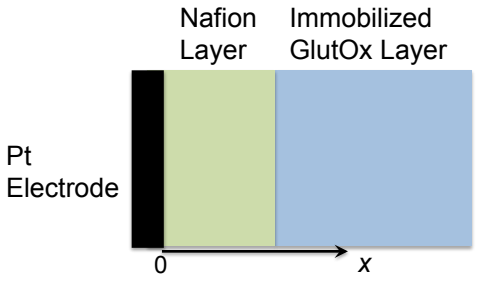

Figure 2.10. Schematic of the base-case Glut biosensor used in the model with a 10-μm-thick permselective Nafion layer and a 20-μm-thick immobilized GlutOx layer.

2.3.2 Modeling Assumptions and Parameter Values

The formulation of the model equations and the choices of parameter values rely on a number of assumptions and approximations. The following key assumptions were made in formulating the differential material balances for species in the enzyme and permselective layers:

1. One-dimensional mass transport
2. Solutions are dilute and layers are homogeneous such that Fick's Law applies
3. The enzyme layer void space can be represented by a network of random pores such that the model for effective diffusivity of Wakao and Smith[54] applies
4. Enzyme kinetics are not changed by immobilization and can be described by a ping-pong, dual-substrate mechanism similar to that for other oxidases including glucose oxidase[55]
5. No enzyme is deactivated during immobilization and enzyme deactivation is not important over the time course of the simulations
6. H_2O_2 electrooxidation kinetics[56] are not affected by species other than H_2O_2 and O_2
7. Ammonia production does not affect kinetics and its potential electrooxidation does not contribute significantly to the current signal

One-dimensional transport is a reasonable approximation for microelectrodes with characteristic dimension exceeding 25 μm,[57] which applies well to the ~40 μm × ~100 μm microelectrodes produced by us.[24] The second assumption regarding the applicability of Fick's law is commonly applied in models of this type where concentrations are indeed relatively dilute. However, the enzyme and permselective polymer layers may not be homogeneous in reality, which necessitates the use of effective diffusion coefficients and average reaction rates.

The effective diffusivities of each species were based on their diffusion coefficients in water, D_i.[58] For the enzyme layer, the water diffusivity was multiplied by the square of the medium porosity to give the effective diffusivity in accordance with the random pore model,[54] while for the permselective layer a simple multiplier, α, was used to match published effective diffusivities in Nafion. Since a large range of diffusivities in Nafion have been reported,[59] the values used here for α were based on reported measurements of O_2 effective diffusivity at a temperature, pressure, and water content that resembles biosensor conditions.[59, 60]

Conditions in the enzyme layer of the biosensor may alter enzyme kinetics significantly as a consequence of covalent crosslinking and the high protein concentration. Recent work on enzymes in intracellular environments, for example, has shown that enzymatic rates under such crowded conditions may be increased or decreased depending on the enzyme, the reactions catalyzed, and the nature of the enzyme microenvironment.[61, 62] Many of these changes can be explained by considering the effects of reduced void space on mass transport,[63-65] which is accounted for through the effective diffusivities described above. However, for lack of applicable data, other influences on observed GlutOx kinetics were not included in the model. Also, it is known that glutaraldehyde can cause enzyme deactivation during immobilization, yet as discussed below, this may not be a significant concern for thicker enzyme deposits.

The rate equation for H_2O_2 electrooxidation was taken from a study conducted under conditions resembling the physiological, where the reaction has been shown to be phosphate-mediated.[66] More complex rate forms and slightly different rate constants than those used here have been generated to account for nonlinearities in the reaction rate due to influences of pH, chloride ion, temperature, electrode potential, and deficiencies in phosphate.[67] However, these alternative rate forms apply to conditions that generally are not expected in the brain.

The last assumption listed above may constitute a significant approximation, especially if the ammonia concentration reaches a level sufficient to overcome any buffering capacity in the enzyme layer and causes pH to rise significantly into the alkaline range. In this situation, enzyme activity may be affected and ammonia electrooxidation may occur; however this effect may be moderated by the production of protons at the electrode surface as H_2O_2 is electrooxidized. It is well known that ammonia, and to a lesser extent ammonium,[68] is electrooxidized on Pt under alkaline conditions; yet, we have not observed ammonia or ammonium ion electrooxidation currents above noise on bare Pt or on PPD/Nafion-coated Pt at the operating potential for Glut biosensors (0.7 V vs. Ag/AgCl) and at pH 7-11 (data not shown). Clearly, this model does not include a description of all phenomena of potential importance and does entail some important

assumptions and approximations; regardless, it can serve as a useful tool to study the interplay of kinetics and mass transfer on biosensor performance and as a guide for device optimization as described below.

A full list of parameters, definitions and values is given in the Supporting Information. Parameter values were obtained directly from the literature, measured experimentally, or calculated from published experimental data. The thickness of a dip-coated Nafion layer on a microelectrode array site[3] has been observed by us using scanning electron microscopy to range from 5 to 20 μm, thus the thickness of the permselective Nafion layer was modeled in the base case as 10 μm, but was also varied over the range of 0.1 to 20 μm when investigating the effects of Nafion layer thickness. The void fraction (*i.e.*, porosity) of the enzyme layer was set at 0.5, whereas that for the permselective layer was chosen based on measured Nafion film void fractions.[69]

Parameters related to the GlutOx concentration in the enzyme layer and GlutOx kinetics are discussed in detail in the Supporting Information. Although the reaction mechanism for GlutOx has not been established, the enzyme kinetics were modeled according to the common ping-pong reaction mechanism of oxidase enzymes.[55] Also, Glut concentrations in the brain before and after trauma have been measured to range from 1-50 μM,[51] in accordance with our experimental sensor measurements,[24] which guided the range of Glut concentrations investigated.

Species transport from the sample space to the outer edge of the sensor enzyme layer was described in terms of mass transfer coefficients. Such a mass transfer coefficient has been measured for O_2 at a microelectrode surface in a flow field,[70] and experiments testing sensor response time have used flow cells with similar flow rates (~1 cm/s) and dimensions.[24] The mass transfer coefficients for Glut and H_2O_2 were estimated based on their molecular diffusivities relative to that for O_2 and the theoretical relationship between a species diffusivity and its mass transfer coefficient.[71] The partition coefficient between the electronegative permselective film

(Nafion) and the enzyme layer was assumed to be 1 for the charge neutral O_2 and H_2O_2 species and 10^{-3} for negatively charged Glut, thereby essentially excluding Glut from the permselective layer. The equation for the current generated at the electrode surface accounts for two electrons liberated with each oxidized H_2O_2 molecule, platinum electrooxidation kinetics based on the concentration of H_2O_2 and O_2 at the electrode surface (see Supporting Information),[42] and an electrode surface area of 4800 μm^2 that is half covered with a polypyrrole permselective film as follows from its porosity, which was taken as 0.5.[72]

2.3.3 Numerical Solution

The model was solved using COMSOL (v. 5.2a) using 1D coefficient form PDE physics and the standard finite element solver, with time steps as small as 0.1 ms in cases where the simulations reached a steady state very rapidly or as boundary conditions required. Each domain was given a coefficient form PDE with local variables and a global variable version to implement the partition coefficient. Advanced physics settings were required to specify the partitioned concentrations between layers without disrupting flux continuity. Error tolerances for all variables were set to 10^{-9}. Solutions were verified to be mesh independent at the settings used, by first splitting the combined domains into 100 domain elements (between 6 nm and 0.3 μm in size, depending on overall sensor thickness) and then refining to 200 or 300 elements as needed. To smooth the solutions over the first few time steps, the bulk sample Glut concentration was stepped from 0 to the specified value over the first 0.01 s, or with further mesh refinement at domain boundaries. Use of the COMSOL software package enabled straightforward exploration of parameters representing experimentally controllable characteristics, including enzyme and permselective layer thicknesses, and enzyme loading, which might be optimized for improved sensor performance.

2.4 Conclusion

A detailed mathematical model of an electroenzymatic glutamate sensor that accounts for diffusion and reaction in an immobilized enzyme layer and diffusion across a permselective polymer layer to an underlying Pt electrode was constructed without any adjustable parameters. The model simulates well the performance of existing glutamate biosensors consisting of permselective polymer and enzyme layers of ~10 and ~20 microns in thickness, and illustrates a lag in biosensor current response that makes estimation of response time from current rise time problematic. These simulations also show that >95% of H_2O_2 generated in the thick enzyme layers characteristic of current biosensors is lost back to the sample environment, which suggests that biosensors constructed with much thinner polymer and enzyme layers would be optimal. A theoretically near-optimal biosensor with polymer and enzyme layers of 1 μm and 3 μm in thickness would result in several-fold improvement in response time and sensitivity to ~30 ms and ~365 nA/μM/cm^2; yet these predictions might best be interpreted as qualitative, as they are subject to the modeling assumptions described. Interestingly, for enzyme layers greater than a few microns in thickness, the simulations also show that enzyme loading over the practical range has very little impact on sensor performance due to mass transfer effects unless much less than 1% of the enzyme is functional. This result suggests that enzyme deactivation, which was not included in the model, may also be masked by mass transfer effects. Mass transfer effects, including related O_2 limitations, also mask intrinsic enzyme kinetics such that the apparent sensor Glut K_m for GlutOx, even for a very thin 1 μm thick layer, is much higher than what is observed for the enzyme in free solution. Thus, care must be taken in inferring conclusions about the state of the immobilized enzyme from these sensor kinetic constants without support from simulations. Model simulations also showed that O_2 transport limitations are not expected to limit sensor performance in discerning glutamate concentrations up to 15 μM for sample O_2 concentrations as low as 5 μM. Finally, an analysis of biosensor response to subsecond glutamate pulses of the sort that may be representative of glutamate signals in the brain shows the limitations of existing

glutamate biosensors and the promise of theoretically optimized biosensors in monitoring such signals.

The results presented here are specific to electroenzymatic Glut biosensors of the construction described, although they can be extended to other electroenzymatic sensors by adjusting enzyme layer parameters and those of permselective polymer film(s) as necessary. However, the limitations of the model to one spatial dimension makes it difficult to investigate the effects of electrode surface roughness, which has been shown to increase sensitivity by more than an increase in surface area alone would predict,[73] and makes it impossible to optimize electrode size or placement on microelectrode array probes. Extension of the model to three spatial dimensions is planned to address these issues and to enable incorporation of probe placement into a simulated brain region, where synaptic release and subsequent diffusion and uptake could also be modeled, so as to provide insights into operation *in vivo* of existing and theoretically optimized sensors.

2.5 References

1. Clark, J. J., Sandberg, S. G., Wanat, M. J., Gan, J. O., Horne, E. A., Hart, A. S., Akers, C. A., Parker, J. G., Willuhn, I., Martinez, V., Evans, S. B., Stella, N., and Phillips, P. E. M. (2010) Chronic microsensors for longitudinal, subsecond dopamine detection in behaving animals, *Nature Methods 7*, 126-U158.
2. Robinson, D. L., Venton, B. J., Heien, M. L. A. V., and Wightman, R. M. (2003) Detecting subsecond dopamine release with fast-scan cyclic voltammetry in vivo, *Clin Chem 49*, 1763-1773.
3. Tseng, T. T., and Monbouquette, H. G. (2012) Implantable Microprobe with Arrayed Microsensors for Combined Amperometric Monitoring of the Neurotransmitters, Glutamate and Dopamine, *J Electroanal Chem (Lausanne) 682*, 141-146.

4. Parikh, V., Pomerleau, F., Huettl, P., Gerhardt, G. A., Sarter, M., and Bruno, J. P. (2004) Rapid assessment of in vivo cholinergic transmission by amperometric detection of changes in extracellular choline levels, *Eur J Neurosci 20*, 1545-1554.

5. Garguilo, M. G., and Michael, A. C. (1996) Amperometric microsensors for monitoring choline in the extracellular fluid of brain, *J Neurosci Meth 70*, 73-82.

6. Huang, Z. X., Villartasnow, R., Lubrano, G. J., and Guilbault, G. G. (1993) Development of Choline and Acetylcholine Pt Microelectrodes, *Anal Biochem 215*, 31-37.

7. Mitchell, K. M. (2004) Acetylcholine and choline amperometric enzyme sensors characterized in vitro and in vivo, *Analytical Chemistry 76*, 1098-1106.

8. Kulagina, N. V., Shankar, L., and Michael, A. C. (1999) Monitoring glutamate and ascorbate in the extracellular space of grain tissue with electrochemical microsensors, *Analytical Chemistry 71*, 5093-5100.

9. Burmeister, J. J., Pomerleau, F., Palmer, M., Day, B. K., Huettl, P., and Gerhardt, G. A. (2002) Improved ceramic-based multisite microelectrode for rapid measurements of L-glutamate in the CNS, *J Neurosci Meth 119*, 163-171.

10. Hamdi, N., Wang, J., and Monbouquette, H. G. (2005) Polymer films as permselective coatings for H2O2-sensing electrodes, *Journal of Electroanalytical Chemistry 581*, 258-264.

11. Hamdi, N., Wang, J., Walker, E., Maidment, N. T., and Monbouquette, H. G. (2006) An electroenzymatic l-glutamate microbiosensor selective against dopamine, *Journal of Electroanalytical Chemistry 591*, 33-40.

12. Walker, E., Wang, J., Hamdi, N., Monbouquette, H. G., and Maidment, N. T. (2007) Selective detection of extracellular glutamate in brain tissue using microelectrode arrays coated with over-oxidized polypyrrole, *Analyst 132*, 1107-1111.

13. Bucher, E. S., and Wightman, R. M. (2015) Electrochemical Analysis of Neurotransmitters, *Annu Rev Anal Chem (Palo Alto Calif) 8*, 239-261.

14. Burmeister, J. J., Moxon, K., and Gerhardt, G. A. (2000) Ceramic-based multisite microelectrodes for electrochemical recordings, *Analytical Chemistry 72*, 187-192.

15. Burmeister, J. J., Pomerleau, F., Huettl, P., Gash, C. R., Wemer, C. E., Bruno, J. P., and Gerhardt, G. A. (2008) Ceramic-based multisite microelectrode arrays for simultaneous measures of choline and acetylcholine in CNS, *Biosensors & Bioelectronics 23*, 1382-1389.

16. Wassum, K. M., Tolosa, V. M., Tseng, T. C., Balleine, B. W., Monbouquette, H. G., and Maidment, N. T. (2012) Transient extracellular glutamate events in the basolateral amygdala track reward-seeking actions, *J Neurosci 32*, 2734-2746.

17. Malvaez, M., Greenfield, V. Y., Wang, A. S., Yorita, A. M., Feng, L. L., Linker, K. E., Monbouquette, H. G., and Wassum, K. M. (2015) Basolateral amygdala rapid glutamate release encodes an outcome-specific representation vital for reward-predictive cues to selectively invigorate reward-seeking actions, *Sci Rep-Uk 5*.

18. Hascup, K. N., Hascup, E. R., Littrell, O. M., Hinzman, J. M., Werner, C. E., Davis, V. A., Burmeister, J. J., Pomerleau, F., Quintero, J. E., Huettl, P., and Gerhardt, G. A. (2013) Microelectrode Array Fabrication and Optimization for Selective Neurochemical Detection, pp 27-54.

19. Ammam, M., and Fransaer, J. (2010) Highly sensitive and selective glutamate microbiosensor based on cast polyurethane/AC-electrophoresis deposited multiwalled carbon nanotubes and then glutamate oxidase/electrosynthesized polypyrrole/Pt electrode, *Biosens Bioelectron 25*, 1597-1602.

20. Batra, B., and Pundir, C. S. (2013) An amperometric glutamate biosensor based on immobilization of glutamate oxidase onto carboxylated multiwalled carbon nanotubes/gold nanoparticles/chitosan composite film modified Au electrode, *Biosens Bioelectron 47*, 496-501.

21. Govindarajan, S., McNeil, C. J., Lowry, J. P., McMahon, C. P., and O'Neill, R. D. (2013) Highly selective and stable microdisc biosensors for l-glutamate monitoring, *Sensors and Actuators B: Chemical 178*, 606-614.

22. Ryan, M., Lowry, J. P., and O'Neill, R. D. (1997) Biosensor for Neurotransmitter L-Glutamic Acid Designed for Efficient Use of L-Glutamate Oxidase and Effective Rejection of Interference, *Analyst 122*, 1419-1424.

23. Hascup, E. R., Hascup, K. N., Talauliker, P. M., Price, D. A., Pomerleau, F., Quintero, J. E., Huettl, P., Gratton, A., Strömberg, I., and Gerhardt, G. A. (2013) Sub-Second Measurements of Glutamate and Other Neurotransmitter Signaling Using Enzyme-Based Ceramic Microelectrode Arrays, *80*, 179-199.

24. Wassum, K. M., Tolosa, V. M., Wang, J., Walker, E., Monbouquette, H. G., and Maidment, N. T. (2008) Silicon Wafer-Based Platinum Microelectrode Array Biosensor for Near Real-Time Measurement of Glutamate in Vivo, *Sensors (Basel) 8*, 5023-5036.

25. Tseng, T. T., Chang, C. F., and Chan, W. C. (2014) Fabrication of implantable, enzyme-immobilized glutamate sensors for the monitoring of glutamate concentration changes in vitro and in vivo, *Molecules 19*, 7341-7355.

26. Weltin, A., Kieninger, J., and Urban, G. A. (2016) Microfabricated, amperometric, enzyme-based biosensors for in vivo applications, *Anal Bioanal Chem 408*, 4503-4521.

27. De Corcuera, J. I. R., Cavalieri, R. P., and Powers, J. R. (2005) Improved platinization conditions produce a 60-fold increase in sensitivity of amperometric biosensors using glucose oxidase immobilized in poly-o-phenylenediamine, *Journal of Electroanalytical Chemistry 575*, 229-241.

28. Croce, R. A., Jr., Vaddiraju, S., Papadimitrakopoulos, F., and Jain, F. C. (2012) Theoretical analysis of the performance of glucose sensors with layer-by-layer assembled outer membranes, *Sensors (Basel) 12*, 13402-13416.

29. Bacha, S., Montagne, M., and Bergel, A. (1996) Modeling Mass Transfer with Enzymatic Reaction in Electrochemical Multilayer Microreactors, *AIChE Journal 42*, 2967-2976.

30. Gros, P., and Bergel, A. (1995) Improved Model of a Polypyrrole glucose oxidase modified electrode, *Journal of Electroanalytical Chemistry 386*, 65-73.

31. Leypoldt, J. k., and Gough, D. A. (1984) Model of a Two-Substrate Enzyme Electrode for Glucose, *Anal. Chem 56*, 2896-2904.

32. Marchesiello, M., and Genies, E. (1993) A theoretical model for an amperometric glucose sensor using polypyrrole as the immobilization matrix, *J. Electroanal.Chem. 358*, 35-48.

33. Phanthong, C., and Somasundrum, M. (2003) The steady state current at a microdisk biosensor, *Journal of Electroanalytical Chemistry 558*, 1-8.

34. Gooding, J. J., Hall, E. A. H., and Hibbert, D. B. (1998) From Thick Films to Monolayer Recognition Layers in Amperometric Enzyme Electrodes, *Electroanalysis 10*, 1130-1136.

35. Baronas, R., Ivanauskas, F., Ivanauskas, F., and Kulys, J. (2004) The effect of diffusion limitations on the response of amperometric biosensors with substrate cyclic conversion, *Journal of Mathematical Chemistry 35*, 199-213.

36. Cambiaso, A., Delfino, L., Grattarola, M., Verreschi, G., Ashworth, D., Maines, A., and Vadgama, P. (1996) Modelling and simulation of a diffusion limited glucose biosensor, *Sensor Actuat B-Chem 33*, 203-207.

37. Bergel, A., and Comtat, M. (1984) Theoretical Evaluation of Transient Responses of an Amperometric Enzyme Electrode, *Analytical Chemistry 56*, 2904-2909.

38. Jablecki, M., and Gough, D. A. (2000) Simulations of the frequency response of implantable glucose sensors, *Analytical Chemistry 72*, 1853-1859.

39. Bartlett, P. N., and Whitaker, R. G. (1987) Electrochemical Immobilization of Enzymes .1. Theory, *Journal of Electroanalytical Chemistry 224*, 27-35.

40. Mell, L. D., and Maloy, J. T. (1976) Amperometric Response Enhancement of Immobilized Glucose Oxidase Enzyme Electrode, *Analytical Chemistry 48*, 1597-1601.

41. Mell, L. D., and Maloy, J. T. (1975) Model for Amperometric Enzyme Electrode Obtained through Digital-Simulation and Applied to Immobilized Glucose Oxidase System, *Analytical Chemistry 47*, 299-307.

42. Hall, S. B., Khudaish, E. A., and Hart, A. L. (1998) Electrochemical oxidation of hydrogen peroxide at platinum electrodes. Part 1. An adsorption-controlled mechanism, *Electrochimica Acta 43*, 579-588.

43. Burmeister, J. J., and Gerhardt, G. A. (2001) Self-Referencing Ceramic-Based Multisite Microelectrodes or the detection and Elimination of Interferences from the Measurement of L-Glutamate and other Analytes, *Anal. Chem 73*, 1037-1042.

44. Tolosa, V. M., Wassum, K. M., Maidment, N. T., and Monbouquette, H. G. (2013) Electrochemically deposited iridium oxide reference electrode integrated with an electroenzymatic glutamate sensor on a multi-electrode array microprobe, *Biosens Bioelectron 42*, 256-260.

45. Weltin, A., Kieninger, J., and Urban, G. A. (2016) Microfabricated, amperometric, enzyme-based biosensors for in vivo applications, *Anal Bioanal Chem 408*, 4503-4521.

46. McAteer, K., and O'Neill, R. D. (1996) Strategies for Decreasing Ascorbate Interference at Glucose Oxidase-Modified Poly(o-phenylaminediamene)-coated Electrodes, *Analyst 121*, 773-777.

47. Lowry, J. P., McAteer, K., Atrash, S. E., Duff, A., and O'Neill, R. D. (1994) Characterization of Glucose Oxidase-Modified Poly(phenylaminediamine)-Coated Electrodes in Vitro and in Vivo: Homogeneous Interference by Ascorbic Acid in Hydrogen Peroxide Detection, *Anal. Chem 66*, 1754-1761.

48. Ford, R., Quinn, S. J., and O'Neill, R. D. (2016) Characterization of Biosensors Based on Recombinant Glutamate Oxidase: Comparison of Crosslinking Agents in Terms of Enzyme Loading and Efficiency Parameters, *Sensors-Basel 16*.

49. Ollis, D. F. (1972) Diffusion Influences in Denaturable Insolubilized Enzyme Catalysts, *Biotechnol Bioeng 14*, 871-&.

50. McMahon, C., Rocchitta, G., Serra, P. A., Kirwan, S. M., Lowry, J. P., and O'Neill, R. D. (2006) Control of the Oxygen Dependence of an Implantable Polymer/EnzymeComposite Biosensor for Glutamate, *Anal. Chem 78*, 2352-2359.

51. Hinzman, J. M., Thomas, T. C., Burmeister, J. J., Quintero, J. E., Huetti, P., Pomerleau, F., Gerhardt, G. A., and Lishitz, J. (2010) Diffuse Brain Injury Elevates Tonic Glutamate Levels and Potassium-Evoked Glutamate Release in Discrete Brain Regions at Two Days Post-Injury: An Enzyme-Based Microelectrode Array Study, *J. Neurotrauma 27*, 889-899.

52. Zimmerman, J. B., and Wightman, R. M. (1991) Simultaneous Electochemical Measurements of Oxygen and Dopamine in Vivo, *Analytical Chemistry 63*, 24-28.

53. Kile, B. M., Walsh, P. L., McElligott, Z. A., Bucher, E. S., Guillot, T. S., Salahpour, A., Caron, M. G., and Wightman, R. M. (2012) Optimizing the Temporal Resolution of Fast-Scan Cyclic Voltammetry, *ACS Chem Neurosci 3*, 285-292.

54. Wakao, N., and Smith, J. M. (1962) Diffusion in Catalyst Pellets, *Chemical Engineering Science 17*, 825-834.

55. Parker, J. W., and Schwartz, C. S. (1987) Modeling the Kinetics of Immobilized Glucose-Oxidase, *Biotechnol Bioeng 30*, 724-735.

56. Hall, S. B., Khudaish, E. A., and Hart, A. L. (1998) Electrochemical oxidation of hydrogen peroxide at platinum electrodes. Part II: effect of potential, *Electrochimica Acta 43*, 2015-2024.

57. Bard, A. J., and Faulkner, L. R. (2001) *Electrochemical methods : fundamentals and applications*, 2nd ed., Wiley, New York.

58. Cussler, E. L. (1997) *Diffusion: Mass Transfer in Fluid Systems*, 2nd Edition ed., Cambridge University Press.

59. Sethuraman, V. A., Khan, S., Jur, J. S., Haug, A. T., and Weidner, J. W. (2009) Measuring Oxygen, Carbon Monoxide and Hydrogen Sulfide Diffusion Coefficient and Solubility in Nafion Membranes, *Electrochimica Acta 54*, 6850-6860.

60. Gode, P., Lindbergh, G., and Sundholm, G. (2002) In-situ measurements of gas permeability in fuel cell membranes using a cylindrical microelectrode, *Journal of Electroanalytical Chemistry 518*, 115-122.

61. Poggi, C. G., and Slade, K. M. (2015) Macromolecular crowding and the steady-state kinetics of malate dehydrogenase, *Biochemistry 54*, 260-267.

62. Wilcox, A. E., LoConte, M. A., and Slade, K. M. (2016) Effects of Macromolecular Crowding on Alcohol Dehydrogenase Activity Are Substrate-Dependent, *Biochemistry 55*, 3550-3558.

63. Aumiller, W. M., Jr., Davis, B. W., Hashemian, N., Maranas, C., Armaou, A., and Keating, C. D. (2014) Coupled enzyme reactions performed in heterogeneous reaction media: experiments and modeling for glucose oxidase and horseradish peroxidase in a PEG/citrate aqueous two-phase system, *J Phys Chem B 118*, 2506-2517.

64. Ikemoto, H., Mossin, S. L., Ulstrup, J., and Chi, Q. (2014) Probing structural and catalytic characteristics of galactose oxidase confined in nanoscale chemical environments, *RSC Advances 4*, 21939.

65. Minton, A. P. (2001) The influence of macromolecular crowding and macromolecular confinement on biochemical reactions in physiological media, *J Biol Chem 276*, 10577-10580.

66. Hall, S. B., Khudaish, E. A., and Hart, A. L. (1999) Electrochemical oxidation of hydrogen peroxide at platinum electrodes. Part IV: phosphate buffer dependence, *Electrochimica Acta 44*, 4573-4582.

67. Hall, S. B., Khudaish, E. A., and Hart, A. L. (2000) Electrochemical oxidation of hydrogen peroxide at platinum electrodes. Part V: inhibition by chloride, *Electrochimica Acta 45*, 3573-3579.

68. Diaz, L. A., and Botte, G. G. (2015) Mathematical modeling of ammonia electrooxidation kinetics in a Polycrystalline Pt rotating disk electrode, *Electrochimica Acta 179*, 519-528.

69. Verbrugge, M. W., and Hill, R. F. (1988) Ion and Solvent Transport in Ion-Exchange Membranes .2. A Radiotracer Study of the Sulfuric-Acid, Nafion-117 System, *J Electrochem Soc 135*, C345-C345.

70. Stoodley, P., Yang, S., Lappin-Scott, H., and Lewandowski, Z. (1997) Relationship Between Mass Transfer Coefficient and Liquid Flow Velocity in Heterogeneous Biofilms Using Microelectrodes and Confocal Microscopy, *Biotechnology and Bioengineering 56*, 681-688.

71. Bird, R. B., Stewart, W. E., and Lightfoot, E. N. (2002) *Transport phenomena*, 2nd, Wiley international ed., J. Wiley, New York.

72. Hallik, A., Alumaa, A., Kurig, H., Jänes, A., Lust, E., and Tamm, J. (2007) On the porosity of polypyrrole films, *Synthetic Metals 157*, 1085-1090.

73. Wang, J., Myung, N. V., Yun, M., and Monbouquette, H. G. (2005) Glucose oxidase entrapped in polypyrrole on high-surface-area Pt electrodes: a model platform for sensitive electroenzymatic biosensors, *Journal of Electroanalytical Chemistry 575*, 139-146.

Chapter 3: Electroenzymatic glutamate sensing at near the theoretical performance limit

Chapter 3 is a manuscript published with the following citation:

I-Wen Huang, **Mackenzie Clay**, Siqi Wang, Yuwan Guo, Jingjing Nie and Harold G. Monbouquette, "Electroenzymatic glutamate sensing at near the theoretical performance limit," Analyst, 2020, 145, 2602-2611.

Mackenzie Clay developed the mathematical model, performed the simulations, and contributed to the writing of the manuscript and analysis of results.

Abstract

The sensitivity and response time of glutamate sensors based on glutamate oxidase immobilized on planar platinum microelectrodes have been improved to near the theoretical performance limits predicted by a detailed mathematical model. Microprobes with an array of electroenzymatic sensing sites have emerged as useful tools for the monitoring of glutamate and other neurotransmitters *in vivo*; and implemented as such, they can be used to study many complex neurological diseases and disorders including Parkinson's disease and drug addiction. However, less than optimal sensitivity and response time has limited the spatiotemporal resolution of these promising research tools. A mathematical model has guided systematic improvement of an electroenzymatic glutamate microsensor constructed with a 1–2 μm-thick crosslinked glutamate oxidase layer and underlying permselective coating of polyphenylenediamine and Nafion reduced to less than 200 nm thick. These design modifications led to a nearly 6-fold improvement in sensitivity to 320±20 $nA\mu M^{-1}cm^{-2}$ at 37°C and a ~10-fold reduction in response time to 80 ± 10 ms. Importantly, the sensitivity and response times were attained while maintaining a low detection limit and excellent selectivity. Direct

measurement of the transport properties of the enzyme and polymer layers used to create the biosensors enabled improvement of the mathematical model as well. Subsequent model simulations indicated that the performance characteristics achieved with the optimized biosensors approach the theoretical limits predicted for devices of this construction. Such high-performance glutamate biosensors will be more effective *in vivo* at a size closer to cellular dimension and will enable better correlation of glutamate signaling events with electrical recordings.

3.1 Introduction

As was articulated clearly several years ago,[1] an understanding of information processing in the brain can be had only by unraveling of the interrelated roles of chemical neurotransmission and neuronal electrical activity. Great strides have been made in recording activity simultaneously from large numbers of interconnected neurons through millisecond timescale measurements of action potentials or intracellular Ca^{2+} changes.[2-7] However, corresponding tools to monitor chemical neurotransmission with the cellular-scale spatial resolution and the single-digit millisecond timescale of synaptic signaling events have yet to emerge.[8-11] This spatiotemporal mismatch has made problematic the desired correlation of chemical neurotransmission with neuronal activity. The problem is made particularly challenging by the broad array of chemical species involved that must be detected selectively against the complex background of brain extracellular fluid. Microdialysis and related techniques have been valuable tools for neurotransmitter measurements, although the typical minute-to-minute time resolution limits the detection of rapid neurotransmission events which are known to be much faster. [12,13] Electrochemical devices based on microelectrode arrays (MEAs) with electroenzymatic sensing sites on silicon or ceramic microprobes have emerged as useful tools for the monitoring of glutamate and choline (as surrogate for acetylcholine) *in vivo*. Our group

and others have successfully demonstrated the feasibility of MEAs with response times in the ~1 s range for use in the study of complex neurological diseases and disorders including Parkinson's disease and drug addiction.[14-16] Yet historically, these sensors have lacked the temporal resolution to associate unambiguously release events with local field potentials, and certainly not action potentials. Further, sensitivity limitations have required sensing sites on probes to be much larger than cellular dimension, thereby limiting spatial resolution. This report addresses these challenges through several-fold improvement in the design of a selective electroenzymatic sensor for the important excitatory neurotransmitter, glutamate (Glut).

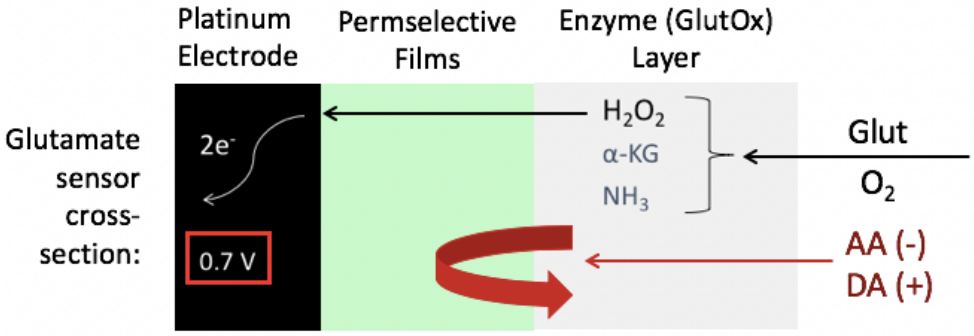

Figure 3.1. Schematic of an electroenzymatic glutamate (Glut) sensor with permselective films and a glutamate oxidase (GlutOx) enzyme layer.

An electroenzymatic Glut sensor consists of an electrode upon which one or more permselective films are deposited as well as an immobilized enzyme (Fig. 3.1). Typically, glutamate oxidase (GlutOx) serves as the enzyme and selective molecular recognition element that catalyzes Glut oxidation to α-ketoglutarate with production of hydrogen peroxide (H_2O_2). This recognition event is transduced into an electrical current signal most often through the electrooxidation of H_2O_2 by an underlying Pt electrode poised at oxidizing potential. In this way, Glut concentration may be correlated with measured current magnitude. However, the Pt electrode generally must be coated with permselective films to allow H_2O_2 to pass but to reject

electrooxidizable interfering species common to brain extracellular fluid such as ascorbic acid (AA) that could give rise to false signals. Due to the restricted di!usion of Glut through the immobilized GlutOx layer and H_2O_2 through both the enzyme layer and the underlying permselective films, bio- sensor performance is impacted significantly by sensor con- struction. A variety of polymeric materials have been used as permselective films including polypyrrole (PPy), polyphenylenediamene (PPD) and Nafion.[17-19] GlutOx is most commonly immobilized on the electrode by spreading a mixture of enzyme and bovine serum albumin (BSA) on the coated electrode surface followed by crosslinking with glutaraldehyde. (GAH).[9,11,15,16,19-22]

Our previous simulations of then currently representative Glut sensors of the type illustrated in Fig. 3.1 suggested that the majority of the Glut diffusing into the enzyme layer is consumed near its outer edge, and that the H_2O_2 concentration in the layer peaks closer to the bulk solution than to the Pt electrode surface.[23] The steeper H_2O_2 concentration gradient in the direction of the bulk solution and the larger corresponding flux indicated that the vast majority of H_2O_2 generated by the GlutOx-catalyzed Glut oxidation reaction escapes from the sensor site and is not available at the Pt electrode surface to give rise to a current signal. These simulations strongly suggest that reducing the enzyme layer thickness while maximizing active enzyme concentration to improve H_2O_2 capture would be an effective strategy to reduce response time and to improve sensitivity.

This report describes sensors fabricated with thinner permselective films and enzyme layers based on the guidance of our simulations. In order to characterize these new sensors, the mass transport properties of H_2O_2 within these permselective and immobilized enzyme films were evaluated experimentally using rotating disk electrodes (RDEs). These values provided improved parameter estimates for our mathematical model, and enabled demonstration that the new Glut biosensors had been improved to near the theoretical performance limit.

3.2 Experimental

3.2.1 Reagents

Nafion (5 wt% in lower aliphatic alcohols and 15–20% water), m-phenylenediamine (PD), pyrrole (Py), bovine serum albumin (BSA) lyophilized powder, glutaraldehyde solution (GAH), L-glutamic acid (Glut), L-ascorbic acid (AA), 3-hydroxytyramine (dopamine, DA), sodium phosphate dibasic, sodium chloride, HCl (36.5–38%), and hydrogen peroxide solution (30%) were purchased from Sigma-Aldrich (St Louis, MO). L-Glutamate oxidase (EC 1.4.3.11) was obtained from US Biological. Bis(sulfosuccinimidyl) suberate (BS3) was purchased from Thermo Fisher Scientific (Pittsburgh, PA). Ag/AgCl glass-bodied reference electrodes with NaCl electrolyte (3 M) and a 0.5 mm-diameter Pt wire auxiliary electrode were obtained from BASi (West Lafayette, IN). Sodium phosphate buffer (PBS, pH 7.4) was composed of 50 mM sodium phosphate dibasic and 100 mM sodium chloride. Four-inch silicon wafers (p-type boron doped; orientation h100i; thickness 150 μm) were purchased from Silicon Valley Microelectronics (Santa Clara, CA). The platinum rotating disk electrodes (RDEs) (5.0 mm disk, 12.0 mm OD PEEK shroud) were purchased from Pine Research (Durham, NC). Microcloth (PSA, 2-7/8″) for electrode polishing was purchased from Buehler (Lake Bluff, Illinois).

3.2.2 Instrumentation

The RDE system (model AFMSRX) was purchased from Pine Research (Durham, NC). Microsensors were calibrated using a Versatile Multichannel Potentiostat (model VMP3) equipped with the ‘p’ low current option and N’Stat box driven by EC-LAB software (Bio-Logic USA, LLC, Knoxville, TN) in a three-electrode configuration consisting of the sensing electrode, a Pt wire auxiliary electrode, and a Ag/AgCl reference electrode. The film thicknesses on microelectrodes and RDEs were measured using a SEM (Nova 600 SEM/FIB System), a Dektak 8 stylus profilometer, and/or a Wyko NT300 optical profiling system.

3.2.3 Sensor preparation

The silicon-based microelectrode arrays used in this work were manufactured in house using microelectromechanical system (MEMS) techniques. The fabrication and array details are described in our previous work.[11] The microelectrode array probes were 150μm thick, 140 μm wide and 9 mm long, with four, 6000 μm^2 (40 μm x 150 μm) Pt recording sites arranged in pairs at the tip (Fig. 3.2). A PPD film first was electrodeposited on Pt microelectrodes from a 5 mM PD solution in phosphate buffered saline (0.1 M PBS) by holding the voltage constant at 0.85 V vs. Ag/AgCl until the desired total charge was transferred (7.6 x 10^{-7} coulombs). Alternatively, a PPy film was electrodeposited from 200 mM pyrrole in PBS at 0.85 V vs. Ag/AgCl for 5 min. A Nafion layer then was applied by dip-coating a 2% Nafion solution (diluted from stock with 4 : 1 IPA : water) 3x for PPy/Nafion and only 1x for PPD/Nafion, followed by annealing at 115 °C for 20 min (115 °C-Nafion) or 180 °C for 4 min (180 °C-Nafion). Next, an immobilized GlutOx coating was deposited manually by loading a GlutOx and BSA mixture (dissolved in PBS) on the microelectrodes and crosslinking with 174 mM BS3 or 5% GAH vapor for 1 min. After the final crosslinking step, sensors were stored dry at 4 °C for 48 h prior to testing.

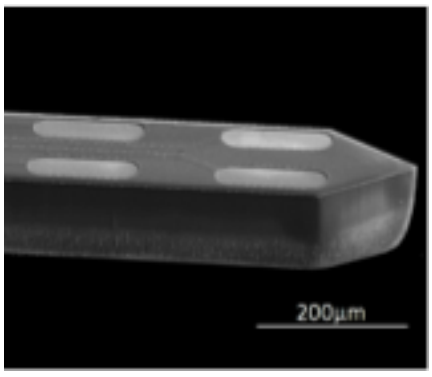

Figure 3.2. Scanning electron microscopy (SEM) image of the microelectrode array probe.

3.2.4 Electrochemical measurement

To determine sensor selectivity and sensitivity, a constant potential of 0.7 V vs. Ag/AgCl was applied to the sensors in stirred PBS buffer solution. After current stabilization, AA, DA, Glut or H_2O_2 were added to give final concentrations of 250 μM AA, 10 μM DA, 20–60 μM Glut and 20 μM H_2O_2. The selected concentrations of AA and DA were chosen to be reflective of those found *in vivo*.[24-26] To test the response time of the Glut microsensors, two peristaltic pump-driven streams of solution (PBS buffer and analyte) flowing from separate pipette tips were positioned close to the microprobe tip (Fig. 3.3). Rapid step changes in analyte concentration at the microsensors were achieved by alternating between PBS buffer and analyte streams by turning pumps on and off.[22]

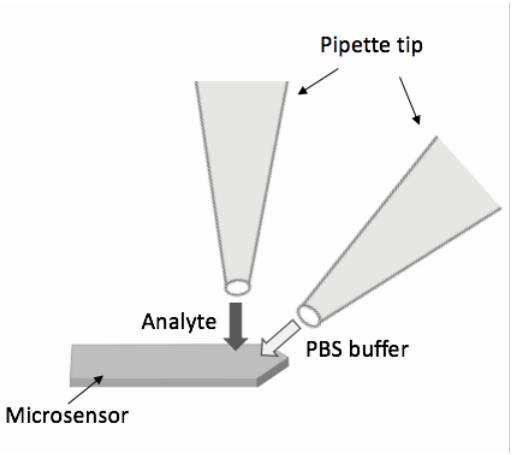

Figure 3.3. Testing set-up for microsensor response time. Rapid switching of solution flow onto the microprobe was controlled by alternating between pumped streams of PBS buffer and analyte solution.

3.2.5 Diffusion coefficient measurement

Diffusion of H_2O_2 within the PPD, Nafion or immobilized enzyme coatings was determined using a Pt RDE. The Pt RDE was polished using a microcloth and a 0.05 μm particle suspension, followed by rinsing with DI water and sonication in isopropyl alcohol. Next, a PPD, Nafion or enzyme film was deposited onto the electrode surface in the same way described in the sensor preparation section above. Linear sweep voltammetry (LSV) from 0.2 V to 0.9 V *vs.* Ag/AgCl was used as well as constant potential amperometry with varied rotation

rate (see Results and discussion). Aftermath software was used for collection of voltammetric data (Pine Research, Durham, NC).

3.2.6 Mathematical Model and Simulations

Simulations of sensor performance were generated using an established model for electroenzymatic sensors with updated values for transport parameters based on this work, adjusted for temperature dependence.[23] In the model, sets of partial differential equations describe the one-dimensional transport and reaction rates of Glut, O_2, and H_2O_2 within separately considered PPD, Nafion, and immobilized enzyme coatings. Boundary conditions simulate a step- change in Glut concentration from 0 to 20 μM on the microsensor surface at t = 0. Numerical solutions of model equations were generated using COMSOL (COMSOL, Inc. Los Angeles).

3.3 Results and Discussion

3.3.1 Optimization of permselective films

Our published Glut sensor modeling study showed that permselective film thicknesses and transport properties are important parameters to address in sensor optimization.[23] Dopamine (DA) and ascorbic acid (AA) are two common, electroactive interferents found in brain extracellular fluid at relatively high concentration that should be rejected by permselective films coated on the sensing electrode surface (Fig. 3.1). For what we will refer to as the base-case microsensor in this study, a PPy film and a Nafion overlayer annealed at 180 °C for 4 min (180 °C-Nafion) were used to reject DA and AA, respectively, yet to permit transport of H_2O_2 to the Pt electrode surface. However, this PPy/180 °C-Nafion combination resulted in slow H_2O_2 diffusion to the electrode surface and low Glut sensitivity, mostly due to the overly thick Nafion coating necessary for adequate AA rejection, which was measured by SEM at 304 ± 87 nm (*n* =

3). Alternatively, when PPD was used as the underlying permselective film, a much thinner 180 °C-Nafion coating (96 ± 10 nm (n = 5)) was adequate, thereby improving H_2O_2 sensitivity ~3-fold from 121 ± 52 nA μM^{-1} cm^{-2} (n = 4) to 372 ± 70 nA μM^{-1} cm^{-2} (n = 15) (Fig. 3.4).

The Nafion annealing temperature also impacts sensor performance significantly. In order to improve the mechanical stability of Nafion coatings and to reduce water solubility, dip-coated Nafion films normally must be heated above the glass transition temperature (T_g = 109 °C for protonated Nafion) to anneal them.[27,28] However, the choice of annealing temperature and duration of the annealing process also affects Nafion properties. As illustrated in Fig. 4, we found that lowering the annealing temperature from 180 °C to 115 °C while increasing the baking time from 4 min to 20 min resulted in a further improvement of the H_2O_2 sensitivity by ~25% to 536 ± 69 nA μM^{-1} cm^{-2} (n = 15). The improved annealing process resulted in an even thinner final Nafion layer thickness of 71 ± 11 nm (n = 5) while retaining excellent selectivity against AA. This result is in agreement with the recently published work of Leppänen et al. showing that very thin Nafion films can retain effective anion exclusion properties.[29]

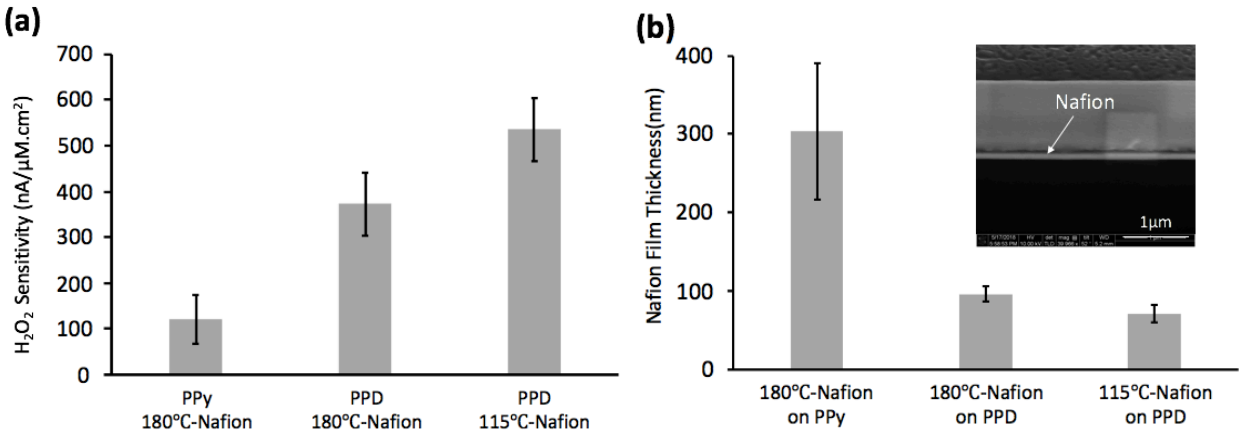

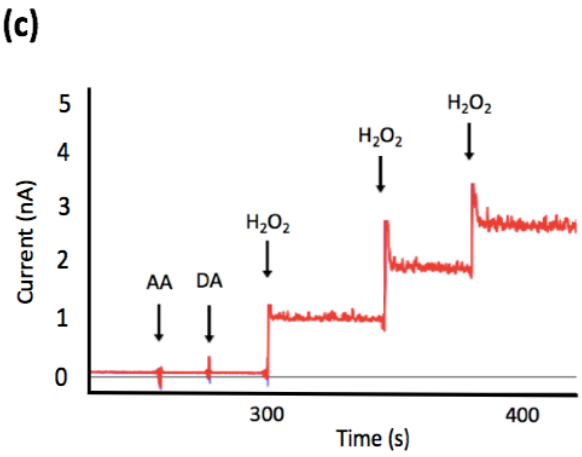

Figure 3.4. (a) Comparison of H2O2 sensitivity among sensors prepared with PPy/180 °C-Nafion, PPD/180 °C-Nafion, and PPD/115 °C-Nafion. (b) The Nafion thicknesses corresponding to the three different sensor preparations. Inset: SEM image of a Nafion film on Pt. (c) Representative current responses of PPD/115 °C-Nafion coated sensors to 250 μM AA, 5 μM DA, and H2O2 administered in 20 μM concentration increments. (Error bars shown are 95% confidence intervals.)

3.3.2 Hydrogen peroxide diffusion coefficient in permselective films and the crosslinked GlutOx layer

In addition to electrode coating thicknesses, measurements of H_2O_2 diffusivities in the permselective films and crosslinked enzyme layers are needed to improve the accuracy of sensor simulations and to better guide sensor optimization. There are three “resistances” that can limit the rate of H_2O_2 oxidation at the coated Pt electrode: (1) the transport of H_2O_2 in the external diffusion boundary layer just above the coated electrode surface, (2) the diffusion of H_2O_2 within the deposited films and (3) the H_2O_2 electrooxidation kinetics at the Pt surface. The overall current density can be described in terms of these serial resistances by a form of the Koutecky–Levich equation.[17,30-35]

$$\frac{1}{I} = \frac{1}{I_k} + \frac{1}{I_f} + \frac{1}{I_l} \tag{3.1}$$

where I is the measured current, I_k is the current in the absence of any mass transfer limitations, I_f is the current when limited totally by diffusion in a film deposited on the electrode and I_l is the current when limited totally by mass transfer through the liquid boundary layer on the coated or uncoated electrode surface. Further, I_l can be modeled using the Levich equation, and eqn (3.1) then becomes[35]

$$\frac{1}{I} = \frac{1}{I_k} + \frac{1}{I_f} + \frac{1}{B_L \omega^{1/2} C} \tag{3.2}$$

where B_L is the Levich constant, ω is the electrode rotation rate (radians per s), and C is the bulk concentration of H_2O_2. The Levich constant is a function of H_2O_2 diffusivity in the bulk liquid, D_l, and the kinematic viscosity of the liquid medium, v, such that[35]

$$B_L = 0.62 n F A D_l^{2/3} \nu^{-1/6} \tag{3.3}$$

where n is the stoichiometric number of electrons transferred in the electrode reaction, F is Faraday's constant, and A is the electrode surface area.

Representative current–potential (I–E) curves corresponding to bare Pt and Nafion-coated Pt RDEs in 0.2 mM H_2O_2 are shown in Fig. 3.5 and 3.6, respectively. The anodic current increases initially as the voltage and the electrode rotation rate are increased as expected, while water dissociation occurs in the potential region above 0.85–1.0 V *vs*. Ag/AgCl. The limiting current condition (plateau current) on bare Pt (Fig. 3.5) is achieved when the current is limited by the rate at which H_2O_2 is transported to the Pt electrode surface. When Nafion films are deposited on the Pt surface, these films ultimately limit the current achievable; and the electrode rotation rate, which influences external transport, has little to no impact (Fig. 3.6a). These results also show that diffusion of H_2O_2 was more hindered in 180 °C-Nafion than 115 °C-Nafion.

In order to obtain estimates for the diffusivities in Nafion, the current was set at 0.7 V *vs*. Ag/AgCl while the electrode rotation rate was varied. The plot of the inverse of the recorded current versus the inverse square root of the electrode rotation rate shows a linear relationship

as expected from Equation 3.2. Since the bathing solution (0.2 mM H_2O_2 in PBS) is unchanged during the whole experiment, the slopes of the lines are about the same (Fig. 3.6b). For the bare Pt RDE, extrapolation to infinite rotation rate yields an inverse current intercept close to zero, which indicates that the system was limited by mass transfer through the liquid boundary layer. Thus, to a good approximation, I_f may be obtained directly from the plot intercept for the coated electrodes assuming that external mass transport to the coated electrodes is approximately the same as that for bare Pt. Since I_f can be defined as a function of Nafion film thickness, δ, and the H2O2 effective diffusivity in the Nafion film, D_f, according to,[35]

$$I_f = nFAD_fC/\delta \tag{3.4}$$

an estimate for D_f may be calculated from the intercept of the Koutecky–Levich plot.

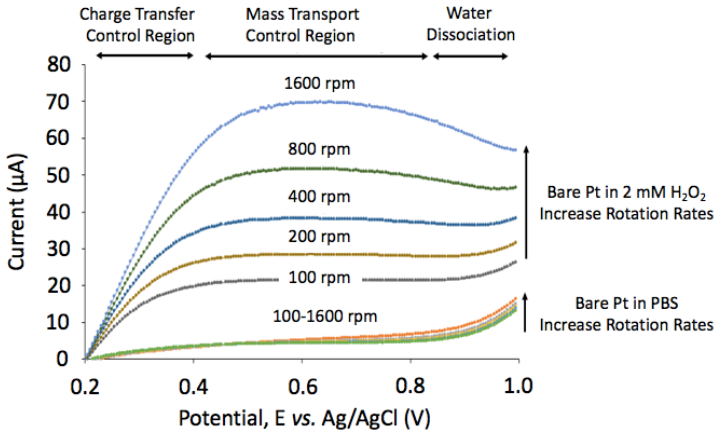

Figure 3.5. Representative current vs. potential curves showing the charge transfer, mass transport controlled and water dissociation regions at a bare Pt RDE using a potential sweep rate of 20 mV/s with rotation rates of 100, 200, 400, 800, 1600 rpm in PBS and 0.2 mM H_2O_2 solution.

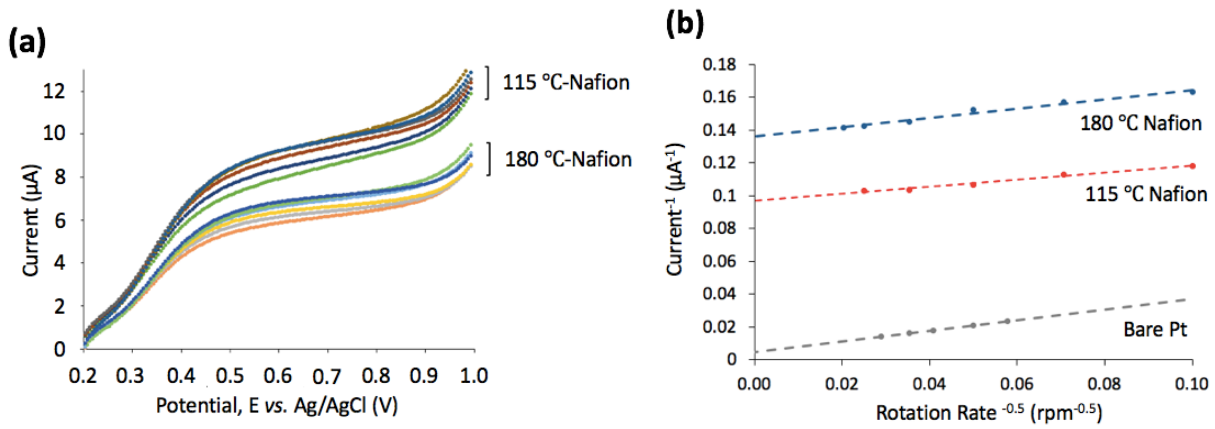

Figure 3.6. (a) Oxidation of 0.2 mM H_2O_2 in PBS (pH 7.4) at Nafion-coated Pt RDEs annealed at 180°C and 115°C using a potential sweep rate of 20 mV/s with rotation rates of 100, 200, 400, 800, 1600, 2400 rpm. (b) Koutecky-Levich plot of data for a bare Pt RDE (gray trace) and for 180°C-Nafion/Pt (blue trace) and 115°C-Nafion/Pt (red trace) RDEs. Current data were obtained at 0.7 V vs. Ag/AgCl.

For the larger RDE electrodes, the thickness difference between the dip-coated 180 °C-Nafion and 115 °C-Nafion films were more obvious at ~2 μm and ~1 μm, respectively, than what was observed for our micromachined microelectrode array probes, probably due to the substantial differences in geometry. The average values of D_f were found to be $(1.7 \pm 0.2)' 10^{-7}$ $cm^2 s^{-1}$ (n = 3) for 180 °C-Nafion and $(1.3 \pm 0.2)' 10^{-7}$ $cm^2 s^{-1}$ (n = 3) for 115 °C-Nafion. Since these effective diffusivities are approximately the same, these results highlight the importance of the thinner 115 °C-Nafion films that still show excellent selectivity against interferents. Also, these results are in rough agreement with literature values for effective diffusivity of the slightly smaller O_2 molecule in Nafion in the range of ~2 x 10^{-7} - ~2 x 10^{-6} $cm^2 s^{-1}$.[31,36,37] The broad range of values is due primarily to the different preparation conditions for the films and membranes studied.

The data and estimated diffusivities were further examined by comparing the values of I_k and the slope ($1/B_L$) to expected values. Specifically, I_k is the current limited by the kinetics of

the electrooxidation of H_2O_2 on Pt, assuming no mass transfer limitations, so the value of I_k should match the value calculated using published reaction kinetics.[38] RDE data gave I_k = 0.208 mA, in general agreement with that derived from published data of 0.273 mA. The measured slope was validated by checking consistency with the known value of H_2O_2 diffusivity at room temperature in water, 1.43 x 10^{-5} cm^2 s^{-1}.[39] Based on the measured slope and eqn (3.3), a comparable diffusivity of 0.94 x 10^{-5} cm^2 s^{-1} was obtained. Thus, this RDE analysis appears to be giving at least semiquantitative results that are well within an order of magnitude of those expected.

A similar experimental procedure was followed to obtain estimates for H_2O_2 effective diffusivities in the PPD film and in the crosslinked GlutOx deposit. For the PPD film, the mean value of the H_2O_2 diffusion coefficient was found to be (1.7 ± 0.3) x 10^{-8} cm^2 s^{-1} (n = 3), based on the measured film thickness of ~20 nm. This result is in agreement with literature data for H_2O_2 diffusivity in overoxidized polypyrrole (OPPy) (10^{-8} cm^2 s^{-1}), which is a similar polymer.[17] The average estimated value for the effective H_2O_2 diffusion coefficient in the GAH-crosslinked GlutOx layer on the Pt RDE was found to be ~1.6 x 10^{-6} cm^2 s^{-1}, which is about an order of magnitude less than that in free solution due to a deposit porosity less than unity as well as its substantial tortuosity. The effective diffusivities of Glut and O_2 in permselective films and the GlutOx layer were obtained from the H_2O_2 effective diffusivities scaled by the ratio of the molecular diffusivities with that of H2O2. These measured values for deposit thicknesses and effective diffusivities provide improved parameters for our simulation studies described below.

3.3.3 Effect of Enzyme loading and Activity

Most commonly, GlutOx is immobilized on electrodes by spreading a mixture of GlutOx and BSA on the electrode surface and crosslinking with GAH. However, the many variations of methods used produces layers of different compositions and thicknesses that directly affect the

sensor performance. Typical reported immobilized enzyme layer thicknesses have been in the 10-20 μm range. However, our simulation results suggest immobilized GlutOx layers 1-3 μm thick may be optimal to ensure high sensitivity while achieving rapid response time (if GlutOx activity is well preserved during the immobilization process).[23] Therefore, our experimental strategy was first to improve enzyme activity retention during the immobilization process, and then to optimize systematically the layer thickness.

Homobifunctional crosslinker, BS3, which like GAH also reacts with amine groups, appeared to be a good alternative due to its longer spacer arm, 11.4 Å *vs.* 5 Å. We hypothesized that this longer spacer arm would result in less enzyme crowding and better access to enzyme active sites. Also, the BS3-crosslinked enzyme layer might be more permeable overall. Crosslinking conditions for both BS3 and GAH were investigated individually before making comparisons. GAH concentrations and vapor exposure times were varied as were BS3 concentrations to find the best conditions for use of each crosslinker. After this simple optimization procedure, sensors made with enzyme crosslinked via BS3 showed ~1.5-fold improvement in sensitivity compared to those crosslinked via GAH, which showed sensitivity of 259 ± 25 nA $\mu M^{-1}\,cm^{-2}$ (n = 11) and 196 ± 24 nA $\mu M^{-1}\,cm^{-2}$ (n = 11), respectively. Further, the importance of permselective film and enzyme layer thicknesses on sensor performance should be evident here again. Compared to our base-case sensors, a ~4-fold improvement in Glut sensitivity was achieved merely by applying a thinner permselective film and halving the enzyme layer thickness to ~5 μm even while using the inferior crosslinker, GAH (Fig. 3.7).

For our existing sensor designs, a direct investigation of the effect of deposited enzyme concentration on sensor performance can be performed easily by changing the relative proportion of GlutOx and BSA without changing enzyme layer thickness. The protein mass fraction of GlutOx (f_{glutox}) was varied from 0.02 to 0.95 for the sensors coated optimally with PPD and 115 °C-Nafion and crosslinked with BS3. Based on the experimental results shown in Fig.

3.8, Glut sensitivity goes through a peak at f_{glutox} = ~0.4. Theoretically, as GlutOx mass fraction decreases for thicker enzyme layers, more Glut diffuses deeper into the layer before being oxidized resulting in more penetration of H_2O_2 to the electrode surface, less loss back to the bulk medium, and a greater current signal.[23,40] However, for the very thin enzyme layers explored here, an optimum f_{glutox} is expected. At low enzyme mass fraction, decreased Glut sensitivity was observed due to insufficient active enzyme available to consume Glut at a high rate. On the other hand, high enzyme concentration corresponding to $f_{glutox} \geq 0.5$ was found not to be preferable either due to the fact that GlutOx does not have an abundance of surface lysines available for crosslinking, unlike BSA. The relatively low BSA concentration at high f_{glutox} led to poor crosslinking, an unstable enzyme layer, and great difficulty in gathering data for Fig. 3.8 at high enzyme concentration. As a result, f_{glutox} = 0.2 was chosen as the target level for future work since there is little compromise in sensitivity in exchange for excellent stability.

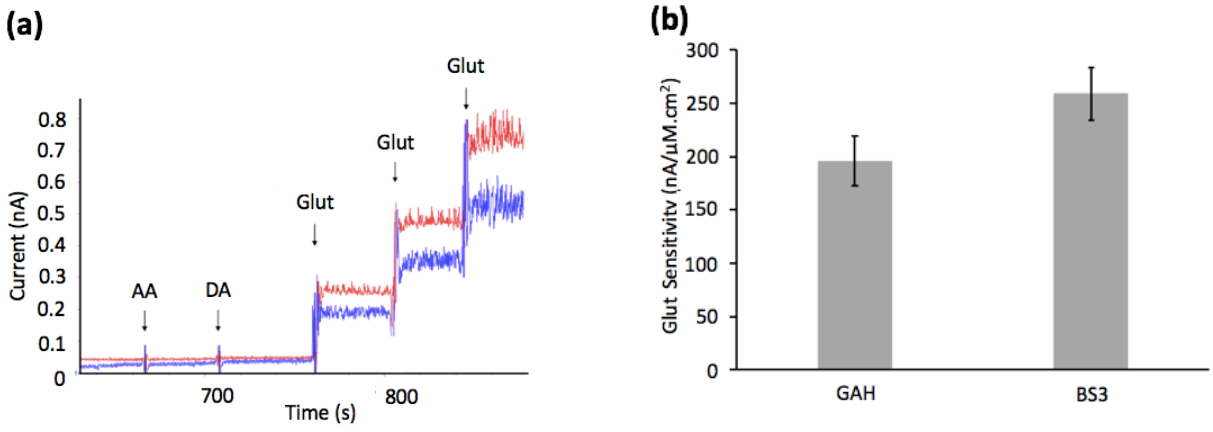

Figure 3.7. (a) Representative current response of Glut sensors crosslinked via BS3 (red trace) and GAH (blue trace) to interferents (250 μM AA and 5 μM DA), followed by three 20 μM step increases in H_2O_2 concentration. (b) Glut sensitivity comparison between BS3 and GAH crosslinked GlutOx sensors with error bars giving 95% confidence intervals. In all cases, the mass ratio of GlutOx to BSA was 1 : 4 and the enzyme layer was less than 5 μm thick.

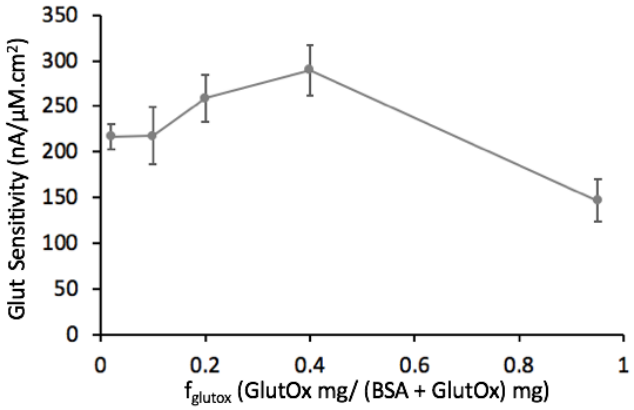

Figure 3.8. Effect of GlutOx concentration on the Glut sensitivity, where f_{glutox} is varied from 0.02 to 0.95. In all cases, sensors were crosslinked with BS3 and the layer thickness was less than 5 µm. Error bars represent 95% confidence intervals.

3.3.4 Optimal enzyme layer thickness

Our experimental results of Fig. 3.9 show the expected result that Glut sensitivity goes through an optimum with regard to enzyme layer thickness. The Glut sensitivity drops sharply for GlutOx layer thickness less than a micron and remains a roughly constant value for up to a 2 µm thickness. These results match stimulations well and are consistent with other published experimental reports showing that very thin enzyme layers realized by electropolymerization result in low sensitivity.[40,41] As discussed earlier, the decrease in Glut sensitivity with thickness for thicker GlutOx layers is due to the greater diffusional mass-transfer limitation and the loss of the majority of H_2O_2 generated in the enzyme layer back to the bulk solution. Also, the added mass-transfer resistance of a thick enzyme layer leads to a slower response time.

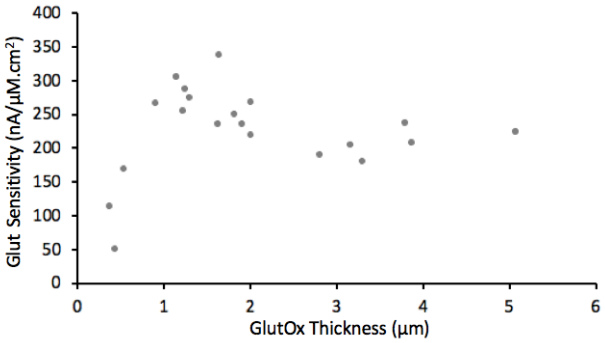

Figure 3.9. Sensor sensitivity based on the linear range of calibration curves (0-60 μM Glut) *versus* immobilized GlutOx layer thickness. In all cases, f_{glutox} = 0.2, and sensors were crosslinked with BS3.

3.3.5 Comparison in performance between the optimized and base-case sensors

Sensors with the optimal permselective film (PPD/115 °C-Nafion) topped with an enzyme layer of optimal thickness of 1-2 μm with mass fraction of GlutOx (f_{glutox}) = 0.2 and crosslinked with BS3 has led to excellent sensitivity of 320 ± 19.6 nA μM^{-1} cm^{-2} (n = 18), which is a ~6-fold improvement compared with our previously reported design (51 ± 1.96 nA μM^{-1} cm^{-2}) without sacrificing selectivity and detection limit (signal-to-noise ratio equal to 3).[11] The detection limit for the improved sensors and those previously reported are 0.70 ± 0.08 μM (n = 18) and 0.79 ± 0.31, respectively (Fig. 3.10). Noise limited improvement in detection limit despite the large increase in sensitivity achieved with the optimized sensors.

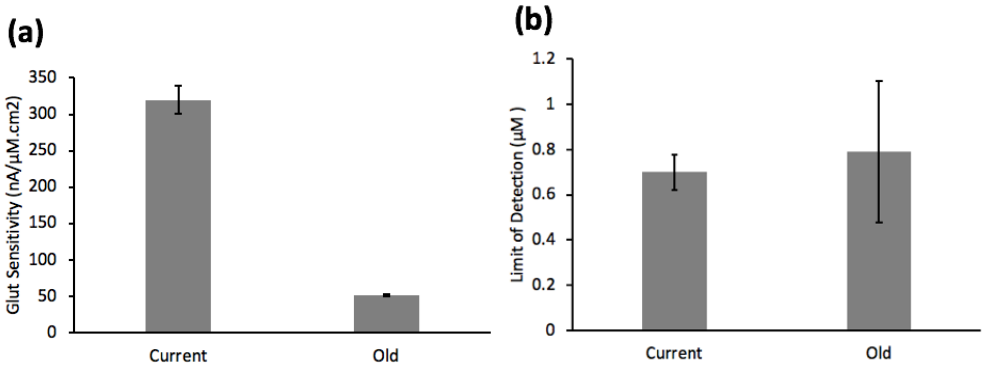

Figure 3.10. (a) Sensor sensitivity and (b) detection limit based on the linear range of the calibration curves (0-60 μM Glut) for the improved (current) and previously published[11] (old) Glut sensors. Error bars represent 95% confidence intervals.

Response time is defined here as the time for the current signal to reach 90% of its steady-state value in response to a step change in Glut from zero to 40 μM under conditions where external mass transfer is essentially eliminated. Our base case and other published response times are in the ~1 s range,[11,42] mostly due to the overly thick enzyme and permselective layers thought to be needed for high sensitivity and selectivity. Our improved sensors having thin enzyme and polymer layers enabled a faster response time of 0.080 ± 0.012 s (n = 5), which is a ~10-fold improvement over prior work (Fig. 3.11). The fact that the bare Pt response to H_2O_2 appears as a near step change as expected given very rapid electrooxidation kinetics suggests that this method for measuring response time essentially eliminates the external mass transfer resistance. In contrast, the intrinsic response of our optimized Glut biosensor is obscured by the rate of external mass transfer when the measurement is attempted in a stirred beaker or a simple flow cell. However, the response time measurement method, whether using a stirred beaker or pump-driven buffer streams (Fig. 3.3), was not seen to affect sensor calibration and therefore the determination of sensitivity. In fact, essentially the same response time was measured for our early Glut sensor design using the pump-driven bu!er streams (Fig. 3.11). The higher temporal resolution exhibited by the optimized Glut sensor will enable better correlation of Glut signaling *in vivo* with local field potentials, which occur at <100 Hz.[4] Straightforward correlation with single-unit action potentials will require improvement of response time to the single digit millisecond range, which may be attainable without sacrificing sensitivity by further optimization of these biosensors (see below).

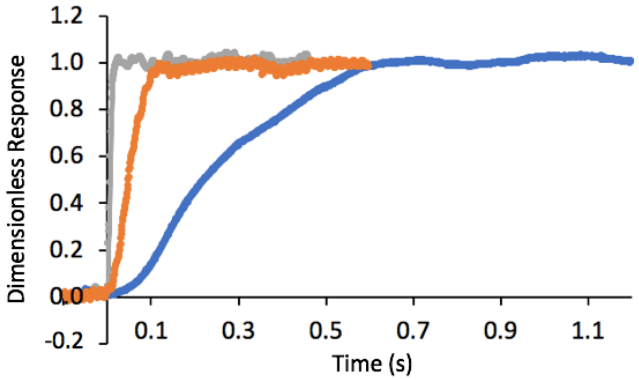

Figure 3.11. Representative sensor response to a 0-40 μM step-change in Glut concentration for base-case Glut sensor (blue trace), the improved Glut sensor (orange trace) and a step-change in H_2O_2 for bare Pt sensor (grey trace) as reference. Dimensionless response is the current divided by the steady-state current.

3.3.6 Simulation Results

Using the newly measured values of coating thicknesses and transport parameters, a mathematical model for Glut sensor performance in vitro was updated to estimate the theoretical limits of sensitivity and response time for these improved sensors.[23] For the simulations, an external mass transfer coefficient of 0.05 cm s^{-1} and the currently optimized permselective film thicknesses were used. Note that at this mass transfer coefficient value and above, there is little or no impact on predicted sensor response time. Also, an appropriate range of f_{glutox} and enzyme layer thicknesses were chosen for comparison with experimental work (Fig. 3.12). As expected, simulations predict that increasing f_{glutox} increases sensitivity and reduces the optimal enzyme layer thickness. The comparison with representative experimental data suggest that improvements to sensor design described here have brought performance near the theoretical sensitivity limit of ~375 nA μM^{-1} cm^{-2} for this sensor construction at f_{glutox} = 0.2. As suggested by the simulations shown in Fig. 3.12, even higher sensitivities of ~450 nA μM^{-1} cm^{-2} at f_{glutox} = 0.4 and ~550 nA μM^{-1} cm^{-2} at f_{glutox} = 1.0 (data not shown) are possible if stable enzyme layers can be created at these concentrations and all activity is

retained upon immobilization. Theoretically, sensitivities well above 1000 nA μM^{-1} cm^{-2} are possible, although such results would require additional hypothetical improvements including better transport properties of the immobilized enzyme layer, essentially no mass transfer resistance of the permselective films, and improved H_2O_2 electrooxidation kinetics.

Experimental results are consistent with simulated results in terms of optimal enzyme layer thickness and sensitivity for simulated values of f_{glutox} in the range of "0.02 to <0.2, given measured thicknesses and transport properties of microelectrode coatings. The observation that most experimental results correspond to simulations at lower f_{glutox} values than the experimental preparation of 0.2 suggests that enzyme activity was reduced substantially upon immobilization. It is suspected that amine crosslinking negatively impacts immobilized enzyme activity both through direct inactivation of the active site and steric hindrance e!ects, so that actual active f_{glutox} after crosslinking is less than the f_{glutox} used to prepare the sensor.

Response time predictions showed little dependence on f_{glutox}, and fell within the range of ~8–10 ms for sensors with optimal enzyme layer thicknesses (1–2 μm). The discrepancy between experimental and simulated response time may be due to key differences in the experimental and model sensors. In particular, the model assumes a perfectly planar, rigid sensor surface, whereas SEM images show that the surface is rough and probably soft. Thus, external mass transport from the bulk liquid in vitro to the sensor surface likely is impacted. Also, the model does not account for the likely possibility that Glut adsorbs to sites in the immobilized enzyme layer and that there likely are dead-end pores as well. Both of these possibilities could contribute to the longer response times observed experimentally but would not necessarily affect sensitivity. In any case, the value of these response times measured in vitro where an effort is made to reduce the impact of external mass transfer on the measurement is clear in comparing sensors, but the relevance to utility in practice is not so straightforward since the surrounding medium is essentially quiescent in the brain. The true

value of these improved sensors may best be assessed from performance *in vivo*. Recently, data was reported showing excellent recording of ms-scale Glut signals *in vivo* using an innovative Glut biosensor with a thin GlutOx layer.[43] Although the response time and sensitivity were not measured *in vitro*, these results offer promising evidence of the utility of high performance Glut biosensors as neuroscience research tools going forward.

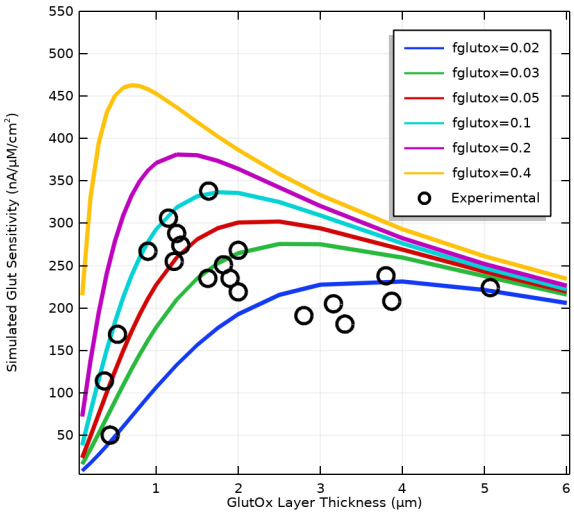

Figure 3.12. Simulations of sensor sensitivity to Glut as a function of GlutOx mass fraction in the enzyme layer (f_{glutox}) and enzyme layer thickness.

3.4 Conclusions

Guided by a detailed mathematical model of electroenzymatic Glut sensors based on crosslinked GlutOx immobilized on planar Pt microelectrodes coated with permselective polymer films, a ~6-fold improvement in sensitivity from ~50 to ~320 nA μM^{-1} cm^{-2} and a ~10-fold improvement in response time from ~0.8 s to ~80 ms was achieved while maintaining a low detection limit of ~0.70 μM and excellent selectivity against AA and DA. The transport properties of the enzyme layer and polymer films used to construct the biosensors were measured directly so as to improve the predictive capability of the mathematical model. Subsequent model simulations showed that the experimentally attained biosensor performance approaches the

theoretical limits of sensitivity (~550 nA μM^{-1} cm^{-2}) and response time ("8–10 ms) achievable with electroenzymatic Glut sensors of this construction using this enzyme. Such high-performance biosensors will enable monitoring of Glut signaling with near cellular-scale spatial resolution and at a temporal resolution closer to that of electrical recordings, particularly local field potentials.[4]

3.5 References

1. A. M. Andrews, ACS Chem. Neurosci., 2013, 4, 645–645.
2. C. Sekirnjak, P. Hottowy, A. Sher, W. Dabrowski, A. M. Litke and E. J. Chichilnisky, J. Neurosci., 2008, 28, 4446–4456.
3. B. Eversmann, M. Jenkner, F. Hofmann, C. Paulus, R. Brederlow, B. Holzapfl, P. Fromherz, M. Merz, M. Brenner, M. Schreiter, R. Gabl, K. Plehnert, M. Steinhauser, G. Eckstein, D. Schmitt-Landsiedel and R. Thewes, IEEE J. Solid-State Circuits, 2003, 38, 2306–2317.
4. G. S. Hong and C. M. Lieber, Nat. Rev. Neurosci., 2019, 20, 330–345.
5. I. L. Jones, P. Livi, M. K. Lewandowska, M. Fiscella, B. Roscic and A. Hierlemann, Anal. Bioanal. Chem., 2011, 399, 2313–2329.
6. Q.J.Liu,W.W.Ye,L.D.Xiao,L.P.Du,N.HuandP.Wang, Biosens. Bioelectron., 2010, 25, 2212–2217.
7. E. H. Kim, G. Chin, G. Rong, K. E. Poskanzer and H. A. Clark, Acc. Chem. Res., 2018, 51, 1023–1032.
8. J. J. Burmeister, F. Pomerleau, P. Huettl, C. R. Gash, C. E. Wemer, J. P. Bruno and G. A. Gerhardt, Biosens. Bioelectron., 2008, 23, 1382–1389.
9. L. N. Q. Hoa, H.-R. Chen and T. T. C. Tseng, Electroanalysis, 2018, 30, 561–570.
10. E. Walker, J. Wang, N. Hamdi, H. G. Monbouquette and N. T. Maidment, Analyst, 2007, 132, 1107–1111.

11. K. M. Wassum, V. M. Tolosa, J. Wang, E. Walker, H. G. Monbouquette and N. T. Maidment, Sensors, 2008, 8, 5023–5036.
12. M. Parkin, S. Hopwood, D. A. Jones, P. Hashemi, H. Landolt, M. Fabricius, M. Lauritzen, M. G. Boutelle and A. J. Strong, J. Cereb. Blood Flow Metab., 2005, 25, 402–413.
13. M. L. Rogers, D. Feuerstein, C. L. Leong, M. Takagaki, X. Niu, R. Graf and M. G. Boutelle, ACS Chem. Neurosci., 2013, 4, 799–807.
14. A. L. Collins, T. J. Aitken, I. W. Huang, C. Shieh, V. Y. Greenfield, H. G. Monbouquette, S. B. Ostlund and K. M. Wassum, Biol. Psychiatry, 2019, 86, 388–396.
15. M. Malvaez, V. Y. Greenfield, A. S. Wang, A. M. Yorita, L. L. Feng, K. E. Linker, H. G. Monbouquette and K. M. Wassum, Sci. Rep., 2015, 5, 12511.
16. E. C. Rutherford, F. Pomerleau, P. Huettl, I. Stromberg and G. A. Gerhardt, J. Neurochem., 2007, 102, 712–722.
17. C. Debiemme-Chouvy, Biosens. Bioelectron., 2010, 25, 2454– 2457.
18. N. Hamdi, J. J. Wang and H. G. Monbouquette, J. Electroanal. Chem., 2005, 581, 258–264.
19. N. Wahono, S. Qin, P. Oomen, T. I. Cremers, M. G. de Vries and B. H. Westerink, Biosens. Bioelectron., 2012, 33, 260– 266.
20. J. J. Burmeister, F. Pomerleau, M. Palmer, B. K. Day, P. Huettl and G. A. Gerhardt, J. Neurosci. Methods, 2002, 119, 163–171.
21. J. J. Burmeister, F. Pomerleau, J. E. Quintero, P. Huettl, Y. Ai, J. Jakobsson, M. Lundblad, A. Heuer, J. T. Slevin and G. A. Gerhardt, Neuromethods, 2018, 130, 327–351.
22. T. T. C. Tseng and H. G. Monbouquette, J. Electroanal. Chem., 2012, 682, 141–146.
23. M. Clay and H. G. Monbouquette, ACS Chem. Neurosci., 2018, 9, 241–251.
24. K. T. Kawagoe, P. A. Garris, D. J. Wiedemann and R. M. Wightman, Neuroscience, 1992, 51, 55–64.

25. J. A. Stamford, Z. L. Kruk and J. Millar, Brain Res., 1984, 299, 289–295.

26. B. Ghasemzedah, J. Cammack and R. N. Adams, Brain Res., 1991, 547, 162–166.

27. B. Ilic, P. Neuzil, T. Stanczyk, D. Czaplewski and G. J. Maclay, Electrochem. Solid-State Lett., 1999, 2, 86–87.

28. S. Vengatesan, E. Cho, H.-J. Kim and T.-H. Lim, Korean J. Chem. Eng., 2009, 26, 679–684.

29. E. Leppänen, A. Peltonen, J. Seitsonen, J. Koskinen and T. Laurila, J. Electroanal. Chem., 2019, 843, 12–21.

30. D. A. Gough and J. K. Leypoldt, Anal. Chem., 1979, 51, 439–444.

31. D. R. Lawson, L. D. Whiteley, C. R. Martin, M. N. Szentirmay and J. I. Song, J. Electrochem. Soc., 1988, 135, 2247–2253.

32. J. A. Leddy, A. J. Bard, J. T. Maloy and J. M. Saveant, J. Electroanal. Chem. Interfacial Electrochem., 1985, 187, 205-227.

33. C. Malitesta, F. Palmisano, L. Torsi and P. G. Zambonin, Anal. Chem., 1990, 62, 2735–2740.

34. L. D. Spurlock, A. Jaramillo, A. Praserthdam, J. Lewis and A. Brajter-Toth, Anal. Chim. Acta, 1996, 336, 37–46.

35. A. J. Bard and L. R. Faulkner, Electrochemical methods : funda- mentals and applications, Wiley, New York, 2nd edn, 2001.

36. A. T. Haug and R. E. White, J. Electrochem. Soc., 2000, 147, 980–983.

37. Z. Ogumi, Z. Takehara and S. Yoshizawa, J. Electrochem. Soc., 1984, 131, 769–773.

38. S. B. Hall, E. A. Khudaish and A. L. Hart, Electrochim. Acta, 1997, 43, 579–588.

39. S. A. M. Vanstroebiezen, F. M. Everaerts, L. J. J. Janssen and R. A. Tacken, Anal. Chim. Acta, 1993, 273, 553–560.

40. M. R. Ryan, J. P. Lowry and R. D. O'Neill, Analyst, 1997, 122, 1419–1424.

41. K. McAteer and R. D. O'Neill, *Analyst*, 1996, 121, 773-777.

42. K. N. Hascup, E. C. Rutherford, J. E. Quintero, B. K. Day, J. R. Nickell, F. Pomerleau, P. Huettl, J. J. Burmeister and G. A. Gerhardt, in Electrochemical Methods for Neuroscience, ed. A. Michael and L. Borland, CRC Press, Boca Raton, 2007, ch. 19, pp. 407–450.

43. Y. Wang, D. Mishra, J. Bergman, J. D. Keighron, K. P. Skibicka and A.-S. Cans, ACS Chem. Neurosci., 2019, 10, 1744–1752.

Chapter 4. Electroenzymatic glutamate sensors are slowed by reversible binding to pore walls of requisite sensor coatings

This chapter presents a proposal for experimental work to address the discrepancy between the simulated Glut sensor response time and the experimentally observed, order-of-magnitude slower response times, with the support of simulation data from new mathematical models. Simulations show that if previous models of electroenzymatic Glut sensors are modified to account for noncatalytic, reversible binding of Glut to the proteins within the sensor's enzyme coating (*i.e.*, glutamate oxidase (GlutOx) and bovine serum albumin (BSA)), the simulated sensor response time increases without affecting the sensor's sensitivity. With reasonable parameter estimates, the new model can fully resolve the prior discrepancy in sensor response time, although experimental evidence is needed to validate these simulations. It is hypothesized that sensors may operate with slower response times during calibrations *in vitro* than during studies *in vivo* due to these reversible binding effects since many of the adsorption sites may already be filled by other biomolecules which are naturally present within the complex extracellular fluid of the brain (and not typically included in solutions for calibrations *in vitro*). Confirmation of this phenomenon and its significance will improve our understanding of sensor response time, which is necessary for the proper analysis of data collected from measurements of transient Glut release events in the brain. It would also be useful for modeling diffusion near and within similar biological structures including misfolded protein aggregates, which are characteristic properties of a number of neurodegenerative diseases including Alzheimer's disease, Parkinson's disease, Huntington's disease, and Amyotrophic lateral sclerosis (ALS).[1]

4.1. Motivation

The important role of glutamate (Glut) as the most common excitatory neurotransmitter in the brain has led to great interest in understanding the biological mechanisms which dictate its release and subsequent signaling as well as its importance in relation to larger scale systems, including those responsible for addictive behavior and neurological diseases. Electrochemical sensors built onto microelectrode array probes have frequently been used to measure such Glut signaling and dynamics in the extracellular space of brain slices, anesthetized animals, and freely behaving animals. Two of the most important properties of these sensors are sensitivities, which relate sensor response to exogenous Glut concentrations, and response time, which is the time required for a sensor to reach a steady-state response (often defined as reaching 90% of the steady-state response) to a step change in Glut concentration. Recently optimized electroenzymatic Glut sensors exhibit great improvements in both of these properties, reaching sensitivities of 320 nA/μM/cm^2 and response times of ~80 ms, aided by mathematical simulations to guide sensor design.[2] However, simulated response times (8 ms) were an order of magnitude faster than those observed experimentally. Identification of the causes of this discrepancy will lead to improved models better able to guide further sensor optimization toward the theoretical limit of sensor response time of ~8 ms, at optimal sensitivity as well.

4.2 Models and simulations

4.2.1 Equations and numerical methods

Mathematical models have been used to simulate Glut biosensor performance by mathematically describing diffusion and reaction of the three chemical species of interest in Glut sensor performance: Glut, O_2 and H_2O_2.[2, 3] These processes are specified in separate time-dependent mass balance equations for each chemical species over every layer of the biosensor (3 separately defined domains, *j,* of 3 linked partial differential equations, *i*) of the following form:

$$\varepsilon_j \frac{\partial C_i}{\partial t} = -\alpha_j D_i \frac{\partial^2 C_i}{\partial x^2} + r_{i,j} \quad (4.1)$$

i = Glut, H_2O_2, O_2; j = PPD, Nafion, immobilized enzyme

In these models, effective diffusivities within sensor coatings are given by $\alpha_j D_i$, where D_i is the molecular diffusivity of species *i* in water and α_j is a constant that adjusts for the porosity of the biosensor layer, *j*, and the tortuosity of the diffusion path within it. The concentration of species *i* within the pore space of each layer is C_i and any reactions it participates in is given by $r_i(C_i)$. Describing diffusion this way (using Fick's Law of diffusion) makes a number of assumptions about the chemical species and the porous sensor coatings, including the assumptions that concentrations remain dilute, that their diffusion is not affected by interactions with the walls of the porous region, and that reaction and diffusion rates are constant throughout the coatings (the porous sensor coatings are homogeneous). The accuracy of any results of simulations that are based on these assumptions are dependent on their validity in the system being described. In the case of Glut diffusing through the immobilized enzyme layer, it is hypothesized that the negatively charged Glut interacts significantly with charged amino acid residues (of BSA and glutamate oxidase) that form the pore walls in the enzyme layer, requiring a modification of Equation 4.1 to describe this effect.

Incorporation of Glut binding to proteins within the sensor's immobilized enzyme layer required the definition of another variable ($C_{glut,ads}$), with an effective diffusivity of 0, representing the concentration of adsorbed Glut that is unable to diffuse or react with GlutOx. The rate of Glut binding and unbinding is described by Equation 4.2, where the binding rate constant is K_{on} = 10^6 M^{-1} s^{-1},[4, 5] the total concentration of proteins in the layer (BSA and glutamate oxidase) is $C_{protein}$, equal to approximately 0.14 M,[3] the number of exposed amino acids that bind with Glut per protein (assuming one Glut molecule per site) is *aaratio*, which is an unknown parameter that was varied from 5 to 20 in the simulations, and the rate of desorption is given by K_{off} as defined

by Equation 4.4. Binding was assumed to follow a Langmuir binding isotherm (Equations 4.3, 4.4), where θ is the fraction of filled binding sites and ΔG is the change in fee energy for Glut binding. Binding energies are also uncertain due to the complexity of the protein surfaces and were varied up to the highest binding energies that have been reported for the binding energy of Glut to some amino acid residues (10,[6] 15-30,[6] and 18 kJ/mol[7] for Glut to binding to Glut, lysine, and arginine, respectively). This model assumes equal binding energies to all sites, although more complex binding can also be simulated;[4] this simplification means the values for binding energies and number of binding sites in this model should be considered *effective* values since the actual binding parameters vary depending on multiple factors including amino acid identity, protein folding, and nearby ions and molecules in solution.

$$r_{glut,ads} = K_{on}C_{glut}\left(aaratio \times C_{protein} - C_{glut,ads}\right) - K_{off}C_{glut,ads} \tag{4.2}$$

$$\theta = \frac{C_{glut,ads}}{aaratio \times C_{protein}} = \frac{K_{eq}C_{Glut}}{1+K_{eq}C_{Glut}} \tag{4.3}$$

$$\Delta G = -RTln\left(\frac{K_{on}}{K_{off}}\right) \tag{4.4}$$

Boundary conditions specify equal fluxes and partition-coefficient dependance on concentrations (or equal concentrations, when appropriate) at internal boundaries, maintaining a conservation of mass and a partitioning of negatively charged Glut from the negatively charged Nafion layer. A mass transfer coefficient describes the flux condition at the sensor surface (m_h = 0.05 cm/s for H_2O_2, with relations for the coefficients of other species based on their molecular diffusivities as described in Chapter 1)[8] representing rapid convective mass transfer in a well-stirred beaker. Kinetics for the electrooxidation of H_2O_2 on platinum define the flux at the electrode surface.[9] Initial concentrations of 0 μM for Glut and H_2O_2 species and a bulk O_2

concentration everywhere of 200 μM are used to represent a step-change in the bulk Glut concentration from 0 to 10 μM; the change to 10 μM is incorporated using the convective mass transfer flux for $t > 0$. Numerical, time-dependent solutions were generated using COMSOL Multiphysics (COMSOL Inc., Los Angeles), as explained previously in Chapters 2 and 3 (other sensor variables including coating thicknesses were kept constant).[2] Further details regarding the use of COMSOL to numerically solve the sets of equations are provided in Appendix A.

4.2.2 Simulations of sensor response time

Initial simulations of Glut sensor response time with the incorporated Glut binding show that simulated sensor response time is strongly dependent on the binding energy (ΔG) and concentration of binding sites, as defined by Equations 4.3 and 4.4. Simulations show that response time (the time to achieve 90% of the steady-state response) increases to the experimental value of ~0.08 s when a binding energy of -18.28 kJ/mol and a binding site concentration corresponding to 10 binding sites per protein are used (*aaratio* = 10). The parameter, K_{on}, was seen to have no effect on response time if $K_{on} > 10^5$ $m^{-1}s^{-1}$, and does not need to be considered further since binding rate constants are generally greater than this value.[4, 5] Overall, precise information regarding the binding energies, distribution of binding energies, and number of binding sites is needed to make definitive conclusions. In the meantime, the model can be used to represent a Glut sensor with the same sensitivity and varied response times, depending on the binding parameters specified.

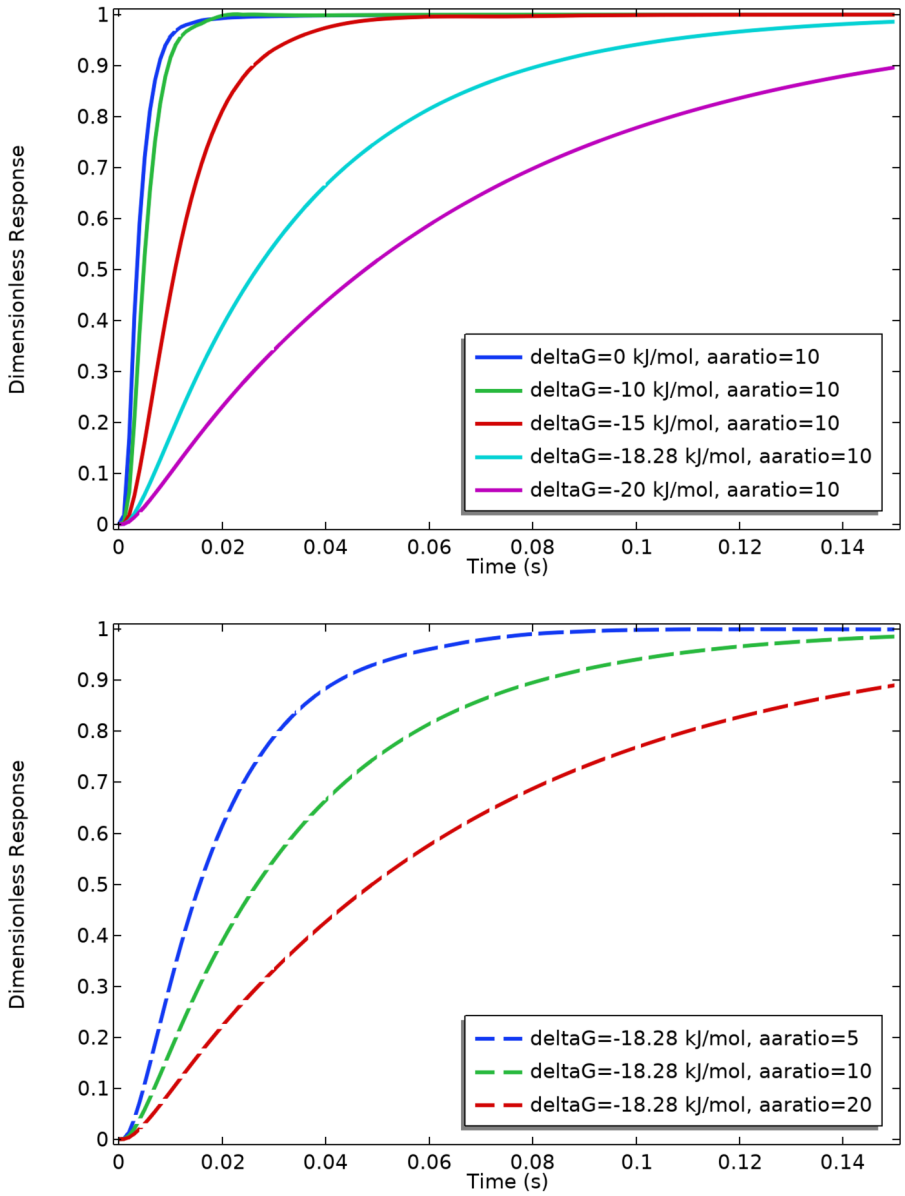

Fig. 4.1. Sensor response relative to maximum sensor response for varied binding energies (ΔG), above, and for varied number of binding sites per protein in the enzyme layer (aaratio). Response time is defined as the time to achieve 90% of the steady-state response, or a dimensionless response of 0.9. Sensor parameters, including coating thicknesses, are consistent with previously reported values.[2]

Additional simulations (not shown) have verified that in the presence of a large concentration of molecules with similar binding affinities and diffusivities, such as ascorbate (ascorbate concentrations in dog cerebrospinal fluid have been measured at ~800 μM),[10] can

improve sensor response to ~8 ms (the theoretically fastest response time at optimum sensitivity). In this case, competitive binding at the protein surfaces is marginalizing the effect of adsorption on response time. If this can be experimentally verified, it may be possible to introduce a sensor pre-treatment method to fill these possible binding sites before sensor use and potentially bring observed sensor response times down to 8 ms.

4.3 Determining effective binding energy and number of effective binding sites

Simulations of glutamate sensors have suggested that glutamate binds to proteins in the enzyme layer, increasing sensor response time if the magnitude of the binding energy is >15 kJ/mol and there are around 5-20 binding sites per protein. To confirm this, it is necessary to measure both the binding energy and number of binding sites per protein. Since the enzyme layer is a mixture of bovine serum albumin (BSA) and a smaller fraction of glutamate oxidase (GlutOx), it would be ideal to measure the amount of Glut that is adsorbed into a similar mixture. However, the high cost of GlutOx makes this an expensive process; instead of the expensive mixture, binding to BSA could be measured instead. Although the amino acid content and sequences are different between proteins, similar residues are present in both proteins and results are expected to be similar for both mixtures and pure BSA.

To measure the BSA binding energy, a solution can be mixed with a relatively large amount of BSA (so that the Langmuir adsorption model is valid), allowed to equilibrate, and then filtered using centrifugal filters (BSA has a molecular weight of 66500 Da) or other methods. Any change in Glut (which can be measured with electroenzymatic Glut sensors) corresponds to Glut binding to the BSA. If this is repeated for increasing initial Glut concentrations, the concentration difference will approach 0 as all or most of the BSA's binding sites become filled. This corresponds to θ approaching 1 (Fig 4.2). By plotting this concentration change as a function of the equilibrated, leftover Glut solution, we should see curves similar to those in Fig. 4.2 where the shape of the curve is a function of the binding energy. By fitting experimental data

to these curves, we can identify an effective binding energy for Glut to BSA. For example, calculations show that binding energies of -15, -18, and -21 kJ/mol should result in half-filling of sites for final solution concentrations of 3, 1, and 0.25 mM and fully filled binding sites for final solution concentrations of ~20, ~10, or ~4 mM, respectively.

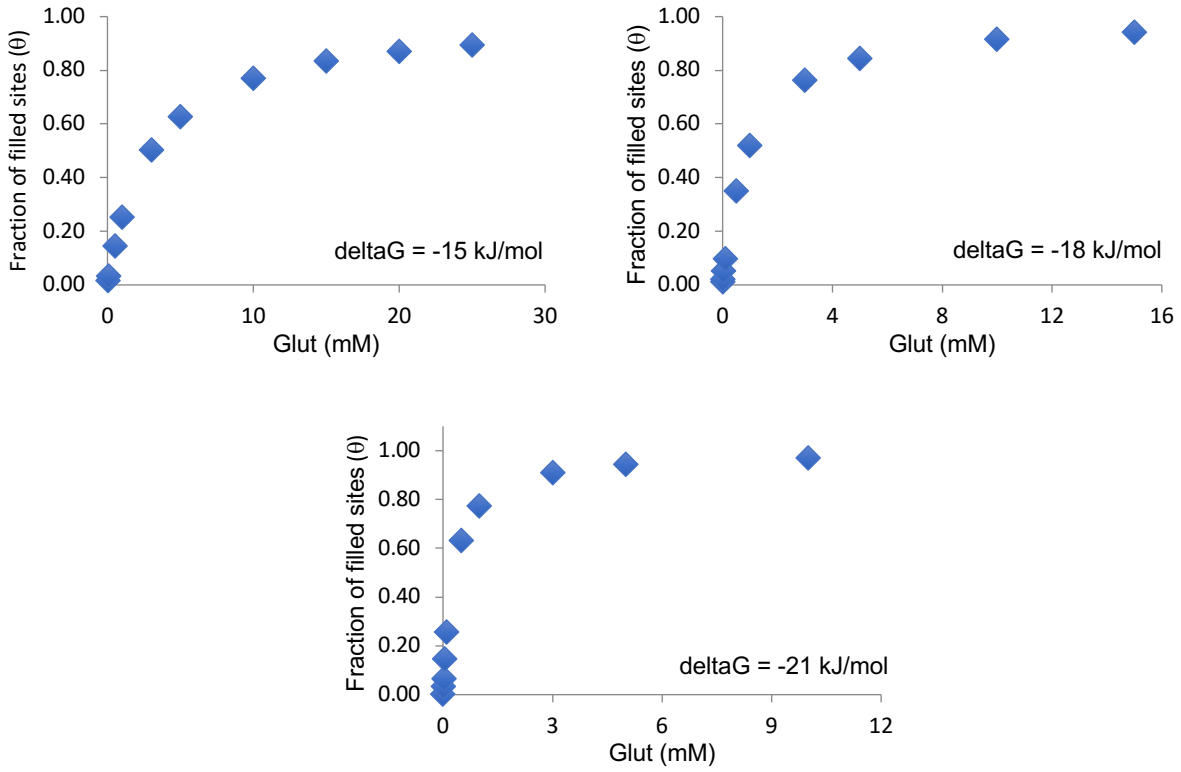

Figure 4.2 Langmuir binding isotherms for binding energies of -15, -18, and -21 kJ/mol. Glut concentration (x-axis) is in equilibrium with BSA.

If the amounts (moles) of BSA and Glut are known, the effective number of binding sites per BSA can also be calculated. This requires measuring the change in Glut concentrations in solution before and after mixing with BSA, conversion to moles transferred using the original solution volume and a mass balance, and calculating the moles of Glut per mol BSA based on the initially measured amount of BSA and fraction of filled adsorption sites.

4.4 Additional Considerations

It will be wise to test the assumption that the presence of other amino acids or sugars would compete for these binding sites and could make response time faster *in vivo*. It is possible that these molecules compete for the theorized binding sites; if this is true, sensors may not be inhibited by adsorption effects *in vivo* to the same degree as *in vitro*. To test this hypothesis, the experiment would be repeated after first adding physiologically relevant amounts of ascorbate, dopamine, sugars, or other amino acids that are naturally present in the brain extracellular space to the Glut or BSA component. Differences between the results of these experiments and the initial results would inform us of the significance of competitive binding in determining sensor response time. An additional test of the sensor response time after submerging it in a similar complex mixture may further confirm that the presence of competitive binding could decrease response time. This practical confirmation of our hypothesis concerning reversible binding in the sensor coating would provide a satisfying conclusion to the set of simulations, experiments, and calculations conducted.

4.5 References

1. Lim, J.; Yue, Z., Neuronal aggregates: formation, clearance, and spreading. *Dev Cell* **2015,** *32* (4), 491-501.
2. Huang, I. W.; Clay, M.; Wang, S.; Guo, Y.; Nie, J.; Monbouquette, H. G., Electroenzymatic glutamate sensing at near the theoretical performance limit. *Analyst* **2020,** *145* (7), 2602-2611.
3. Clay, M.; Monbouquette, H. G., A Detailed Model of Electroenzymatic Glutamate Biosensors To Aid in Sensor Optimization and in Applications in Vivo. *ACS Chem Neurosci* **2018,** *9* (2), 241-251.

4. Svitel, J.; Balbo, A.; Mariuzza, R. A.; Gonzales, N. R.; Schuck, P., Combined affinity and rate constant distributions of ligand populations from experimental surface binding kinetics and equilibria. *Biophys J* **2003,** *84* (6), 4062-77.

5. Nair, H. K.; Seravalli, J.; Arbuckle, T.; Quinn, D. M., Molecular recognition in acetylcholinesterase catalysis: free-energy correlations for substrate turnover and inhibition by trifluoro ketone transition-state analogs. *Biochemistry* **1994,** *33* (28), 8566-76.

6. Mukherjee, A.; Bhimalapuram, P.; Bagchi, B., Orientation-dependent potential of mean force for protein folding. *J Chem Phys* **2005,** *123* (1), 014901.

7. Jaeqx, S.; Oomens, J.; Rijs, A. M., Gas-phase salt bridge interactions between glutamic acid and arginine. *Phys Chem Chem Phys* **2013,** *15* (38), 16341-16352.

8. Bird, R. B.; Stewart, W. E.; Lightfoot, E. N., *Transport phenomena*. 2nd, Wiley international ed.; J. Wiley: New York, 2002; p xii, 895 p.

9. Hall, S., Khudaish, EA, Hart, AL, Electrochemical oxidation of hydrogen peroxide electrodes. Part 1. An adsorption-controlled mechanism. *Electrochim. Acta* **1998,** *43*, 579-588.

10. Bito, L.; Davson, H.; Levin, E.; Murray, M.; Snider, N., Concentrations of Free Amino Acids and Other Electrolytes in Cerebrospinal Fluid in Vivo Dialysate of Brain and Blood Plasma of Dog. *J Neurochem* **1966,** *13* (11), 1057-&.

Chapter 5: Electroenzymatic choline sensing at near the theoretical performance limit

Chapter 5 is reproduced with permission from:

Huang, I. W.;* **Clay, M.**;* Cao, Y.; Nie, J.; Guo, Y.; Monbouquette, H. G., Electroenzymatic choline sensing at near the theoretical performance limit. *Analyst* **2021,** *146* (3), 1040-1047.

*These authors contributed equally to this work

Mackenzie Clay developed the mathematical model and performed the simulations and also made large contributions to the writing and data analysis.

Abstract

A high performance, electroenzymatic microsensor for choline based on choline oxidase (ChOx) immobilized on Pt coated with permselective polymer layers has been created that exhibits sensitivity approaching the theoretical performance limit. Sensor construction was guided by simulations performed with a detailed mathematical model. Implantable microsensors with an array of electroenzymatic sensing sites provide a means to record concentration changes of choline, an effective surrogate for acetylcholine due to its very rapid turnover in the brain, and other neurochemicals in vivo. However, electroenzymatic sensors generally have insufficient sensitivity and response time to monitor neurotransmitter signaling on the millisecond timescale with cellular-level spatial resolution. Model simulations suggested that choline sensor performance can be improved significantly by optimizing immobilized ChOx layer thickness and minimizing the thicknesses of permselective polymer coatings as well. Electroenzymatic choline sensors constructed with a ~5 μm-thick crosslinked ChOx layer atop

200 nm-thick permselective films (poly(m- phenylenediamine) and Nafion) exhibited unprecedented sensitivity and response time of 660 ± 40 nA μM^{-1} cm^{-2} at 37 °C and 0.36 ± 0.05 s, respectively, while maintaining excellent selectivity. Such performance characteristics provide greater flexibility in the design of microelectrode array (MEA) probes with near cellular-scale sensing sites arranged in more dense arrays. Also, faster response times enable better resolution of transient acetylcholine signals and better correlation of these events with electrophysiological recordings so as to advance study of brain function.

5.1 Introduction

A deep understanding of information processing in the brain is critical for rational development of effective treatments for complex neurological disorders including drug addiction. Brain processes are controlled by neuronal networks whose functioning is evidenced both by neurochemical signaling and electrophysiological events. Thus, there is great incentive to develop advanced technologies for neurochemical and electrophysiological recordings with similar spatiotemporal resolution *in vivo* so that this data may be correlated and used to unravel network functions. Current implantable devices enable electrophysiological recordings simultaneously from large numbers of interconnected neurons at millisecond temporal and cellular-scale spatial resolution.[1–5] However, techniques for neurochemical recording have yet to achieve such high spatiotemporal resolution due to slow sensor kinetics exacerbated by the need for selectivity against the complex background of brain extracellular fluid.[6–14] Historically, broadly applicable neurotransmitter detection *in vivo* has been accomplished using microdialysis probes coupled to analytical instrumentation (*e.g.*, high performance liquid chromatography (HPLC)). However, the typical minute-to-minute temporal resolution and relatively large size of the probes has limited utility of this technique, although there have been recent impressive advances both in probe size and sampling rate.[15,16]

Micromachined microprobes supporting an array of microelectrode sensing sites have emerged as alternative tools to monitor concentration changes for a limited number of neurochemicals. These microsensors, once implanted in the brain, are in direct contact with extracellular fluid, potentially providing a means for near-real time neurochemical sensing.[17–21] Sites on these microelectrode array (MEA) microprobes may be modified with permselective polymer films and immobilized redox enzymes to create selective electroenzymatic sensors. For example, the electroenzymatic choline (Ch) sensor studied in this work consists of a platinum (Pt) microelectrode coated first with permselective polyphenylenediamine (PPD) and Nafion films and then a layer of cross-linked choline oxidase (ChOx). ChOx catalyzes the 4-electron oxidation of Ch to glycine betaine in the presence of oxygen to give two equivalents of hydrogen peroxide (H_2O_2), which diffuse through the underlying polymer layers to the electrode surface where they are electrooxidized thereby generating a current signal indicating the presence of Ch.

$$\text{Ch} + O_2 \xrightarrow{\text{ChOx}} \text{betaine aldehyde} + H_2O_2 \tag{5.1}$$

$$\text{betaine aldehyde} + O_2 + H_2O \xrightarrow{\text{ChOx}} \text{glycine betaine} + H_2O_2 \tag{5.2}$$

Electrooxidizable interfering species existing in brain extracellular fluid such as dopamine (DA) and ascorbic acid (AA), which are larger than H_2O_2 and charged, are blocked from the electrode surface by the PPD and negatively charged Nafion films through a combination of size exclusion and charge repulsion mechanisms. The high specificity of ChOx for Ch provides selectivity against non-electroactive species other than Ch.[22]

Choline is a useful surrogate for the important neurotransmitter, acetylcholine (ACh), which is turned over very rapidly to Ch and acetate in the brain.[23] Our group and others have demonstrated successfully the feasibility of such electroenzymatic Ch sensors with response

times in the ~1 s range for the detection of Ch both *in vitro* and *in vivo*.[14,19,21,24] An alternative approach to achieve selective detection of Ach directly is to co-immobilize acetylcholinesterase and ChOx on an electrode and to employ fast-scan cyclic voltammetry (FSCV) rather than constant potential amperometry. However, a FSCV sampling rate of 10 Hz (100 ms sampling interval) leads to an effective response time of ~1 s as well (sampling at 10 Hz cannot resolve ~100 ms events).[25,26] Such 1 s temporal response times still are not fast enough to detect rapid neurotransmitter signaling events that are thought to occur on the millisecond time scale. Furthermore, the previously published sensitivities are too low to create small microsensors with cellular-scale spatial resolution.

To address these challenges of spatiotemporal resolution, a mathematical model has been developed for devices of this type. Our previous glutamate (Glut) sensor modelling and experimental studies showed that performance can be improved dramatically by engineering the compositions and thicknesses of the immobilized enzyme and permselective film compositions.[27,28] To construct an electroenzymatic sensor, the protein catalyst most commonly is immobilized by loading a mixture of enzyme and BSA on the microelectrode surface and crosslinking with glutaraldehyde (GAH).[9,11,14,20,29–31] The resulting enzyme layer thicknesses typically have been in the 10 μm range to ensure adequate signal. Our simulation results suggested that such thick coatings cause elevated mass-transfer resistances leading to long response times.[28] If enzyme activity and accessibility could be preserved well during the immobilization process, the density of active enzyme in the layer could be increased so that layer thicknesses could be reduced with an actual enhancement in sensitivity. The systematic optimization of Glut sensors based on the guidance of our simulations led to a remarkable 6-fold improvement in sensitivity and a 10-fold reduction in response time to 80 ms.[28]

In this work, a model of electroenzymatic Ch sensors was developed and used to guide sensor optimization in the same manner as was done for Glut sensors previously.[28] Simulations of Ch sensors similarly illustrated the importance of depositing enzyme layers with optimal

thicknesses, dependent on the active enzyme concentration, in order to maximize H_2O_2 generation near the electrode surface. Such an approach shortens diffusion times and improves sensor response. Retention of enzyme activity was enhanced by exploring additional enzyme crosslinkers and changes to the enzyme immobilization conditions. The optimized, thinner immobilized ChOx layer resulted in sensors with higher sensitivities approaching theoretical limits, significantly faster response times, low detection limits, and excellent selectivity.

5.2 Experimental

5.2.1 Reagents

Nafion (5 wt% in lower aliphatic alcohols and water, 15-20% water), *m*-phenylenediamine (PD), bovine serum albumin (BSA) lyophilized powder, choline oxidase (ChOx, from *Alcaligenes* sp.), choline chloride (Ch), glutaraldehyde solution (25% in water, GAH), L-ascorbic acid (AA), 3-hydroxytyramine (dopamine, DA), sodium phosphate dibasic, sodium chloride, and hydrogen peroxide solution (30%) were purchased from Sigma-Aldrich (St. Louis, MO). Sulfuric acid (30%), hydrochloric acid (36.5-38%), bis(sulfosuccinimidyl)suberate (BS3), sulfo-(ethylene glycol bis(sulfosuccinimidyl succinate)) (EGS), and (1-ethyl-3-(3-dimethylaminopropyl)carbodiimide hydrochloride) (EDC) were purchased from Thermo Fisher Scientific (Pittsburgh, PA). Ag/AgCl glass-bodied reference electrodes with NaCl electrolyte (3 M) and a 0.5-mm-diameter Pt wire auxiliary electrode were obtained from BASi (West Lafayette, IN). Sodium phosphate buffer (PBS, pH 7.4) was composed of 50 mM sodium phosphate dibasic and 100 mM sodium chloride. Four-inch, 150 μm silicon wafers were purchased from Silicon Valley Microelectronics (Santa Clara, CA).

5.2.2 Instrumentation

Electrochemical preparation and calibration of the microsensors were performed using a Versatile Multichannel Potentiostat (model VMP3) equipped with the ‘p’ low current option and

N'Stat box driven by EC-LAB software (Bio-Logic USA, LLC, Knoxville, TN) in a three-electrode configuration consisting of the sensing electrode, a Pt wire auxiliary electrode, and a Ag/AgCl reference electrode. The film thicknesses on microelectrodes were determined by milling pores on the deposited films using a focused ion beam (FIB) and measuring cross-section thicknesses using a scanning electron microscope (Nova 600 SEM/FIB System).

5.2.3 Sensor preparation

Fig. 5.1 shows a scanning electron micrograph (SEM) and optical microscopy image of the microelectrode array (MEA) tip of a single probe used in this work. The probe shafts were 150 μm thick, 140 μm wide and 9 mm long with four 6000 μm^2 (40 μm x 150 μm) Pt recording sites arranged in pairs at the tip. Microelectrode array probes were manufactured using microelectromechanical system (MEMS) fabrication techniques as described in our previous work.[11] Each microsensor was cleaned with 0.1 M H_2SO_4 solution by cycling the potential between -0.2 V and 1.5 V at a scan rate of 50 mV/s vs. Ag/AgCl, repeated at least 4 times. Afterward, a poly-phenylenediamine (PPD) film was electrodeposited from a 5 mM PD solution in phosphate-buffered saline (0.1 M PBS) by holding the voltage constant at 0.85 V vs. Ag/AgCl until the total transferred charge reached 7.6×10^{-7} coulombs. A Nafion layer then was applied by dip-coating a 2% Nafion solution (diluted from stock with 4:1 IPA:water) once, followed by annealing at 115 °C for 20 min. Next, enzyme immobilization was accomplished by manually swiping ~1 μL of a ChOx and BSA mixture (at different ratios, see below) onto the microelectrode sites using a microliter syringe and exposing the deposit to different crosslinkers, also as described below. Twelve to 15 coatings of enzyme solution typically gives a ~4 μm thick ChOx layer on the electrode surface, depending on solution concentration and environmental conditions.

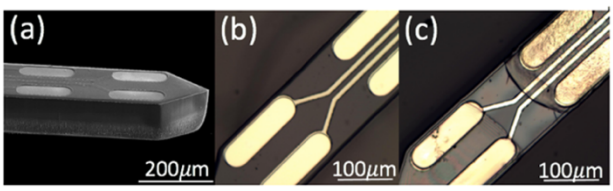

Fig. 5.1 (a) SEM and (b) optical microscopy images of the bare microelectrode array (MEA) probe. (c) Optical microscopy image of the MEA probe after polymer and enzyme deposition.

In this work, four different crosslinkers, including three amine-to-amine crosslinkers with different spacer arm lengths (GAH, BS3, EGS) and one carboxyl-to-amine crosslinker (EDC), were used and compared. Each set of crosslinking conditions was optimized individually before making comparisons (see Supplementary Information). A previously loaded ChOx/BSA mixture was exposed to 5% GAH vapor for 1 min at room temperature or to manually applied ~0.5 µL BS3 (100 mg/ml in PBS) or ~0.5 µL EGS (100 mg/ml in PBS). Alternatively, when EDC was used as crosslinker, EDC was mixed directly with ChOx and BSA to give a final EDC concentration of ~6.3 mg/ml in PBS prior to rapid application onto a microelectrode. After the crosslinking step, sensors were stored dry at 4 °C for 48 h prior to testing.

5.2.4 Electrochemical measurements

To determine the selectivity and sensitivity, a constant potential of 0.7 V vs. Ag/AgCl was applied to the microsensors in rapidly stirred PBS buffer solution at pH 7.4 and ~37 °C. Selectivity was assessed relative to AA and DA, which are electroactive interferents commonly found in brain extracellular fluid (ECF). Their typical concentrations in ECF are in the range of a few hundred µM for AA and from nM to a few µM for DA.[32,33] In selectivity tests, the current signal from a probe immersed in stirred buffer was allowed to stabilize. Subsequently AA and DA were added separately to the beaker to reach final concentrations of 250 µM AA and 10 µM DA. Next, serial injections were made to give final concentrations of 20-100 µM Ch and 20 µM H_2O_2 to determine sensitivities to both species. The response time ($t_{0\text{-}90\%}$) of Ch sensors was

estimated from the current response to a near step change in concentration created by analyte injection into rapidly stirred PBS buffer.

5.2.5 Mathematical model and simulations

Simulations of sensor performance were generated using an adaptation of our established model for electroenzymatic glutamate (Glut) sensors that was modified to include ChOx rather than glutamate oxidase in the immobilized enzyme coating.[28,34] In the model, a set of partial differential equations describe one-dimensional transport as well as consumption or generation rates of Ch, O_2, and H_2O_2 within and between separately modelled PPD, Nafion, and immobilized enzyme domains,

$$\epsilon_j \frac{\partial C_i}{\partial t} = -\alpha_j D_i \frac{\partial^2 C_i}{\partial x^2} + r_{i,j}. \quad (5.3)$$

In each equation for species *i* in coating *j*, C_i is the concentration within the pores of the coating, *t* is time, *x* is the distance from the Pt microelectrode surface, ϵ_j is the void fraction, αD is the effective diffusivity, and *r* is the reaction rate (if enzyme is present). In these equations, each chemical species is allowed to diffuse freely within the void spaces of the coatings in which they are soluble, as defined by the transport parameters that were used in the Glut sensor model, assuming them to be unchanged; the Ch diffusion coefficient at 25 °C has been reported,[35] and the diffusivity at 37 °C (1.816×10^{-9} m^2/s) was calculated according to the Stokes-Einstein equation. It is also assumed that the H2O2 electrooxidation kinetics on the Pt microelectrode sensing sites is also unchanged from that used previously.[36] Enzymatic reaction rates reflect ChOx kinetics for the full oxidation of Ch to glycine betaine, recognizing that the betaine aldehyde intermediate does not leave the enzyme active site,

$$r_{Ch} = -\frac{k_{cat} c_e c_{Ch} c_{O_2}}{k_{m,O_2} c_{Ch} + k_{m,Ch} c_{O_2} + c_{Ch} c_{O_2}} = 2r_{O_2} = -2r_{H_2O_2} \quad (5.4)$$

Since the measured kinetic rates for ChOx isolated from *Alcaligenes sp* are for air-saturated concentrations of O_2 (~206 μM) and do not account for oxygen dependence,[37] which is important to consider in modelling biosensors, O_2 kinetics terms were added and the published, apparent k_{cat} and $k_{m,Ch}$ were multiplied by a factor of $(1 + k_{m,O_2}/C_{O_2})$ to give the k_{cat} and $k_{m,Ch}$ in the rate equation above and to reflect the intrinsic, O_2-dependent rates (k_{m,O_2} was assumed to be 1 mM). The resulting enzymatic rate constants were found to be consistent with values found from ChOx isolated from *A. globiformis* at the temperature and pH used (k_{cat} = 95 s^{-1}; $k_{m,Ch}$ = 5.07 mM; k_{m,O_2} = 1 mM),[38] suggesting that ChOx isolated from either organism may show similar kinetic behavior. The enzyme concentration (mol/L) depends on the fraction of ChOx in the layer and the void fraction, and was calculated in the same way as in the Glut model based on a protein density of 1.41 g/mL: $c_e = [1000 * 1.41 * f_{ChOx} * (1 - \epsilon)]/MW_{ChOx}$, where f_{ChOx} is the mass fraction of protein in the immobilized enzyme layer that is ChOx. Numerical solutions were obtained using COMSOL (COMSOL, Inc. Los Angeles), employing boundary conditions that simulate a step-change in Ch concentration from 0 to 20 μM at the microsensor surface at time, t = 0.

5.3 Results and discussion

5.3.1 Effect of enzyme loading and activity

In an effort to improve enzyme activity retention, the alternative homobifunctional crosslinkers BS3 and EGS (that like GAH also react with amine groups at neutral pH) were studied. We demonstrated earlier that Glut sensors made with enzyme crosslinked with BS3 showed great improvement in sensitivity compared to those crosslinked with GAH, probably due to the longer spacer arm of BS3, 11.4 Å *vs* 5 Å.[28] In this work, in addition to BS3 and GAH, the

crosslinker, EGS, with the longest spacer arm of 16.1 Å was used in order to explore further the effect crosslinker spacer arm length on resulting sensor performance. Before making a comparison among these three reagents, crosslinking conditions were investigated individually by varying crosslinker concentrations and vapor exposure times to find the best conditions for use of the reagent for Ch sensor fabrication (see Supplementary Information). Representative EGS optimization data is illustrated in Fig. 5.2(b), which shows that above ~100 mg/mL EGS, there is no statistically meaningful improvement in sensor sensitivity.

Fig. 5.2 (a) Ch sensitivity comparison between GAH, BS3 and EGS crosslinked Ch sensors with error bars giving 95% confidence intervals. (b) Effect of EGS concentration on the Ch sensitivity. In all cases, the mass ratio of ChOx to BSA was 2 : 3 and the enzyme layer was ~3-4 μm thick.

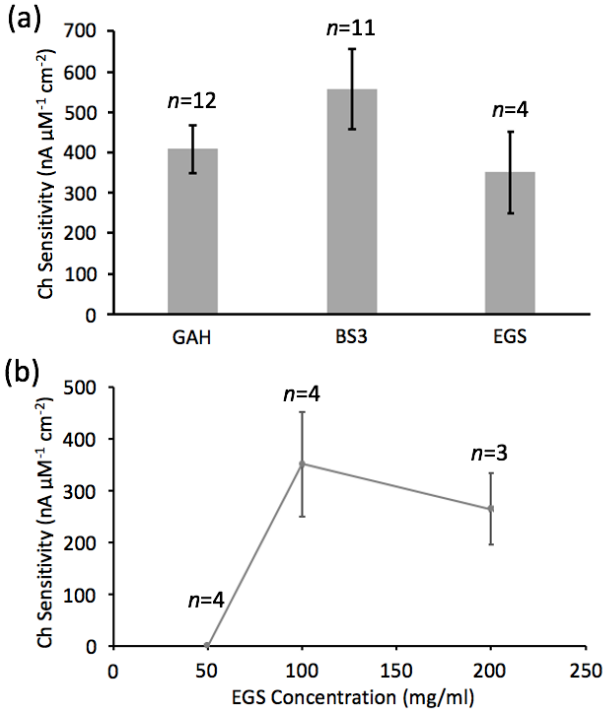

After this optimization process, Ch sensors made with BS3-crosslinked ChOx showed the greatest sensitivity relative to those crosslinked with GAH or EGS, 557 ± 99 nA μM^{-1} cm^{-2} (*n* = 11), 409 ± 59 nA μM^{-1} cm^{-2} (*n* = 12) and 351 ± 101 nA μM^{-1} cm^{-2} (*n* = 4), respectively. This ~1.5-fold improvement in sensitivity of Ch sensors crosslinked with BS3 compared to those crosslinked via GAH agrees with our previous work on Glut sensor optimization.[28] However, it was interesting to observe the decrease in Ch sensitivity when the longest crosslinker, EGS, was used. We hypothesize that spacer arm length not only affects the accessibility of substrate to the enzyme active site, but also the void fraction within the enzyme layer and the concentration of active enzyme entrapped in the BSA/ChOx network. The optimal crosslinker will immobilize ChOx as densely as possible without becoming a barrier to diffusion or restricting any enzyme conformational changes that may occur during catalysis. The moderate length of the BS3 spacer arm may be preferable, because such a length (11.4 Å) is long enough to reduce enzyme crowding and improve active site accessibility, but also short enough to maintain a stable, high enzyme concentration in the crosslinked BSA/ChOx network.

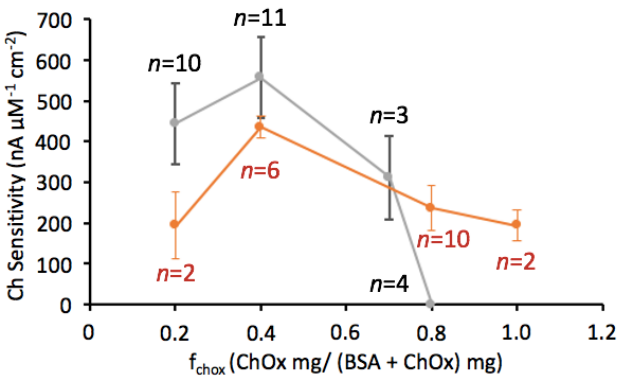

Fig. 5.3 Effect of immobilized ChOx concentration on the Ch sensitivity of sensors crosslinked via BS3 (grey trace) and sensors crosslinked via EDC (orange trace). In all cases, the enzyme layer thickness was ~3-4 μm. Error bars represent 95% confidence intervals.

The effort to improve Ch sensor performance was carried further by conducting a study of the effect of deposited enzyme concentration on sensor performance, which can be

performed straightforwardly by changing the relative proportion of ChOx and BSA without changing enzyme layer thickness of ~3-4 μm. The mass fraction of ChOx (f_{chox}) was varied from 0.2 to 0.8 for the sensors coated with PPD and Nafion and crosslinked with BS3. The experimental Ch sensitivity versus f_{chox} plot showed that Ch sensitivity tends to fall above f_{chox} = ~0.4 and drops to zero at high enzyme concentration corresponding to f_{chox} = 0.8 (Fig. 5.3). It is noteworthy that this general trend also was observed for GAH- and EGS-crosslinked Ch sensors. For the thin enzyme layers explored here, a decrease in Ch sensitivity at low f_{chox} was expected due to insufficient active enzyme available to turnover Ch at the high rate needed for a strong current signal. However, high relative enzyme concentration (low BSA concentration) also was found not to be preferable. This result again matched our previously published data on Glut sensor optimization showing that there are insufficient lysine groups available for crosslinking of the protein layer at low relative concentrations of lysine-rich BSA (Fig. 5.3).

These consistent results prompted us to consider crosslinkers that react with carboxyl groups of which ChOx has an abundance on its surface. The heterobifunctional crosslinker, EDC, which crosslinks carboxyl and amine groups, was chosen due to its ready commercial availability. The mass fraction of ChOx was varied from f_{chox} = 0.2 to f_{chox} = 1.0 and the experimental results are shown as the orange trace in Fig. 3. This amine-to-carboxyl crosslinker enabled the stable immobilization of ChOx in the absence of BSA (f_{chox} = 1.0). This data supports our unsurprising contention that the availability of crosslinkable functional groups on the enzyme surface plays an important role in stable enzyme immobilization at higher concentration. However, a decrease in Ch sensitivity at high enzyme concentration was still observed, which may be due to hindered accessibility of the enzyme active site and/or increased enzyme deactivation as more EDC, which has a very short spacer arm, reacts directly with ChOx instead of BSA. Overall, sensors crosslinked with EDC showed lower Ch sensitivity of 435 $\pm$ 27 nA μM^{-1} cm^{-2} (n = 6) compared to those crosslinked with BS3 at optimal values of

f_{chox}. As a result, the BS3 crosslinked sensor with f_{chox} = 0.4 was chosen for future work due to its best sensitivity.

5.3.2 Optimized enzyme layer thickness

Fig. 5.4 shows Ch sensitivity for varied thicknesses of the enzyme layer, using the optimal f_{chox} of 0.4 and best crosslinker (BS3). As expected, Ch sensitivity decreased sharply for enzyme layer thicknesses less than 3 μm due to insufficient deposited enzyme. Sensitivity reached a plateau as enzyme layer thickness increased beyond ~4 μm. Since response time is known to increase with layer thickness, a ChOx layer thickness of 4-6 μm was determined to be best to ensure both high Ch sensitivity and fast response time. The plateau in sensitivity for enzyme layers more than 3 μm thick may be due to the counterbalancing effects of greater enzyme availability and increasing mass-transfer limitation as the enzyme layer is thickened.

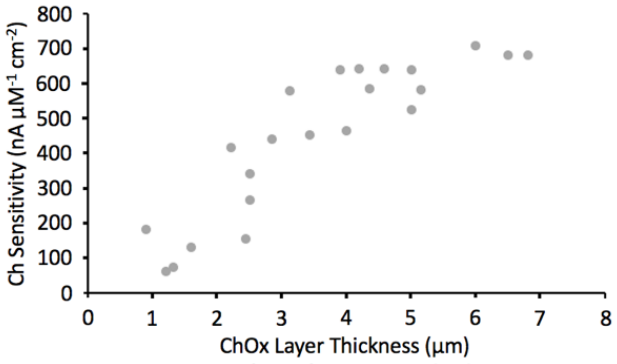

Fig. 5.4. Sensitivity versus immobilized ChOx layer thickness. In all cases, f_{ChOx} = 0.4. All sensors were crosslinked with BS3. Each data point represents one trial.

5.3.3 Optimized sensor performance

The sensitivity of the best Ch sensor constructed was based on the slope of the linear range of calibration curves (0-100 μM Ch), and the detection limit was determined at a signal-to-noise ratio of 3. Ch sensors generated with optimal enzyme layer composition f_{ChOx} = 0.4, crosslinked with BS3, and with enzyme layer thickness in the 4-6 μm range showed high Ch sensitivity of 658 ± 40 nA μM^{-1} cm^{-2} (n = 20), low detection limit of 0.34 ± 0.06 μM (n = 20), and excellent selectivity against two common interferents, AA and DA, tested at physiologically relevant concentrations (Fig. 5.5). This detection limit is suitable for detecting Ch transients in the brain, which have been reported in the range of 0.5-2 μM in response to behavioural cues and up to ~6 μM following KCl injections.[39,40]

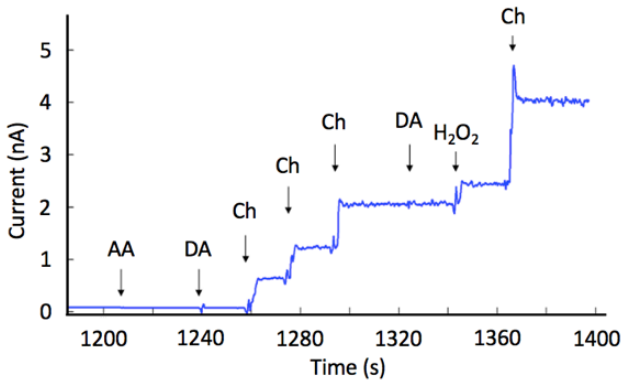

Fig. 5.5 Representative current responses of optimized Ch sensors tested in batch with key interferents AA (250 μM), DA (5 μM), target Ch (final 20, 40, 60 μM in solution), interferent DA (final 15 μM in solution), H_2O_2 (20 μM) and Ch (final 100 μM in solution) in series.

5.3.4 Response time

Response time is defined here as the time for the current signal to reach 90% of its steady-state value in response to a step change in Ch from zero to 60 μM in a stirred beaker. Compared to other sensors in the literature that reported response times of Ch sensors of ~1 s[14,19], our improved sensor with thinner enzyme and permselective layers showed fast response time of 0.36 ± 0.05 s (n = 8) without compromising sensitivity and selectivity (Fig. 5.6). The very

rapid response of bare Pt to 10 μM H_2O_2 is also shown in Fig. 5.6 as a benchmark, which is close to a step as expected. A comparison of the performance of reported Ch sensors illustrates the remarkably improved sensitivity and response time of the sensor reported here (Table 5.1).

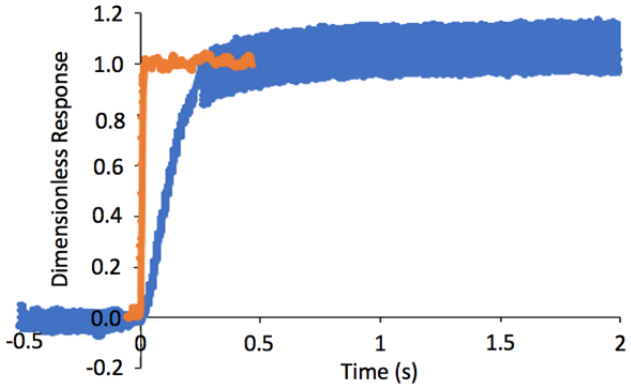

Fig. 5.6 Representative optimized Ch sensor response to a step-change in Ch concentration from 0 to 60 μM (blue trace) and a step-change in H_2O_2 for a bare Pt sensor (orange trace) serving as a benchmark.

5.3.5 Stability

The stability of the Ch sensor *in vitro* was expressed as half-life, the amount of time required for the sensitivity to be reduced to one half of its original value, for sensors stored in PBS at 4 °C and tested periodically at 37 °C. The decay in sensitivity over time, nondimensionalized relative to the initial sensitivity, is shown in Fig. 5.7. Results showed that Ch sensors crosslinked with BS3 (n = 4) had longer half-lives on average than those crosslinked conventionally with GAH (n = 4), which were ~11 days and ~ 8 days, respectively. After 2 weeks, the GAH-crosslinked Ch sensors exhibited less than 10% of initial sensitivity, whereas BS3-crosslinked Ch sensors retained 40% sensitivity over the same time period. The fast decrease in Ch sensitivity after 2 weeks for GAH-crosslinked sensors is likely due to the instability of the immobilized enzyme layer, which was readily observed under the microscope. We hypothesize that the smaller GAH is more likely to form intramolecular bonds that do not contribute as well to a more stable three-dimensional network.[31]

Table 5.1. Comparison of the performance characteristics of the Ch sensor of this work with other recently reported electroenzymatic Ch sensors.

Sensitivity (nA μM^{-1} cm^{-2})	Response time (s)	Limit of detection (μM)	Reference
654	0.35	0.34	This work
354	2	0.45	[41]
286	1.5	1.00	[14]
204	4	0.60	[42]
128	1.16	0.12	[19]
75	2	15.00	[43]

5.3.6 Simulations to determine theoretical performance limits

Simulations of optimized Ch sensors (Fig. 5.8) predict the maximum theoretical sensitivities of sensors with the required permselective films and the enzyme layer thicknesses and compositions that were tested experimentally. The fraction of active ChOx is expected to decrease upon immobilization and over time, prompting simulations to consider how sensitivity is affected when f_{ChOx} drops below 0.4. Experimental data suggest that f_{ChOx} is significantly reduced after immobilization, consistent with simulations and optimizations of Glut sensors.[28] In Ch sensors, experimental maximum sensitivities are consistent with a simulated f_{ChOx} of 0.2. Comparison of experimental performance to theoretical predictions may suggest that sensors perform as though they have a thinner enzyme layer; this could be explained by considering the roughness of the immobilized enzyme layer's surface, which can result in a lower effective thickness.

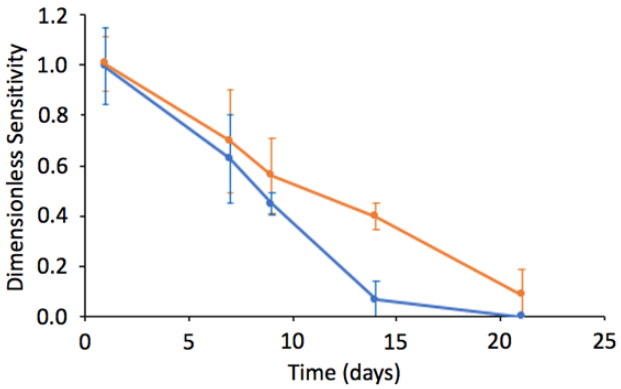

Fig. 5.7 Stability of GAH-crosslinked (blue trace) and BS3-croslinked (orange trace) Ch sensors stored in PBS at 4 °C and tested periodically at 37 °C. Data shown with 95% confident intervals (n = 4 for both cases).

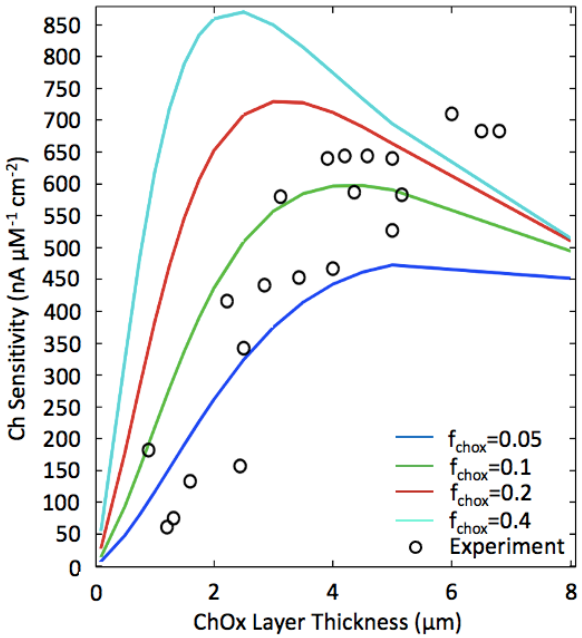

Fig. 5.8 Simulated sensitivity over a range of ChOx layer thicknesses and f_{ChOx} within the layer. Experimental values included for reference.

Simulated response times increased linearly with increasing enzyme layer thicknesses as expected, but simulations also predict that response time could be as fast as 0.048 s for sensors with an enzyme thickness of 5 µm rather than the 0.35 s found experimentally. Model modifications could be made to increase simulated response times without affecting sensitivity by incorporating in the model an accounting of Ch adsorption to protein surfaces. The likelihood

of this type of interaction is supported by experimental data showing reduced response times for later additions of Ch (Fig. 6), when more of the proposed Ch binding sites may already be filled. If this is true, it is likely that *in vivo* response times will approach the theoretical response times, which are significantly faster than those observed *in vitro*, although further work would be required before making definitive conclusions.

Oxygen dependence was investigated by simulating sensor response to varying O_2 and Ch concentrations. The linear range of the sensor was found to be determined linearly by the bulk concentration of O_2 for concentrations of Ch at least as high as 200 μM, where the concentration of O_2 must be >60% of the Ch concentration for >90% of the maximum sensor response or >150% of the Ch concentration for full sensor response. Since the concentration of O_2 in the brain is known to range from ~5 to 50 μM, it is plausible for Ch sensors to begin showing nonlinearity *in vivo* at Ch concentrations in the range of 10 to 100 μM, depending on O_2 availability.

5.4 Conclusions

A detailed mathematical model has been developed for an electroenzymatic Ch sensor to guide the optimization of sensor construction. Model simulations showed the importance of maximizing active enzyme concentration in the immobilized layer and predicted the optimal enzyme thickness to ensure both high sensitivity and fast response time. Therefore, an experimental optimization was conducted whereby enzyme activity retention is first improved followed by an optimization of immobilized enzyme layer thickness. Such an approach resulted in a significantly improved Ch sensor with a 4-6 μm-thick crosslinked ChOx layer on a 200 nm-thick underlying permselective coating of PPD and Nafion, which shortened diffusion times and enhanced H_2O_2 generation near the electrode surface. This design modification led to unprecedent Ch sensitivity of 654 ± 40 nA μM^{-1} cm^{-2} (n = 20) and fast response time of 0.36 ±

0.05 s (n = 8) without compromising selectivity. The improved Ch sensors provide greater flexibility to fabricate more densely arrayed MEAs comprised of near-cellular-scale sensing sites. Such MEAs will facilitate better resolution of choline transients reflective of acetylcholine signals and better correlation of neurotransmitter signaling with electrophysiological activity.

5.5 References

1. J. Du, T. J. Blanche, R. R. Harrison, H. A. Lester and S. C. Masmanidis, *PLoS One*, 2011, **6**, 26204.
2. G. Rios, E. V Lubenov, D. Chi, M. L. Roukes and A. G. Siapas, *Nano Lett.*, 2016, **16**, 6857–6862.
3. J. J. Jun, N. A. Steinmetz, J. H. Siegle, D. J. Denman, M. Bauza, B. Barbarits, A. K. Lee, C. A. Anastassiou, A. Andrei, Ç. Aydın, M. Barbic, T. J. Blanche, V. Bonin, J. Couto, B. Dutta, S. L. Gratiy, D. A. Gutnisky, M. Häusser, B. Karsh, P. Ledochowitsch, C. mora Lopez, C. Mitelut, S. Musa, M. Okun, M. Pachitariu, J. Putzeys, P. Dylan Rich, C. Rossant, W. Sun, K. Svoboda, M. Carandini, K. D. Harris, C. Koch and T. D. Harris, *Nature*, 2017, **551**, 232–236.
4. G. Hong and C. M. Lieber, *Nat. Rev. Neurosci.*, 2019, **20**, 330–345.
5. I. L. Jones, P. Livi and M. K. Lewandowska, *Anal. Bioanal. Chem.*, 2011, **399**, 2313–2329.
6. A. Jaquins-Gerstl and A. C. Michael, *Analyst*, 2015, **140**, 3696.
7. H. Yang, A. B. Thompson, B. J. Mcintosh, S. C. Altieri and A. M. Andrews, *ACS Chem. Neurosci.*, 2013, **4**, 790–798.
8. Z. D. Sandlin, M. Shou, J. G. Shackman and R. T. Kennedy, *Anal. Chem.*, 2005, **77**, 7702–7708.
9. E. C. Rutherford, F. Pomerleau, P. Huettl, I. Strömberg and G. A. Gerhardt, *J. Neurochem.*, 2007, **102**, 712–722.

10 M. C. Parkin, S. E. Hopwood, D. A. Jones, P. Hashemi, H. Landolt, M. Fabricius, M. Lauritzen, M. G. Boutelle and A. J. Strong, *J. Cereb. Blood Flow Metab.*, 2005, **25**, 402–413.

11. K. M. Wassum, V. M. Tolosa, J. Wang, E. Walker, H. G. Monbouquette and N. T. Maidment, *Sensors*, 2008, **8**, 5023–5036.

12. M. L. Rogers, D. Feuerstein, C. L. Leong, M. Takagaki, X. Niu, R. Graf and M. G. Boutelle, *ACS Chem. Neurosci.*, 2013, **4**, 799–807.

13. M. T. Bowser and R. T. Kennedy, *Electrophoresis*, 2001, **22**, 3668–3676.

14. B. Wang, B. Koo, L. W. Huang and H. G. Monbouquette, *Analyst*, 2018, **143**, 5008–5013.

15. M. Wang, N. D. Hershey, O. S. Mabrouk and R. T. Kennedy, *Anal. Bioanal. Chem.*, 2011, **400**, 2013–2023.

16. W. H. Lee, T. Ngernsutivorakul, O. S. Mabrouk, J. M. T. Wong, C. E. Dugan, S. S. Pappas, H. J. Yoon and R. T. Kennedy, *Anal. Chem.*, 2016, **88**, 1230–1237.

17. M. Malvaez, V. Y. Greenfield, A. S. Wang, A. M. Yorita, L. Feng, K. E. Linker, H. G. Monbouquette and K. M. Wassum, *Sci. Rep.*, 2015, **5**, 12511.

18. A. L. Collins, T. J. Aitken, I. Huang, C. Shieh, V. Y. Green, H. G. Monbouquette, S. B. Ostlund and K. M. Wassum, *Biol. Psychiatry*, 2019, **86**, 388–396.

19. J. J. Burmeister, F. Pomerleau, P. Huettl, C. R. Gash, C. E. Werner, J. P. Bruno and G. A. Gerhardt, 2008, **23**, 1382–1389.

20. A. Khan and S. A. Ghani, *Biosens. Bioelectron.*, 2012, **31**, 433–438.

21. D. Jerusalinsky, E. Kornisiuk, I. Izquierdo, J. A. Dani, D. Ji, F. M. Zhou, P. Kasa, Z. Rakonczay, K. Gulya, J. Lemiere, D. V Gool, R. Dom, M. G. Garguilo, N. Huynh, A. Proctor, A. C. Michael, J. Cui, N. V Kulagina, Q. Xin, R. M. Wightman, Z. Huang, R. Villarta-Snow, G. J. Lubrano, G. G. Guilbault, I. Karube, K. Yokoyama, E. Tamiya, J. L. Kawagoe, D. E. Niehaus, E. N. Navera, K. Sode, A. Guerrieri and F. Palmisano, *Biosens. Bioelectron*, 1997, **9**, 1098–1106.

22. S. Ikuta, S. Imamura, H. Misakl and Y. Horiuti, *Purification and Characterization of Choline Oxidase from Arthrobacter globiformis*, 1977, vol. 82.

23. M. G. Garguilo and A. C. Michael, *J. Neurosci. Methods*, 1996, **70**, 73–82.

24. M. G. Garguilo, N. Huynh, a Proctor and a C. Michael, *Anal. Chem.*, 1993, **65**, 523–528.

25. R. Asri, B. O'Neill, J. C. Patel, K. A. Siletti and M. E. Rice, *Analyst*, 2016, **141**, 6416–6421.

26. B. M. Kile, P. L. Walsh, Z. A. McElligott, E. S. Bucher, T. S. Guillot, A. Salahpour, M. G. Caron and R. M. Wightman, *ACS Chem. Neurosci.*, 2012, **3**, 285–292.

27. M. Clay and H. G. Monbouquette, *ACS Chem. Neurosci.*, 2018, **9**, 241–251.

28. I. Huang, M. Clay, S. Wang, Y. Guo, J. Nie and H. G. Monbouquette, *Analyst*, 2020, **145**, 2602–2611.

29. J. J. Burmeister, F. Pomerleau, M. Palmer, B. K. Day, P. Huettl and G. A. Gerhardt, *J. Neurosci. Methods*, 2002, **119**, 163–171.

30. J. J. Burmeister, F. Pomerleau, J. E. Quintero, P. Huettl, Y. Ai, J. Jakobsson, M. Lundblad, A. Heuer, J. T. Slevin and G. A. Gerhardt, 2018, **130**, 327–351.

31. I. Migneault, C. Dartiguenave, M. J. Bertrand and K. C. Waldron, *Biotechniques*, 2004, **37**, 790–802.

32. B. Ghasemzedah, J. Cammack and R. N. Adams, *Brain Res.*, 1991, **547**, 150–154.

33. K. T. Kawagoe, P. A. Garris, D. J. Wiedemann and R. M. Wightman, *Neuroscience*, 1992, **51**, 55–64.

34. F. Fan and G. Gadda, *J. Am. Chem. Soc.*, 2005, **127**, 2067–2074.

35. R. Fleming and L. J. Gosting, *J. Phys. Chem.*, 1973, **77**, 2371–2376.

36. S. B. Hall, E. A. Khudaish and A. L. Hart, *Electrochim. Acta*, 1997, **43**, 579–588.

37. M. Ohta-fukuyama, Y. Miyake, S. Emi and T. Yamano, *J. Biochem.*, 1980, **88**, 197–203.

38. F. Fant and G. Gadda, *J. Am. Chem. Soc.*, 2005, **127**, 17954–17961.

39. J. P. Bruno, C. Gash, B. Martin, A. Zmarowski, F. Pomerleau, J. Burmeister, P. Huettl

and G. A. Gerhardt, *Eur. J. Neurosci.*, 2006, **24**, 2749–2757.

40. V. Parikh, R. Kozak, V. Martinez and M. Sarter, *Neuron*, 2007, **56**, 141–154.

41. A. H. Keihan, S. Sajjadi, N. Sheibani and A. A. Moosavi-Movahedi, *Sensors Actuators B Chem.*, 2014, **204**, 694–703.

42. H. S. Magar, M. E. Ghica, M. N. Abbas and C. M. A. Brett, *Talanta*, 2017, **167**, 462–469.

43. H. Zhang, Y. Yin, P. Wu and C. Cai, *Biosens. Bioelectron.*, 2012, **31**, 244–250.

Chapter 6: Simulated performance of electroenzymatic glutamate biosensors *in vivo* illuminates the complex connection to calibration *in vitro*

Abstract

Detailed simulations show that the relationship between electroenzymatic glutamate sensor performance *in vitro* to that *in vivo* is complicated by the influence of both mass transfer resistances and clearance rates of glutamate (Glut) and H_2O_2 in the brain extracellular space (ECS). Uncertainties in the accuracy of using calibrations *in vitro* to interpret sensor responses *in vivo* have long been present, limiting the value of collected sensor data. Detailed mathematical modeling provides a unique perspective for analyzing sensor response by showing how sensors respond to known sets of conditions in ways that cannot be done physically with existing experimental techniques and systems. Through the use of 1-D model simulations, it is shown that sensor response *in vivo* shows much greater dependence on H_2O_2 mass transfer and clearance in the surrounding tissue than previously thought, potentially leading to sensor measurements more than double the expected value (based on prior sensor calibration *in vitro*) for glutamate release events close to the sensor surface. Sensor response in general is greatly affected by the distance between the sensor and location of glutamate release, with measured apparent concentrations decaying below the actual simulated values at glutamate release distances greater than 3 μm. Simulations of transient glutamate concentrations, including a physiologically relevant bolus release, showed that detection of glutamate signaling likely is limited to events within 30 μm of the sensor surface. Important limitations also exist in how well decays in sensor response represent actual concentration changes, which makes it difficult to use sensor data to determine rates of glutamate uptake in the brain ECS. The model is designed to represent a broad range of relevant physiological

conditions, and although limited to one dimension, provides much needed insight into the interpretation of electroenzymatic sensor data gathered *in vivo*.

6.1 Introduction

Electroenzymatic microsensors have proven valuable for the selective monitoring of chemical species including glutamate (Glut), glucose, ATP, acetylcholine and choline in the deep brain.[1-7] These biosensors are based on one or more immobilized enzymes that serve as the selective recognition element(s) and that generate an electroactive species, commonly H_2O_2, which is oxidized or reduced at an underlying electrode to give a current signal. The electrode normally is coated with one or more permselective polymer layers to prevent electroactive interfering compounds, such as ascorbic acid, from accessing the electrode surface. For example in the case of Glut sensors, glutamate oxidase (GlutOx) commonly is immobilized onto a polymer-coated electrode surface using a cross-linking compound. The immobilized enzyme catalyzes the oxidation of Glut to produce H_2O_2, which is then free to diffuse to the electrode surface where it is electrooxidized to produce a measurable current signal, usually in the picoamp range. The current produced is a function of the exogenous Glut concentration, and the biosensor response is often reported as a concentration measurement calculated using a calibration factor.

Historically, the primary competing technology for deep-brain sensing has been microdialysis. Microdialysis may be employed to detect virtually any neurochemical for which an analytical technique exists, including HPLC, mass spectrometry, LC-MS, *etc*., whereas electroenzymatic sensors have been developed only for the small set of analytes for which appropriate enzymes are available. The typical tradeoffs have been the relatively large size of microdialysis probes compared to electroenzymatic probes and their poor spatiotemporal resolution, although some recent technical advances have reduced these disadvantages.

Of late, genetically encoded fluorescent sensors for neurochemicals, including Glut, have emerged as powerful tools to follow the activity of hundreds of neurons simultaneously.[8-11] However, extensive implementation of the technique is complicated by the limited, mm-scale penetration depth of visible light in the brain, requiring the use of fiber-optic probes or implantable miniaturized microscopes (*i.e*., miniscopes) to stimulate the fluorophores and to monitor the emitted light from deep-brain regions.[12] Light absorption and scattering by brain tissue clearly present obstacles to the use of optical techniques, while neurochemical mass transfer limitations and clearance mechanisms in the brain limit sensor sampling space and can mask neurotransmitter signal characteristics.

The clear advantages and disadvantages of these primary approaches for monitoring neurochemicals *in vivo* suggests that each will have a role going forward in elucidating brain function. Electroenzymatic sensors are well suited to deep-brain measurements where good spatiotemporal resolution and minimal tissue damage are vital. A recent electroenzymatic Glut sensor design offers a several-fold improvement in sensitivity to 320 nA μM^{-1} cm^{-2} and an order-of-magnitude improvement in intrinsic response time (in the absence of external mass transfer resistance) to ~80 ms,[13] which adds to the appeal of the technology.[13]

However, even the fastest electroenzymatic sensors exhibit response times that are too slow to monitor true synaptic neurotransmitter dynamics, which occurs on the millisecond to sub-millisecond time scale. Analysis of sensor response is further complicated by slow diffusive mass transfer of neurochemicals through the brain extracellular space (ECS) to the sensor,[14] which introduces physical limitations that cannot be overcome by any sensor improvements. These considerations highlight the need to formulate validated approaches for the interpretation of electroenzymatic sensor data in order to better establish the true usefulness of these tools for study of neurological processes.

A central issue is the utility of calibration factors obtained *in vitro*, typically by measuring sensor responses to step changes in concentration administered in a rapidly stirred beaker, to

interpretation of sensor data gathered *in vivo*. To date, use of electroenzymatic sensors to study neurotransmitter concentrations has been predicated on the assumption that these biosensors will perform the same in both environments and that the rise and decay of signals from implanted sensors is straightforwardly reflective of corresponding concentration changes *in vivo.* However, the environments employed for calibration where external mass transfer is minimized or essentially eliminated are not reflective of the relatively quiescent deep brain environment where external mass transfer limitations cannot be ignored. A previous theoretical and experimental study of glucose and hypoxanthine biosensors has confirmed this conclusion through an investigation of differences in sensor performance in a stirred beaker, in agar, and in brain tissue. In brain tissue, Newton *et al*. found that the lack of convective mass transfer to quickly transport analyte to the biosensor surface combined with the presence of H_2O_2 clearance mechanisms, resulted in a steady-state sensor response of only ~1.5% of that for the same concentration in a stirred beaker.[15] Detailed models of analyte transport in the brain, including biological uptake and clearance mechanisms, must be combined with biosensor models to properly analyze data collected *in vivo*.

To understand how Glut sensors perform in the complex environment of the brain, a simulation strategy using an accepted model of diffusive mass transport and sensible ranges of average Glut and H_2O_2 uptake and clearance rates is applied for a number of Glut release scenarios at varied distance from the biosensor. Although this one-dimensional model is an approximation, it is known to be a reasonably good one for description of transport to typical sensors with characteristic dimension >25 μm.[16] The sensor parameters used in this study correspond to a theoretically optimized design of the sort shown in Fig. 6.1 with sensitivity of 364 nA μM^{-1} cm^{-2} and response time of 8 ms whereas the best measured instrinsic response time (in the absence of external mass transfer resistance) is ~80 ms.[13] These simulation results therefore correspond to somewhat aspirational sensor spatiotemporal resolution *in vivo*, yet still illustrate well the key issues encountered in the interpretation of sensor data. Of course, these

findings apply best to Glut biosensors of the particular design described here, yet they are expected to be qualitatively relevant to electroenzymatic sensors of related construction.

6.2. Results and Discussion

6.2.1 Model development and simulated sensor response to concentration step changes in the brain ECS

A detailed, transient mathematical model in one spatial dimension (1-D) was developed to describe Glut sensor performance *in vivo*, and to study the sensitivity of simulation results to parameters describing the clearance of Glut and H_2O_2 from the ECS. This model builds upon a previously published mathematical description of sensor performance *in vitro* under conditions where external mass transfer resistance was minimal[13, 17] to include an additional, brain ECS domain where the rates of chemical diffusion to and from the sensor as well as the biological clearance rates of Glut and H_2O_2 are included. These rates of external mass transfer and clearance often are not of concern when a Glut sensor is calibrated in a stirred beaker, yet they play an important role in sensor performance *in vivo*. This importance has been corroborated by previously reported simulations of electroenzymatic sensors implanted in a gel or tissue and exposed to constant analyte concentration.[15]

However, an understanding of sensor response to *transients* in neurotransmitter concentrations as well as the influence of varied clearance and uptake rates within the ECS clearly is of central importance for the interpretation of sensor data used to study actual brain function. Noting that many of the properties affecting the clearance of neurochemicals from the ECS are expected to vary from one region to another, as well as over time, the model simulations presented here were run over a range of reasonable values (high, middle, or low) to capture the effects of temporal and spatial variability in the brain (see Methods). However, modeling in 1-D has some intrinsic limitations, including the description of neurotransmitter release. For example, the difference between synaptic dimensions and sensor sites (~40-150

μm) cannot be addressed in 1-D models that describe only the depth into sensor coatings, not the size of the sensor itself. Nevertheless, transport to the sensors themselves is expected to be modeled well in 1-D, since their characteristic dimensions exceed 25 μm.[16]

Since sensor calibration *in vitro* normally is conducted by recording sensor responses to step changes in Glut concentration, initial simulations were conducted for comparison purposes for step changes to 10 μM Glut at various distances from the sensor, δ, in the simulated ECS (Fig. 6.1a). (A Glut concentration of 10 μM was chosen since it appears to be representative of the peak concentration observed in the mammalian ECS.[18] Since concentration changes originate at a distance from the sensor surface, the step change was specified at increasing distances from the sensor to assess how well sensors may describe a well-defined change in concentration beyond their immediate vicinity *in vivo*.

For a calibration factor obtained from data gathered *in vitro* to be useful directly, sensor responses to actual Glut concentration in the simulated ECS should be predictable straightforwardly by applying the corresponding calibration factor. For the simulations shown in Fig. 6.2 and elsewhere in this study, the sensor is characterized by a calibration factor of 21.85 pA/μM for Glut concentrations within the sensor's linear range. Surprisingly, simulations show that when a step change in concentration occurs close to the sensor surface (<3 μm) sensor current signals correspond to apparent concentrations (based on the calibration factor) that are much higher than the actual imposed concentration of 10 μM in the release zone (Fig. 6.2). For step changes in concentration more distant from the sensor surface, sensor response is reduced significantly relative to that expected for a sustained 10 μM release, dropping to 25% of the expected response for Glut release at a distance of 10 μm and to below 7.6% of the expected response for Glut released at 20 μm. For the simulated range of Glut and H_2O_2 clearance rates, the sensor response was greater for slower rates and lower for faster rates, as shown by the error bars in Fig. 6.2. These simulations suggest that the relationship between

sensor performance *in vitro* in the absence of external mass transfer limitations to sensor performance in a simulated brain environment is not straightforward.

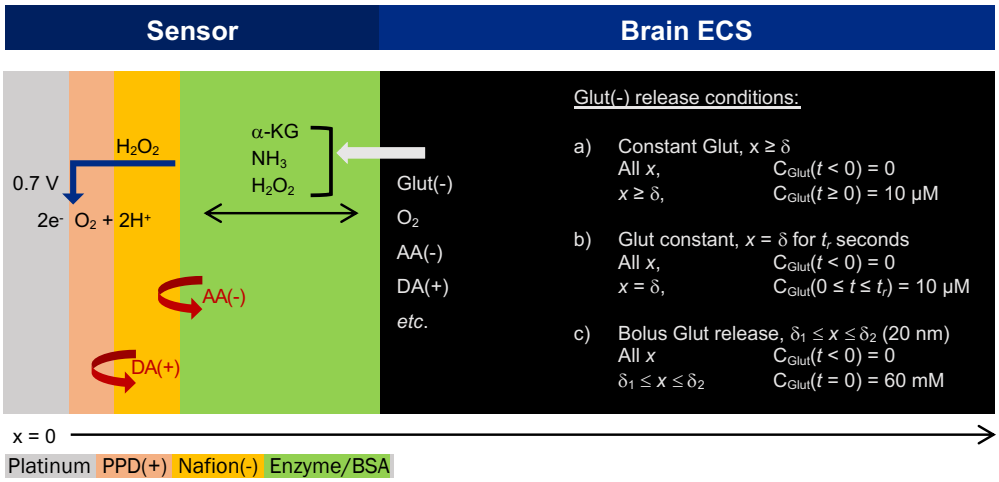

Figure 6.1. Sensor schematic and the set of conditions used to model Glut release into the brain ECS. Equation 1 (see Methods) describes the diffusion and reaction of Glut, O_2 and H_2O_2 within each 1-D domain (PPD, Nafion, Enzyme/BSA, and Brain ECS). Ascorbic acid (AA), dopamine (DA), α-ketoglutarate (α-KG), NH_3, and H^+ are not modeled.

Table 6.1. Rate constants for Glut uptake and H_2O_2 clearance (s^{-1})

Species	Slow	Moderate	Fast
Glut	4.33 s^{-1}	4.95 s^{-1}	7.7 s^{-1}
H_2O_2	0.0116 s^{-1}	5 s^{-1}	30 s^{-1}

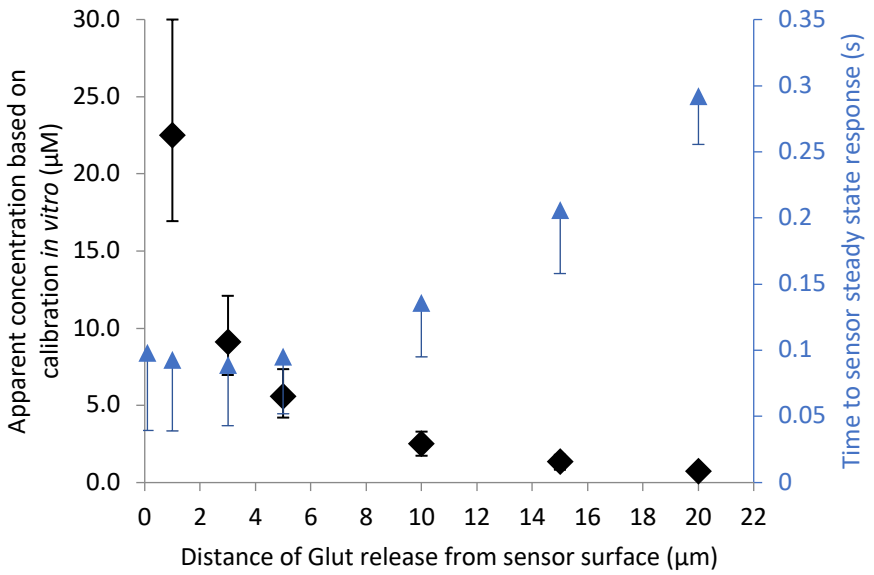

Figure 6.2. Simulated biosensor response *in vivo* to a 10 μM step-change in Glut concentration at varied distances for moderate Glut and H_2O_2 clearance rates. Apparent concentration measurements were calculated using the calibration factor (21.85 pA/μM) obtained *in vitro*. The time periods required for the approximate steady-state responses represent the time to 90% of the actual steady-state values, consistent with calibration procedures *in vitro* (see text). Error bar termini correspond to the slow and fast biological clearance rates of Glut and H_2O_2 given above (see Methods) where slower rates resulted in higher sensitivities and longer response times. Steady-state response times for the slowest H_2O_2 clearance rate (for any Glut uptake rate) were omitted since achievement of steady state required >80 s.

The large deviations in sensor response from what might be expected (Fig. 6.2) arise from the significant mass transfer resistance to species transport to and away from the sensor surface *in vivo* as well as chemical clearance mechanisms in the brain ECS. A rapidly stirred beaker often is used for calibrations *in vitro*, which minimizes mass transfer resistances between the sensor and bulk fluid. Stirring results in rapid convective transport of Glut and O_2 to the sensor surface and rapid removal of typically most of the H_2O_2 produced in the sensor enzyme layer. It is important to note that the Glut concentration at the sensor surface never achieves the concentration released (10 μM in this case) as the system approaches steady

state whether *in vivo* or *in vitro*. Sensor response is related to the rate of Glut transport to the sensor, the rate of Glut uptake in the brain, the rate of Glut turnover in the GlutOx layer of the sensor, and ultimately, the delivery of H_2O_2 to the Pt electrode surface where H_2O_2 is electrooxidized to give rise to the current signal. For example, for a Glut step change to 10 μM at 5 μm from the sensor *in vivo*, a sensor surface concentration of <2.6 μM provides the driving force for Glut diffusion to the sensor surface at steady state and a current signal corresponding to a bulk concentration of ~6 μM Glut (based on *in vitro* calibrations). Since resistance to mass transport of H_2O_2 from the sensor surface also is greater *in vivo*, a greater fraction of H_2O_2 produced may be transported to the Pt electrode surface which can give rise to larger sensor current signals *in vivo* than expected (Fig. 6.2), particularly when Glut release events occur relatively close to the sensor surface. Representative concentration profiles for Glut, H_2O_2 and O_2 both within the sensor coatings and the brain ECF at steady state for Glut release maintained at 10 μM at 5 μm from the sensor surface are shown in Fig. 6.3. Note that the slopes of the concentration profiles at the sensor surface provide an indication of the diffusive mass transfer rates of the chemical species between the sensor surface and the simulated ECS.

Prior simulations of sensor calibration *in vitro* (using the same sensor parameters but including convective mass transfer at the sensor surface and a mass transfer coefficient of 0.5 cm/s for H_2O_2) indicate that only ~15% of the H_2O_2 arising from Glut oxidation catalyzed by GlutOx immobilized in the sensor surface layer diffuses to the underlying Pt electrode where it is electrooxidized to give a current signal; most of the H_2O_2 diffuses to the sensor surface where it is flushed away rapidly to the bulk solution by convective mass transfer. In the brain, mass transfer of H_2O_2 from the sensor surface to the ECS occurs primarily by a much slower diffusive mechanism, which is enhanced somewhat by biological mechanisms that clear H_2O_2 at relatively slow first-order rates. These H_2O_2 clearance mechanisms primarily result from catalase activity and the glutathione system and exhibit characteristic times ranging from 0.1 s to minutes.[19-21] Nevertheless, the slower removal rates of H_2O_2 can lead to not only higher

sensor signals *in vivo* than expected from calibrations *in vitro* as mentioned above but also to a moderate accumulation of H_2O_2 in the brain in the vicinity of the sensor. However, this H_2O_2 accumulation is not expected to show any toxic effects unless it well exceeds 10 μM.[22] For moderate rates of H_2O_2 clearance (5 s^{-1}) the highest accumulation of H_2O_2 for the sensor responses shown in Fig. 2 is 10 μM (faster and slower expected clearance rates result in peak concentrations of 7.25 and 13.5 μM, respectively) for Glut release at 1 μm and in all cases this value drops by ~60% or more for release 3 μm or greater from the sensor surface. Sensor response scales with H_2O_2 concentration at the electrode surface which can be augmented for Glut release events closest to the sensor surface that give rise to local H_2O_2 accumulation.

The intrinsic response time for these sensors is defined in accordance with common practice in the field, namely the time required for the sensor to reach 90% of the steady-state response to a step change in bulk Glut concentration in a system where external mass transfer resistance between the sensor and the bulk solution essentially is eliminated (by rapid stirring for example). The simulations presented here (Fig. 6.2) suggest that much longer times generally are required to approach steady state *in vivo*, typically >90 ms vs 8 ms *in vitro* for an ideal optimized sensor of the design shown in Fig. 6.1,[13] depending on sensor proximity to the Glut source and H_2O_2 clearance rate. This order-of-magnitude difference between simulated sensor response *in vivo* and the intrinsic sensor response time also arises from the slow rate of diffusive transport between the brain and the sensor surface. When Glut release occurs very close to the sensor surface, within a few microns for example, the steady-state Glut concentration profile over this small distance sets up quickly whereas the H_2O_2 profile, which extends 10s of microns into the brain, approaches its steady-state character much more slowly. Thus, H_2O_2 mass transfer and clearance rates control the apparent response of the sensor *in vivo*. For example, for Glut release <1 μm from the sensor surface, the Glut profile becomes constant after ~10 ms, whereas the H_2O_2 concentration profile approaches steady state at ~100 ms thereby controlling the apparent sensor response. H_2O_2 mass transfer and clearance

becomes progressively less controlling as the distance between the sensor surface and the point of Glut release is increased (Fig. 6.2).

As expected, the overall apparent sensor response time increases almost linearly with distance for Glut release distances from the sensor >5 μm. Surprisingly, the opposite trend is shown for the closest Glut release distances. This can be explained by examining the steady-state Glut profiles. At short release distances, there is enough Glut entering the sensor layer to be driven to the Nafion/enzyme layer boundary, where the concentration begins to increase nonlinearly for distances of less than 3 μm. Any H_2O_2 produced here by the accumulating Glut will have an added mass transfer resistance against diffusing back to the outer edge of the sensor, causing an increased response time. At greater release distances, where Glut is fully consumed before reaching the enzyme/Nafion boundary, more H_2O_2 is produced at the outer edge of the immobilized GlutOx layer where it can diffuse directly into the brain thereby resulting in quicker attainment of steady state.

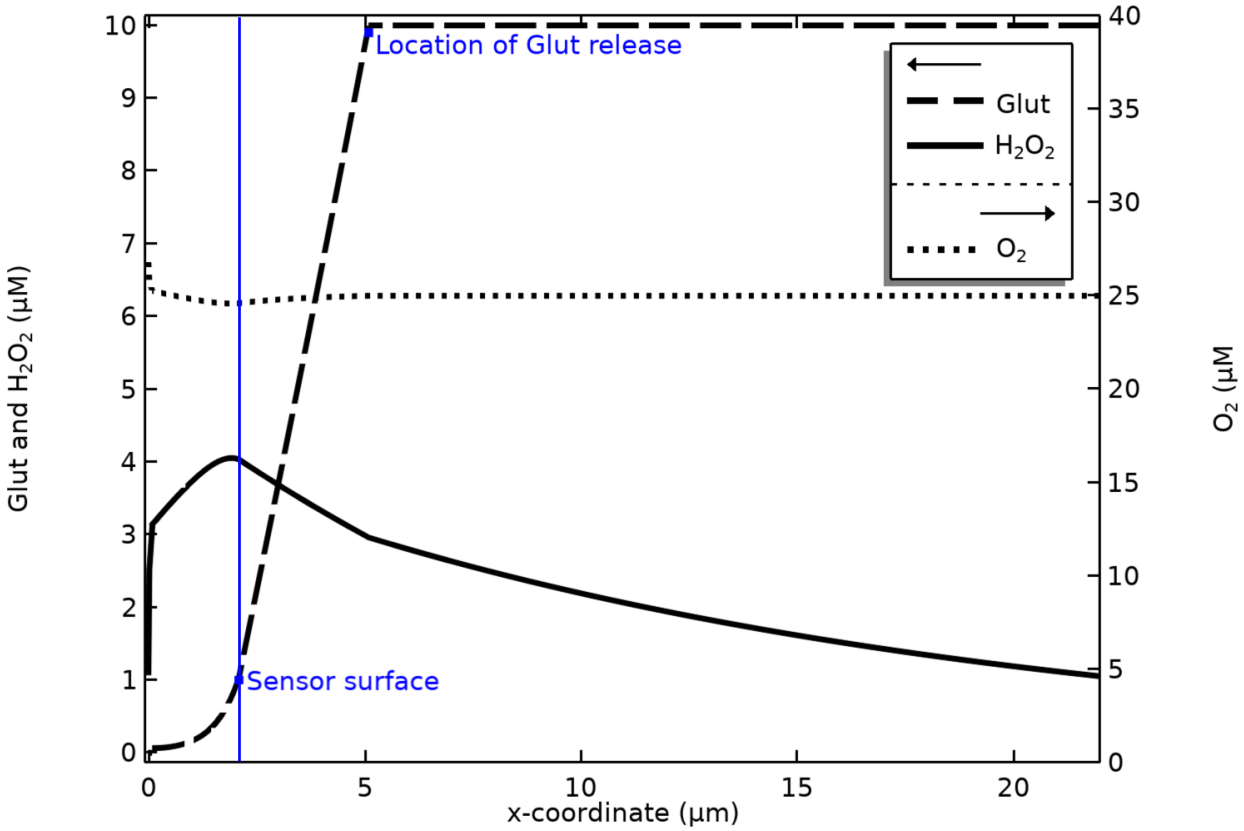

Figure 6.3. Steady state concentration profiles after a 10 μM step-change in Glut 5μm from the sensor surface (sensor surface is located at x = 2.093 μm). H_2O_2 concentration decreases asymptotically to 0 for x > 2.093 μm.

In considering the distances traveled by diffusing molecules in the brain, it is important to acknowledge how the tortuosity of diffusion paths in the brain ECS impacts apparent or effective diffusivities by increasing relative diffusion distances. The anisotropic nature of the brain also influences mass transport, an effect that has been exploited for creation of detailed maps of neural connections using diffusion weighted magnetic resonance imaging: for example, the diffusion of water has been shown to be significantly faster in the axial direction of myelinated axons.[23] These differences are often characterized in terms of the fractional anisotropy (FA), relating the magnitude of diffusivity in primary, axial (faster) and radial (slower) directions. In studies of brains in developing Sprague Dawley rats, FA stabilized through developmental cycles to a value of about 0.3.[24] This corresponds to diffusion in a primary direction that is 1.67

times the average value and diffusion in radial directions 0.667 times the average value. This could increase or decrease the distance at which sensors can detect Glut depending on where the probe is located within the brain and could prove to be an important factor in deciding where to implant sensor probes. However, in order to reduce the complexity of the simulations conducted here while still addressing the main points of discussion, the brain medium is assumed to be isotropic with a void fraction of 0.2 and tortuosity of 1.6, as detailed in the methods.[14]

Although the Glut step change modeled in these initial simulations may not be realistic biologically, these results highlight the impact of the dramatically different conditions used for calibrations *in vitro* and for measurements *in vivo* on sensor response. Simulations of sensor response *in vivo* to transient Glut release described below provide further indication that calibration plots and response time measurements obtained by the typical means *in vitro* cannot be used straightforwardly for the interpretation of sensor data gathered *in vivo*.

6.2.2 Simulated sensor response to transient Glut release events at fixed distances in the brain ECS

Figure 6.2 shows that if Glut concentrations are not maintained at the site of release for >0.09 s, steady-state sensor responses will not be reached for the conditions explored, and the device will provide a signal corresponding to a lower Glut concentration, except for release events very close to the sensor surface. Since it is unlikely that Glut concentration transients *in vivo* occur on such lengthy time scales, the time course of the release event and its distance from the sensor surface will further reduce sensor response below the value expected (based on calibrations *in vitro*). Figure 4 shows simulations of the ideal optimized sensor response if Glut concentration were held constant at specific distance points from the device for very short periods of time (1-10 ms). This scenario corresponds to a rectangular Glut concentration pulse in time at a point location (Fig. 6.1b). This study is intended to investigate how closely a sensor

signal time course might be expected to describe a clearly defined, transient pulse in Glut concentration in a simulated ECS environment. The specific release times investigated (1, 5, and 10 ms) are intended to approximate *in vivo* timescales. For example, recordings from rat nucleus accumbens using relatively fast electroenzymatic sensors recorded exocytosis events with apparent sub-millisecond rise times and ms decay times, resulting in Glut presence near the synapse over the range of 1-5 ms.[25]

Simulated sensor responses to 10 μM Glut concentration releases are shown to vary significantly depending on how long the concentration is maintained and the distance between the sensor and the point of release (Fig. 6.4). Sensor current signals generally correspond to underestimates of the actual 10 μM Glut release concentration, except for some release events very close to the sensor, which is consistent with the results illustrated in Fig. 6.2 for step changes in Glut concentration at varied separations from the sensing site.

It is also notable that although all sensor responses shown in Fig. 6.4 have a similar asymmetric shape, a more distant Glut release event results in a broader signal. The decay rate of sensor responses has been used by some to estimate the extracellular residence times and cellular uptake rates. However, comparing the simulated sensor signal decay profiles with the actual decay in Glut concentration at the release point and also the simulated component of Glut concentration decline due to biological uptake from the ECS (Fig. 6.4) shows how difficult it would be to determine such Glut uptake rates directly from signal decay data. The declining sensor signal results from a combination of Glut uptake from the ECS, actual Glut consumption by the sensor, and diffusion of Glut in the positive *x*-direction away from the release site. Among these influences, the effect of the sensor is minor, but can be observed by comparing the time profiles of the dotted lines across different release point distances. For release at 1 μm, the Glut concentration decays most quickly; however at 5 μm and 15 μm, the Glut time courses are slower and nearly indistinguishable indicating that consumption of Glut by the sensor has become inconsequential.

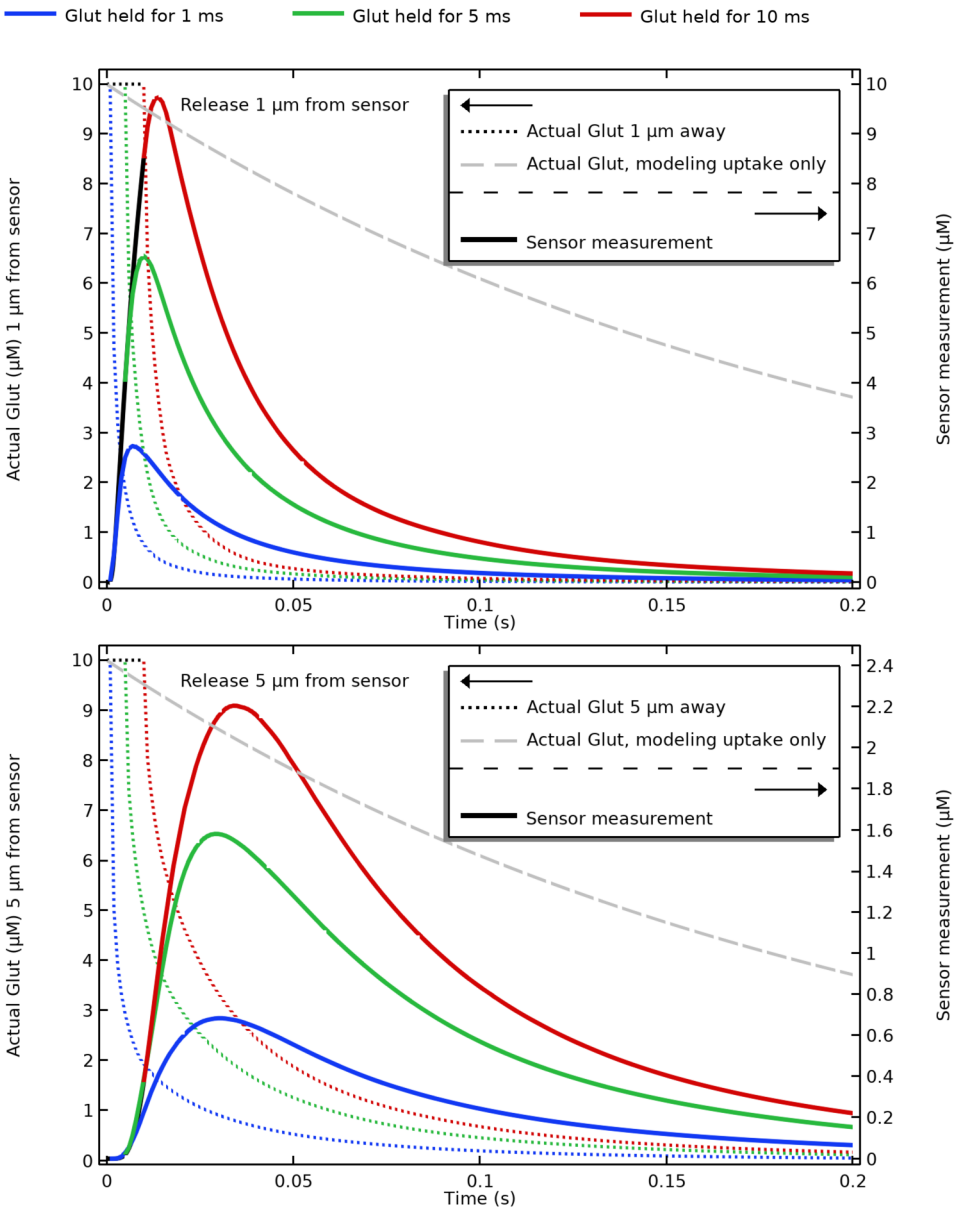
Glut held for 1 ms
Glut held for 5 ms
Glut held for 10 ms
Release 1 µm from sensor
Actual Glut 1 µm away
Actual Glut, modeling uptake only
Sensor measurement
Actual Glut (µM) 1 µm from sensor
Sensor measurement (µM)
Time (s)
Release 5 µm from sensor
Actual Glut 5 µm away
Actual Glut, modeling uptake only
Sensor measurement
Actual Glut (µM) 5 µm from sensor
Sensor measurement (µM)
Time (s)

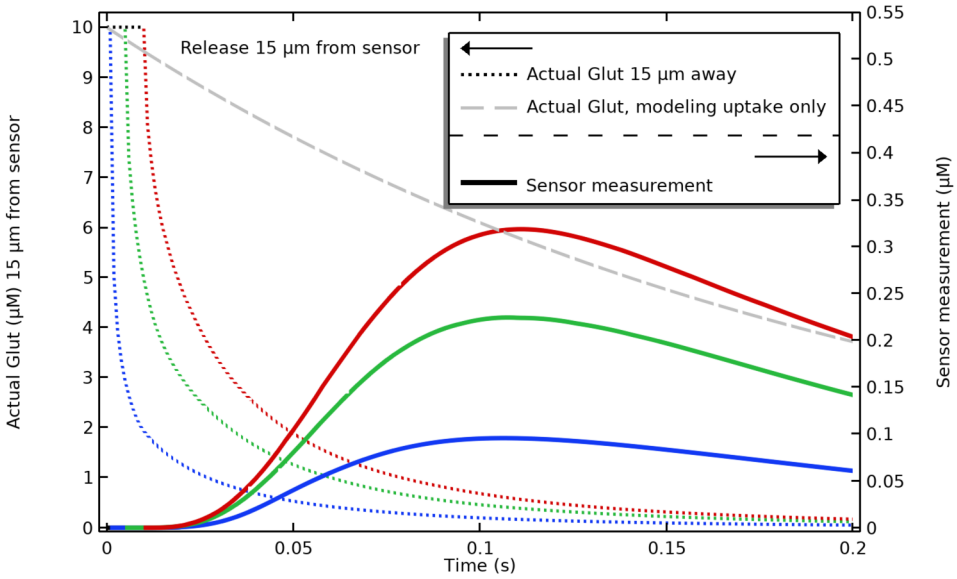

Figure 6.4. Sensor response to transient Glut release at various distances from a sensor. Black portions of solid curves show sensor response while Glut is maintained at 10 µM. The dashed gray curves show modeled Glut disappearance due only to an imposed biological uptake corresponding to a 4.95 s^{-1} rate constant. Simulations were conducted using the moderate rate constants for Glut uptake of 4.95 s^{-1} and for H_2O_2 clearance of 5 s^{-1}. The dotted curves show the actual Glut concentration at the release site. In all plots, the blue, green and red curves represent data for release times of 1 ms, 5 ms, and 10 ms, respectively.

Of course, simulation of Glut release in this way lumps together the many factors that actually influence Glut release and concentration regulation in the ECS. These factors may include variations in the number of vesicles releasing Glut during signaling events, the number of molecules contained in each vesicle, the fraction of molecules released by each vesicle, local geometric constraints, unique synaptic structures, the fraction of Glut spillover into the ECS, and even the possibility of Glut release from astrocytes, which has been observed in response to inflammatory conditions[26] that could be caused by probe insertion. After 1, 5, or 10 ms of maintained Glut concentration there would be approximately 15, 20, or 30 million molecules present in the ECS, assuming outward diffusion from a point into a spherical region. However, due to the 1-D nature of this model, the actual numbers of molecules needed to produce these

simulated sensor responses would be higher, unless sensor sites are miniaturized significantly. These Glut numbers are still 10-100 times the number found inside a single presynaptic vesicle,[27] and do not account for molecules that were taken up from the ECS in those time periods. These 1-D simulations, therefore, should be understood as simplified representations of concurrent release from multiple vesicles and/or synapses.

6.2.3 Simulated sensor response to bolus Glut release events in the brain ECS

Sensor response was also simulated for single, bolus-type releases of Glut into the ECS at varied distances from the sensor. This scenario roughly represents how sensors respond to neurotransmitter release from synaptic vesicles where it is assumed that synaptic vesicles release Glut instantaneously into a volume roughly the size of a synapse, simulated as a 1-D, 20 nm wide region in the ECS, resulting in localized concentrations near 60 mM.[28] After release, Glut diffuses through the ECS and the responses of sensors at various distances from the release site are simulated (Fig. 6.5A). The concentrations of Glut within the ECS at the time of the maximum sensor responses also are shown in Fig. 6.5B. The model conditions for these simulations are given in Fig. 6.1c. Simulations corresponding to the extrema of the range of plausible uptake and clearance rates of Glut and H_2O_2 are shown by the dashed lines, although the differences are less pronounced than under the steady-state conditions presented in Fig. 6.2. However as in Fig. 6.2, higher sensor responses are observed for slower clearance and uptake rates and lower responses are observed when these rates are faster.

At simulated times corresponding to maximum sensor response, actual concentrations in the brain ECS are much lower than the initially imposed 60 mM and vary significantly over micron-scale distances (Fig. 6.5B), complicating analysis of how well a sensor reports the actual concentration in the brain, since the actual concentrations show large spatiotemporal variations. It is important to note once again here that the sensor response at any moment is generated from the rate of electrooxidation of H_2O_2 at the Pt electrode surface, which is directly related to

the flux of H_2O_2 within the sensor coatings arising from the turnover of Glut by the immobilized GlutOx and the flux of Glut to the sensor surface. As time progresses, the peak Glut concentration diminishes due to Glut diffusion into the simulated ECS in the positive *x*-direction and Glut clearance from the ECS, which results in a decreasing slope in Glut concentration at the sensor surface and a decay in the sensor signal. The effect of Glut consumption by the sensor on simulated Glut concentrations is minimal, although its impact is reflected in the slight shift in the peak centers away from the original 10, 15, 20, or 30 µm release locations, as shown in Fig. 6.5B.

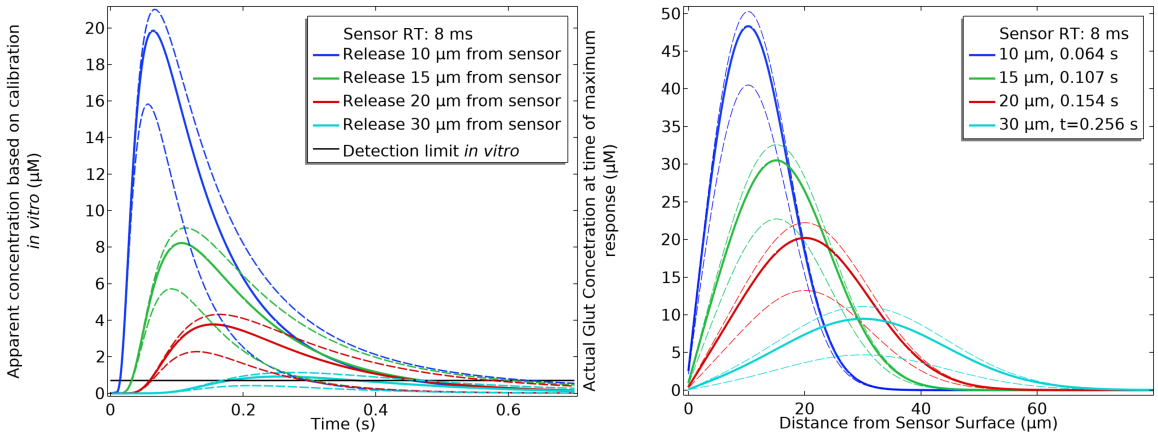

Figure 6.5. A: Simulated sensor concentration measurements after bolus releases of Glut at varied distances from the sensors within a 20 nm, synaptic scale region, where Glut is specified to be 60 mM at *t* = 0. B: The actual Glut concentration profiles in the brain plotted over the distance from the sensor surface, taken at the times of maximum response for releases at each distance. Dashed lines show the effects of slower and faster uptake or clearance rates of Glut and H_2O_2 corresponding to the smaller and large rate constants presented in the table in Fig. 6.2, where slower uptake rates result in higher concentrations.

These 1-D simulations make it appear that it may be possible to observe single, synaptic releases of Glut. However, by modeling in 1-D we are assuming that the concentration at the release distance is constant across the sensor surface; in reality the synapse is much smaller

than the sensor, and the true sensor response to a single synaptic release may be much lower. Also, the apparent Glut concentrations corresponding to sensor signals vary significantly depending on the distance between the sensor and location of Glut release, despite the identical Glut release conditions specified for each sensor/release site separation distance. For Glut released farther from the sensor surface, response is lowered and broadened. For distances greater than 30 μm, even with the 1-D simplifications that overestimate response, simulated response remains below the detection limit, which has been characterized experimentally as 0.7 μM (detection limit is defined as the concentration at which sensor response is 3× that of the noise). However, this 1-D simulation cannot provide a quantitative prediction of the maximum sensor/release site separation distance that could give rise to a detectable signal. Regardless, these distances are far shorter than the range of electrophysiological recordings (100-200 μm).[10] Fortunately, the peak broadening effect that occurs over increasing release distance suggests that it may be possible to correlate the peak widths or rise times to the distance between the sensor and Glut source, although this would require experimental validation and careful consideration of relevant assumptions including the time course of Glut release, the concentration achieved in the synapse, and the Glut leakage rate from the synapse.

It is suspected that in reality only a fraction of the neurotransmitters are released during exocytosis,[29] which would reduce the initial Glut concentration and simulated sensor signals, although not enough is known to account quantitatively for partial neurotransmitter release. This consideration, along with the 1-D nature of the model, suggest that the simulations likely overestimate the sensor signal and that these results should be understood as a maximum possible sensor response.

Nevertheless, these simulation results qualitatively agree with experimental measurements made with less-than-optimal versions of these sensors that had response times *in vitro* of ~0.8 s. In an experimental study *in vivo*, Glut release was detected following cortical

stimulation in the nucleus accumbens of anesthetized rats that decayed to 30% of baseline within 3.5 s.[30] In the basolateral amygdala, similar sensors detected transient increases in extracellular Glut of ~1μM in the time surrounding reward-seeking decisions with transient release frequencies observed on the order of 1 to 8 per second, depending on the rat's activity. [31] Another study entailed injection of nanoliter volumes of 500 μM Glut at ~100 μm from the sensor surface, resulting in a measured value ~25% of the sensor response to 500 μM *in vitro* with signal decay occurring over 3-5 s.[32] Amplitude, rise time, signal decay and asymmetric signal response in these cases all are consistent with the simulations shown here corresponding to Glut release >20 μm from the sensor surface.

6.3. Methods

6.3.1 Models and simulation methods

Mathematical models were used to simulate diffusion and reaction of the three chemical species of primary interest in modeling Glut biosensor performance *in vivo*: Glut, O_2 and H_2O_2.[17] These processes are described by separate time-dependent mass balance equations for each chemical species in each coating layer of the biosensor (Fig. 6.1) as well as in the brain ECS (four separately defined domains, each described by three linked partial differential equations corresponding to the three species of interest, as seen for the ECS in Equation 6.1). The equations used to describe the biosensor, in one spatial dimension (1-D), were reported in our earlier work.[13, 17] In these models, Glut is excluded from the negatively charged Nafion layer using a large partition coefficient of 1000, with equal fluxes and concentrations for all species at all other internal (within sensor layer) boundaries. Others have published a 1-D model of species diffusion and reaction in the brain ECS suitable for our purposes,[14]

$$\epsilon_b \frac{\delta C_i}{\delta t} = \frac{\epsilon_b}{\lambda^2} D_i \frac{\delta^2 C_i}{\delta x^2} + \epsilon_b r_i(C_i) \qquad (6.1)$$

i = Glut, H_2O_2, O_2; j = PPD, Nafion, enzyme, brain ECS

In this model, brain porosity and tortuosity of diffusion paths in the ECS are represented by ϵ_b and λ, respectively. The concentration of species *i* within the ECS is C_i, its molecular diffusivity in water is D_i, and its clearance rate from the ECS is $r_i(C_i)$.

Boundary and initial conditions for the brain ECS varied depending on the simulation being performed; a general visualization of the 1-D domains and simulation initial conditions are provided in Fig. 6.1. In all simulations, equal diffusive fluxes for the ECS domain at the sensor immobilized enzyme layer/ECS boundary were specified, using Equation 2, where $\alpha_e D_i$ represents the effective diffusivity through the enzyme layer of species *i*.

$$\frac{\epsilon_b}{\lambda^2} D_i \frac{\delta C_{i,b}}{\delta x} = \epsilon_e \alpha_e D_i \frac{\delta C_{i,e}}{\delta x} \tag{6.2}$$

At the same boundary in the immobilized enzyme domain, concentrations were set to be equal to that in the ECS (no concentration partition was specified between these domains). At the edge of the ECS far from the sensor, Glut and H_2O_2 were set to be 0 μM while O_2 was set to a bulk *in vivo* concentration of 25 μM (see below). To ensure this boundary condition did not influence simulation results, the length of the domain was increased until further increases did not affect simulation results. Initial conditions generally specified Glut and H_2O_2 at 0 μM and O_2 at 25 μM, although some parts of the ECS domain set Glut to a different value in some simulations. To simulate Glut being held at 10 μM for specified time periods, first a constant concentration boundary condition was used for the given time period, then it was removed, and finally the simulation was continued using data from the last time point as the initial conditions.

Solutions to these sets of equations and boundary conditions were found numerically using COMSOL Multiphysics (COMSOL, Inc, Los Angeles). Equations were entered using the coefficient form PDE interface. At internal domain boundaries, it was necessary to select the "apply reaction terms on individual dependent variables" option to ensure boundary conditions

remained as specified. Time-dependent solutions were found using the default, fully coupled multifrontal massively parallel sparse direct solver (MUMPS). Time steps and variable tolerances were adjusted as necessary, depending on the simulation.

A number of assumptions are implicit in these models. In using Fick's Law to construct the diffusion equations, it is assumed that all regions have a homogeneous nature and that concentrations are low. Other previous assumptions concerning the sensors also apply,[17] including the application of free-enzyme kinetic rate constants for immobilized enzyme, no loss in GlutOx activity upon immobilization and over time, and the nonparticipation of the ammonia byproduct in the reactions of interest. The fraction of active GlutOx in the enzyme layer is assumed to be 0.1, fitting *in vitro* experimental data.[13] It is also important to realize that 1-D models require area-averaged rates and assume homogeneity and temporal consistency in these rates.

6.3.2 Selection of H_2O_2 clearance, Glut uptake, and O_2 bulk concentration parameters

It is assumed that appropriate ranges of rate constants for Glut uptake and for H_2O_2 clearance from the brain ECS can be used to encapsulate the spectrum of conditions expected, making the model more widely applicable over different regions of the brain. The clearance rates of H_2O_2 and Glut from the brain ECS can greatly affect simulated sensor response *in vivo*, and are expected to vary depending on many biological factors including differences due to anisotropy, location within the brain, and the influence of other neurotransmitters and neuromodulators. These considerations led to the performance of multiple simulations for each set of Glut release conditions in order to explore a representative range of H_2O_2 and Glut clearance rates described as fast, moderate, and slow in the discussion of simulation results. Further considerations that must be made when interpreting these results concern the likelihood of tissue damage resulting from probe insertion,[33] which would likely affect the rates of clearance and uptake. If a blood vessel is ruptured on insertion, for example, a layer of red

blood cells would be expected over the sensor surface[33] and would alter normal biological rates for that region of the brain; accumulation of glial cells has also been observed near inserted electrode probes.[18] Ultimately, the values for first-order clearance or uptake rates (Fig. 6.2) were selected based on available literature data and from observations made from sensor use *in vivo* over a range that should be applicable to most *in vivo* conditions.

Prior data gathered *in vivo* with sensors constructed on microelectrode array (MEA) probes did not show evidence of crosstalk between sensor sites arrayed ~50 μm apart, suggesting that any H_2O_2 produced at one site is diluted into or cleared by the surrounding ECS before it can diffuse to an adjacent site at sufficient concentration to give a signal. Simulations were performed to determine the minimum clearance rate required for crosstalk to be absent. For sensor spacings of 40 μm on a MEA probe, a clearance rate constant >5 s^{-1} is required. This is consistent with the rate constant measured for cultured Jurkat T cells of 4.5 s^{-1},[19] and was chosen as the mid-range parameter. An upper bound was found by repeating the simulation assuming that crosstalk would not be observed for a smaller sensor spacing of 20 μm, in this case showing rate constants >30 s^{-1} would be required. Studies of cultured neurons and astrocytes displayed slower clearance rates on the order of minutes,[20] leading to specification of a slow rate constant representing a 1 minute halftime (0.0116 s^{-1}). Other cell types show similarly slow clearance of H_2O_2, including for the red blood cells that may be present in cases of insertion damage. For example, mouse red blood cells have shown a H_2O_2 clearance rate constant of 0.048 s^{-1}.[21] Rates this slow would likely result in significant crosstalk between sensors under sustained Glut exposure, but this value was included as the lower bound that may be situationally accurate for certain instances and locations in the brain.

Clearly, measurement of the extracellular H_2O_2 present during Glut monitoring could help improve sensor accuracy. Furthermore, it is worth mentioning that evoked H_2O_2 has neuromodulatory effects and is known to be produced from additional sources in the brain. For example, electrical stimulation of dopaminergic axons has been shown to produce H_2O_2 along

with neurotransmitters.[34] The possibility of these effects were not incorporated into this model, but may be worth consideration. In some cases, they could cause a greater sensor response due to H_2O_2 evoked by neuronal stimulation. The importance of H_2O_2 production and regulation on biosensor accuracy are unexpected and complex, and the topic deserves further independent study.

The range of Glut uptake rate constants used was taken from data obtained via a genetically encoded glutamate sensing fluorescent reporter (SuperGluSnFR) technique in cultured hippocampal neurons, where Glut dynamics were recorded after electrically stimulating neural tissue at different frequencies.[11] Middle, upper, and lower bounds for Glut uptake rate constants were estimated from this data, where the uptake rate from a single stimulation resulted in the fastest uptake and repeated, high-frequency stimulations resulted in the moderate and slower uptake rates. These rate constants likely result in overestimates of Glut uptake rate since diffusion is not accounted for in the experimental measurements, however they provide a good initial set of values for simulations.

Oxygen concentration was fixed for all simulations at a level such that it would not influence results, which is a reasonable approximation based on previous sensor simulations showing that O_2 is not limiting unless the concentration of Glut is held constant at a concentration more than triple that of O_2.[17] Since the concentration of O_2 in the brain ranges from 5-50 μM, similar to that expected for Glut,[35] simplifications to ignore oxygen dependency are not expected to influence simulation results.

6.4. Conclusions

A mathematical model was developed to simulate the performance *in vivo* of electroenzymatic Glut sensors, which highlights the complex relationship to calibration *in vitro* that is dependent on sensor placement relative to locations of Glut release and the local rates of Glut uptake and H_2O_2 clearance from the brain ECS. Ranges of values for the volume-averaged

uptake and clearance rate constants for Glut and H_2O_2 were chosen to represent the range of their probable variations, spatially and temporally, in the brain. Rates of H_2O_2 clearance were shown to be most significant in affecting steady-state sensor signals and apparent response times, which implies a need for additional experimental study of H_2O_2 concentration regulation in the brain. Simulations of sensor steady-state responses to a 10 μM step-change *in vivo* showed that apparent sensor concentration measurements (based on calibration factors obtained *in vitro*) can be more than double the actual concentration for Glut release events very close to the sensor due to H_2O_2 diffusive mass transfer resistance from the sensor surface that is not present during typical sensor calibration runs *in vitro*. However, if Glut release occurs >3 μm from the sensor surface, measured concentrations are likely to be significantly lower than actual.

Simulations showing sensor responses to transient Glut as a rectangular pulse in time at specified distance from a sensor also showed great dependence of sensor response on both the relative location and duration of Glut release. If Glut concentrations are maintained for <10 ms, sensor measurements (based on calibration data previously gathered *in vitro*) are not likely to correspond to the higher actual concentration reached in the brain. As the sensor signal decays in time due to a combination of Glut diffusion away from the sensor, Glut consumption by the sensor (a minor contributing factor), and Glut uptake from the ECS, it is clear that rate constants for Glut uptake cannot be estimated straightforwardly from signal decay data. Further, as the distance between the sensor and the Glut release site was increased, the sensor signal became progressively broader and lower.

For the most biologically relevant simulations performed, in which a bolus Glut release is specified within a 20 nm region at varied distances from the sensor, it was shown that detection of Glut release within 30 μm of the sensor is feasible, and that the breadth of sensor response is related to the sensor distance from the release site. This information could be useful in distinguishing Glut release events from various locations using a single sensor if all release

events are assumed to have the same character, including magnitude and duration. However, the apparent concentrations measured using a sensor are difficult to interpret since the actual Glut concentration profile in proximity to the sensor at the time of maximum response shows very large spatiotemporal variations (quickly changing with distance from the sensor and over time).

Electroenzymatic biosensors of similar construction for other biomolecules are expected to be similarly affected by conditions *in vivo*, especially considering the key importance of H_2O_2 dynamics on sensor response reported here. Deviations from *in vitro* performance may even be more pronounced if sensors with slower enzyme kinetic rates are used, as even small differences in sensor response time were seen to theoretically have a dramatic effect on the ability of Glut sensors to monitor quickly changing concentrations.

Within the context of the available sensing techniques, miniaturization of Glut sensors will be necessary (and is feasible considering recent sensitivity improvements) if electroenzymatic sensing techniques are intended to operate with spatiotemporal resolution approaching that of electrophysiological measurements,[36] for which temporal resolution has resolved >250 Hz action potentials within ~50 μm of a three-dimensional electrode array.[37] Reaching similar levels of spatiotemporal resolution with electroenzymatic sensors would provide exciting opportunities for coordinated electrophysiological and electrochemical recording.

The current 1-D model cannot be used to determine the lateral spatial resolution of these electroenzymatic sensors. However, this 1-D model provides a foundation upon which to construct a 3-D model to further investigate spatial resolution issue and perhaps to optimize overall probe design for improved spatial resolution.

6.5 References

1. Weltin, A.; Kieninger, J.; Urban, G. A., Microfabricated, amperometric, enzyme-based biosensors for in vivo applications. *Anal Bioanal Chem* **2016,** *408* (17), 4503-4521.
2. Xiao, T. F.; Wu, F.; Hao, J.; Zhang, M. N.; Yu, P.; Mao, L. Q., In Vivo Analysis with Electrochemical Sensors and Biosensors. *Anal Chem* **2017,** *89* (1), 300-313.
3. Ou, Y. G.; Buchanan, A. M.; Witt, C. E.; Hashemi, P., Frontiers in electrochemical sensors for neurotransmitter detection: towards measuring neurotransmitters as chemical diagnostics for brain disorders. *Anal Methods-Uk* **2019,** *11* (21), 2738-2755.
4. Ganesana, M.; Lee, S. T.; Wang, Y.; Venton, B. J., Analytical Techniques in Neuroscience: Recent Advances in Imaging, Separation, and Electrochemical Methods. *Anal Chem* **2017,** *89* (1), 314-341.
5. Beamer, E.; Conte, G.; Engel, T., ATP release during seizures - A critical evaluation of the evidence. *Brain Res Bull* **2019,** *151*, 65-73.
6. Kiyatkin, E. A.; Wakabayashi, K. T., Parsing glucose entry into the brain: novel findings obtained with enzyme-based glucose biosensors. *ACS Chem Neurosci* **2015,** *6* (1), 108-16.
7. Wang, B.; Wen, X.; Cao, Y.; Huang, S.; Lam, H. A.; Liu, T. L.; Chung, P. S.; Monbouquette, H. G.; Chiou, P. Y.; Maidment, N. T., An implantable multifunctional neural microprobe for simultaneous multi-analyte sensing and chemical delivery. *Lab Chip* **2020,** *20* (8), 1390-1397.
8. Lin, M. Z.; Schnitzer, M. J., Genetically encoded indicators of neuronal activity. *Nat Neurosci* **2016,** *19* (9), 1142-1153.
9. Clark, H.; Monaghan, J.; Yang, H. R.; Xia, J. F.; Mu, M.; Lovely, A.; Micovic, N., SPARC_A DNA-based optical nanosensor for in vivo imaging of acetylcholine in the peripheral nervous system. *Faseb J* **2020,** *34*.
10. Marblestone, A. H.; Zamft, B. M.; Maguire, Y. G.; Shapiro, M. G.; Cybulski, T. R.; Glaser, J. I.; Amodei, D.; Stranges, P. B.; Kalhor, R.; Dalrymple, D. A.; Seo, D.; Alon,

E.; Maharbiz, M. M.; Carmena, J. M.; Rabaey, J. M.; Boyden, E. S.; Church, G. M.; Kording, K. P., Physical principles for scalable neural recording. *Front Comput Neurosci* **2013,** *7*, 137.

11. Marvin, J. S.; Borghuis, B. G.; Tian, L.; Cichon, J.; Harnett, M. T.; Akerboom, J.; Gordus, A.; Renninger, S. L.; Chen, T. W.; Bargmann, C. I.; Orger, M. B.; Schreiter, E. R.; Demb, J. B.; Gan, W. B.; Hires, S. A.; Looger, L. L., An optimized fluorescent probe for visualizing glutamate neurotransmission. *Nat Methods* **2013,** *10* (2), 162-170.
12. Aharoni, D.; Khakh, B. S.; Silva, A. J.; Golshani, P., All the light that we can see: a new era in miniaturized microscopy. *Nat Methods* **2019,** *16* (1), 11-13.
13. Huang, I. W.; Clay, M.; Wang, S.; Guo, Y.; Nie, J.; Monbouquette, H. G., Electroenzymatic glutamate sensing at near the theoretical performance limit. *Analyst* **2020,** *145* (7), 2602-2611.
14. Nicholson, C.; Hrabetova, S., Brain Extracellular Space: The Final Frontier of Neuroscience. *Biophys J* **2017,** *113* (10), 2133-2142.
15. Newton, A. J. H.; Wall, M. J.; Richardson, M. J. E., Modeling microelectrode biosensors: free-flow calibration can substantially underestimate tissue concentrations. *Journal of Neurophysiology* **2017,** *117* (3), 937-949.
16. Bard, A. J., and Faulkner, L. R., *Electrochemical Methods: Fundamentals and Applications*. 2nd ed. ed.; Wiley: New York, 2001.
17. Clay, M.; Monbouquette, H. G., A Detailed Model of Electroenzymatic Glutamate Biosensors To Aid in Sensor Optimization and in Applications in Vivo. *ACS Chem Neurosci* **2018,** *9* (2), 241-251.
18. Moussawi, K.; Riegel, A.; Nair, S.; Kalivas, P. W., Extracellular glutamate: functional compartments operate in different concentration ranges. *Front Syst Neurosci* **2011,** *5*, 94.

19. Antunes, F.; Cadenas, E., Estimation of H2O2 gradients across biomembranes. *Febs Lett* **2000,** *475* (2), 121-126.

20. Dringen, R.; Pawlowski, P. G.; Hirrlinger, J., Peroxide detoxification by brain cells. *J Neurosci Res* **2005,** *79* (1-2), 157-165.

21. Wagner, B. A.; Witmer, J. R.; van't Erve, T. J.; Buettner, G. R., An assay for the rate of removal of extracellular hydrogen peroxide by cells. *Redox Biol* **2013,** *1* (1), 210-217.

22. Hohnholt, M. C.; Blumrich, E. M.; Dringen, R., Multiassay analysis of the toxic potential of hydrogen peroxide on cultured neurons. *J Neurosci Res* **2015,** *93* (7), 1127-37.

23. Alexander, A. L.; Lee, J. E.; Lazar, M.; Field, A. S., Diffusion tensor imaging of the brain. *Neurotherapeutics* **2007,** *4* (3), 316-329.

24. Huang, H.; Yamamoto, A.; Hossain, M. A.; Younes, L.; Mori, S., Quantitative cortical mapping of fractional anisotropy in developing rat brains. *J Neurosci* **2008,** *28* (6), 1427-1433.

25. Wang, Y. M.; Mishra, D.; Bergman, J.; Keighron, J. D.; Skibicka, K. P.; Cans, A. S., Ultrafast Glutamate Biosensor Recordings in Brain Slices Reveal Complex Single Exocytosis Transients. *Acs Chemical Neuroscience* **2019,** *10* (3), 1744-1752.

26. Vesce, S.; Rossi, D.; Brambilla, L.; Volterra, A., Glutamate release from astrocytes in physiological conditions and in neurodegenerative disorders characterized by neuroinflammation. *Int Rev Neurobiol* **2007,** *82*, 57-71.

27. Ribrault, C.; Sekimoto, K.; Triller, A., From the stochasticity of molecular processes to the variability of synaptic transmission. *Nat Rev Neurosci* **2011,** *12* (7), 375-387.

28. Scimemi, A.; Beato, M., Determining the Neurotransmitter Concentration Profile at Active Synapses. *Mol Neurobiol* **2009,** *40* (3), 289-306.

29. Omiatek, D. M.; Dong, Y.; Heien, M. L.; Ewing, A. G., Only a Fraction of Quantal Content is Released During Exocytosis as Revealed by Electrochemical Cytometry of Secretory Vesicles. *Acs Chemical Neuroscience* **2010,** *1* (3), 234-245.

30. Wassum, K. M.; Tolosa, V. M.; Wang, J.; Walker, E.; Monbouquette, H. G.; Maidment, N. T., Silicon Wafer-Based Platinum Microelectrode Array Biosensor for Near Real-Time Measurement of Glutamate in Vivo. *Sensors (Basel)* **2008,** *8* (8), 5023-5036.

31. Malvaez, M.; Greenfield, V. Y.; Wang, A. S.; Yorita, A. M.; Feng, L. L.; Linker, K. E.; Monbouquette, H. G.; Wassum, K. M., Basolateral amygdala rapid glutamate release encodes an outcome-specific representation vital for reward-predictive cues to selectively invigorate reward-seeking actions. *Sci Rep-Uk* **2015,** *5*.

32. Hamdi, N.; Wang, J. J.; Walker, E.; Maidment, N. T.; Monbouquette, H. G., An electroenzymatic L-glutamate microbiosensor selective against dopamine. *J Electroanal Chem* **2006,** *591* (1), 33-40.

33. Jaquins-Gerstl, A.; Michael, A. C., A review of the effects of FSCV and microdialysis measurements on dopamine release in the surrounding tissue. *Analyst* **2015,** *140* (11), 3696-3708.

34. Kulagina, N. V.; Michael, A. C., Monitoring hydrogen peroxide in the extracellular space of the brain with amperometric microsensors. *Anal Chem* **2003,** *75* (18), 4875-4881.

35. Burmeister, J. J.; Davis, V. A.; Quintero, J. E.; Pomerleau, F.; Huettl, P.; Gerhardt, G. A., Glutaraldehyde Cross-Linked Glutamate Oxidase Coated Microelectrode Arrays: Selectivity and Resting Levels of Glutamate in the CNS. *Acs Chemical Neuroscience* **2013,** *4* (5), 721-728.

36. Hong, G. S.; Lieber, C. M., Novel electrode technologies for neural recordings (vol 20, pg 330, 2019). *Nat Rev Neurosci* **2019,** *20* (6), 376-376.

37. Rios, G.; Lubenov, E. V.; Chi, D.; Roukes, M. L.; Siapas, A. G., Nanofabricated Neural Probes for Dense 3-D Recordings of Brain Activity. *Nano Lett* **2016,** *16* (11), 6857-6862.

Chapter 7: Simulations of glutamate sensor performance in three spatial dimensions recommend sensor miniaturization to monitor neurotransmitter release with improved spatial resolution

Abstract

Simulations show that miniaturization of electroenzymatic sensors for neurotransmitters is necessary and feasible for glutamate (Glut) sensors and can provide resolution improvements from monitoring tens of thousands of synapses to hundreds of synapses; it is also shown that sensors can be situated much closer than 40 μm apart on sensor probes without risk of crosstalk. Ambiguity in what is detected by electroenzymatic sensors for neurotransmitters, including Glut, includes a basic uncertainty of how many synapses are being monitored and how far they can be from the probe surface to result in sensor detection. The limits on sensor packing on a probe have also seen little experimental verification lately, largely due to the lengthy process of micromachining new probe designs. Simulations are an effective tool to investigate both of these uncertainties; 3-D models of Glut sensors in the brain were constructed to simulate the performance of standard and miniaturized sensors (of various enzyme deposition schemes) in detecting both large-scale and small-scale Glut release. Simulations show sensors could be packed as tightly as is desired and miniaturized to radii of ~10 μm, with sensitivities increasing for small sensors (radii <25 μm) over that of larger sensors and showing the benefits of different enzyme deposition schemes: stamping in small areas around electrode sites *vs* dip-coating enzyme onto the larger probe surface. Simulations further show that excitation of thousands of synapses over the course of 0.5 s is likely required for Glut detection. The consistency of these results with previous experimental reports suggests a widespread applicability of this model for the interpretation of sensor data for similar sensors, including those for glucose and choline.

7.1 Introduction

Chemical signaling in the brain can be thought of as the physiological framework that guides neural function; improving our understanding of this framework is key to understanding normal and abnormal neurological processes, including the mechanisms and processes that enable plasticity and repair, disease propagation, psychological well-being, and motor or sympathetic functions. Recognition of the importance of chemical signaling has led to the development of multiple sensing techniques to monitor neurochemical transmission, generally with a focus on a specific neurochemical. Glutamate (Glut) is of particular interest as it is the primary excitatory neurotransmitter, meaning Glut dynamics can provide vital information about neuronal activity across many locations and conditions of the brain. Debate continues, however, regarding many of the fundamental aspects of Glut transmission, including how presynaptic vesicles fuse to synaptic membranes to release Glut, how much Glut is released, and how far into the brain the released Glut can travel before being removed from the extracellular space.

The most reliable, recent data available regarding Glut dynamics largely comes from two promising techniques for monitoring Glut, including fluorescent methods, which often require genetic expression of fluorescing proteins or fluorescing particle sensors along with detection scopes,[1, 2] and electroenzymatic biosensors,[3, 4] which are comparable to electrophysiological array probes[5] (although electroenzymatic sensors are currently in earlier stages of development and would still benefit from further analysis of sensor spatiotemporal resolution). Each technique is designed to be useful for specific situations, depending on the study being conducted. There are clear benefits of electroenzymatic sensing, particularly if electroenzymatic and electrophysiological sensing sites can be situated on the same probe, which would allow for combined, simultaneous electrophysiological and chemical measurements of synaptic transmission.

Electroenzymatic Glut sensors use a metal electrode (often platinum) that is held at a constant potential, relating the current produced by oxidizing chemicals at the electrode surface to a Glut concentration in the brain or surrounding solution near the sensor surface. Glut is specifically detected by immobilizing an enzyme (glutamate oxidase), which catalyzes conversion of Glut and O_2 to H_2O_2, NH_3, and α-ketoglutarate; this reaction results in a locally-produced, electrooxidizable species (H_2O_2) which can be detected at a Pt electrode. To prevent other oxidizable compounds (including ascorbate and dopamine) from obscuring the signal from Glut-mediated H_2O_2, positively and negatively charged polymer coatings (polyphenylendiamine and Nafion, respectively) are deposited between the enzyme layer and electrode surface. Sensitivities must be very high to minimize sensor size (which increases the number of sensing sites that can be incorporated on each probe and the spatial resolution) and response times must be very fast to record sub-millisecond dynamics of neurotransmitters in the brain. The best reported sensitivities and measured response times of Glut sensors are 320 nA μM^{-1} cm^{-2} and 80 ms, made on an electrode array with four 6000 μm^2 sensing sites.[4]

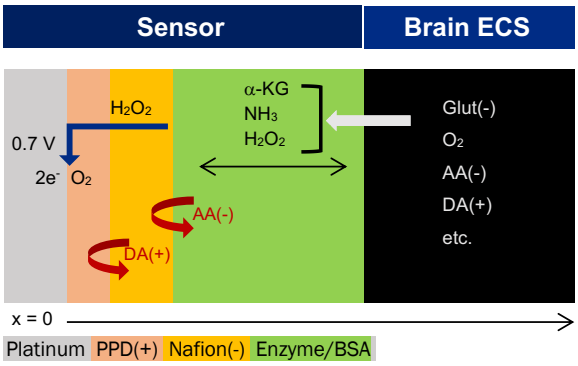

Figure 7.1. Mechanism of electroenzymatic sensing at a single sensor site. H_2O_2 is produced stoichiometrically from Glut and O_2 and releases 2 electrons when electrooxidized at a platinum surface. Ascorbate, dopamine, and other interfering compounds are excluded from the electrode surface by size and charge restrictions imposed by the polymer coatings.

In the development of electroenzymatic biosensors for neurotransmitters, sensor usage has remained largely exploratory in light of the many unknowns encountered in taking measurements *in vivo* that complicate data analysis. Some of these factors that influence Glut sensor response *in vivo* have been theoretically investigated in 1-dimensional models, concluding that the distance from the sensor to the location of Glut release fundamentally affects the nature and magnitude of sensor response and that a number of biological rates (particularly the regulation of hydrogen peroxide and cellular uptake of Glut) can further obfuscate the analysis of sensor response.[6] Ultimately this shows that direct, quantitative measurements of Glut using electroenzymatic biosensors could lead to inaccurate interpretations of sensor response if biological conditions are not accounted for properly. However, previous modeling has been of a scope that is insufficient for large-scale deconvolutions of sensor response, most notably due to its restriction to 1 dimension which makes Glut release from a single synapse (on a nm scale) difficult to model within the context of a 6000 μm^2 electrode. Further modeling can be used to begin interpreting the overlapping and complex signals that have been observed in the brain in terms of the events of Glut release that cause them; it requires modeling sensor response to numerous neurotransmitter release conditions in 3 dimensions.

In developing models to simulate sensor performance in 3 dimensions, it would be negligent to ignore the opportunity to test different probe and sensor designs, including the size and spacing of electrodes and the extent to which enzyme is coated on the outer surface of the probe. Sensing sites for electroenzymatic sensors are typically about 6000 μm^2 in size with spacings of ~40 μm, although a recent design for a glucose sensing array used much smaller sites (20 μm in diameter) with spacings of 200 μm to ensure separate sensing from each site.[7] The minimal spacing required between sensing sites has not been investigated for electroenzymatic sensors and can be clearly determined using 3-dimensional models (unless experimental noise becomes problematic). This would greatly accelerate the development of

probes with optimal sensor placement without needing to carry out the rigorous experiments to slowly increase sensor site density on a probe; such work requires modifying the complex micromachining processes required for probe design. Further consideration of whether the enzyme should be stamped or electrochemically entrapped only onto specific sensing sites or whether it is better to fully coat a probe in immobilized enzyme will also be helpful in guiding further sensor design and in analyzing the response of sensors produced with different enzyme deposition schemes.

In this work, an analysis of sensor performance in response to large-scale and small-scale neurotransmitter release is presented (additionally examining the effects of different enzyme deposition schemes and electrode sizes for Glut sensors), along with a method to determine the minimum spacing requirements for sensor sites on electrode array probes. It is the intent of this work to provide an initial theoretical framework for interpreting the magnitude of sensor response over time in terms of the number of vesicles releasing neurotransmitters and their location relative to the sensor surface.

7.2. Methods

7.2.1 Mathematical model of diffusion and reactions in the brain and sensor coatings

A three-dimensional mathematical model in cartesian coordinates was developed with time-dependent partial differential equations in the form of Equations 7.1 and 7.2, representing the chemical processes and diffusion within the sensor coatings and the brain extracellular space (ECS), respectively. These equations and the relevant parameter values remain the same as reported in Chapters 3 (for the sensor) and 6 (for the brain ECS), and diffusive transport parameters follow from those reported previously.[8] In these models, concentration variables refer to the number of moles per volume of ECS, while the overall terms in the equations represent the change in moles per second within the entire tissue domain. The different volumes used necessitate the inclusion of void fractions in some of the terms so that

the volumes considered in each term remains consistent. Within the sensor, effective diffusivities are used (modifying the molecular diffusivity in water D_i by the constants α_j) and in the ECS, diffusion is modified by the tortuosity (λ = 1.6) and void fraction (ε = 0.2) as previously reported.[8] The rate terms r_i are used to describe enzymatic turnover of Glut (within the enzyme domain) and the uptake and clearance of Glut and H_2O_2 in the ECS. No void fraction term is needed for the enzyme rate since the rate equation uses the enzyme concentration, which is on the total volume of the immobilized enzyme layer.

$$\epsilon_b \frac{\delta C_i}{\delta t} = \frac{\epsilon_b}{\lambda^2} D_i \nabla^2 C_i + \epsilon_b r_i(C_i) \tag{7.1}$$

$$\epsilon_j \frac{\delta C_i}{\delta t} = \alpha_j D_i \nabla^2 C_i + r_i(C_i) \tag{7.2}$$

i = Glut, H_2O_2, O_2; j = PPD, Nafion, enzyme; b = brain ECS

Rates for the uptake and clearance of Glut and H_2O_2 in the ECS are assumed to follow first-order kinetics, as was done in Chapter 6. Due to uncertainties in appropriate rate constants to be used, partly due to the non-isotropic nature of the brain, a range of constants was used for each species. Actual average rate constants within the brain are expected to be described within these limits. Fluorescence data using genetically modified fluorescing proteins in the brain (that bind to Glut) were used to estimate Glut uptake rate constants, and a combination of crosstalk simulations and experimental data was used to select H_2O_2 clearance rate constants (as described in greater depth in Chapter 6). The first-order rate constants for Glut are assumed to fall within the range of 4.33, 4.95, and 7.7 s^{-1} with associated H_2O_2 clearance rate constants of 0.0116, 5, and 30 s^{-1}. Oxygen concentration was regulated such that it would not influence the simulation results, which is a reasonable assumption based on the previous observations

from *in vitro* simulations that O_2 is not limiting unless the concentration of Glut is held constant at a concentration more than triple that of O_2.[6] Since the concentration of O_2 in the brain ranges from 5-50 μM, similar to that expected for Glut,[9] simplifications to ignore oxygen dependency are not expected to influence simulation results.

In all simulations, equal diffusive fluxes were applied at all boundaries between sensor layers with a zero flux condition at the sensor's silicon boundaries and at the deeper regions of the ECS. Platinum electrooxidation of H_2O_2 was specified with a detailed rate equation at the electrode surface equal to the flux at the electrode surface. Current response was calculated by integrating the electrode reaction rate over the surface of the sensor, and compared to 1-D results for the same Glut concentration at the sensor edge to ensure consistency between the two models. Initial conditions specified zero concentrations everywhere for Glut and H_2O_2 and 25 μM for O_2 in all regions. A different initial condition was specified for a single bolus release of Glut (see 7.2.3). The geometries and meshing used are shown in Fig. 7.2. A small region (1-3 μm) near the sensor is separately modeled with no uptake or clearance, representing a volume of space disrupted by sensor insertion in which normal biological functions are not active.

7.2.2 Modeling large-scale neurotransmitter release

To model large-scale Glut release, a domain in the brain was specified with its bottom edge 3 μm from the probe surface (directly above the disrupted ECS region). In this large region >3 μm from the probe surface, where active neurons would be present, Glut release was specified assuming there is an even distribution of synapses releasing Glut at the rate of a given firing pattern. This assumes that with enough sources of Glut release near the sensor at varied distances, the overall Glut level detected by the sensor would be an average of these individual signals. This can be input into the model as a source function (analogous to a reaction rate term that continually produces Glut), specifying an increase in concentration over time. This value can be calculated from the firing rate by assuming a density of glutamatergic synapses of 0.9 ×

7×10^8 synapses/mm^3 as might be expected in the rat neocortex[10] (assuming 90% are glutamatergic) and that each time a synapse fires it releases one vesicle's payload of Glut (~3640 molecules).[11] Cans *et al*. recently have estimated larger quantities in vesicles,[12] although it is commonly thought that not all of the neurotransmitters escape a vesicle when it releases its contents, so the original estimation of 3640 molecules was used.

If a baseline firing pattern produces a tonic level of Glut, the sensor would record this Glut concentration as its baseline. To simplify model initial conditions, the initial concentration of Glut was set to 0 to represent this baseline rate. For levels of increased activity, an increase in firing rate of 10 Hz results in an increase in Glut production of 38.1 μM/s throughout the specified domain (the firing rate of pyramidal neurons has been observed to change by 5-10 Hz at times of increased activity). Since the dendritic tree of a pyramidal neuron is ~100 μm in characteristic length, modeling increases in neuronal activity on this scale is reasonable. By specifying Glut release this way, we can roughly estimate sensor response to a large region of glutamatergic release, using the difference between high and low average firing rates to simulate a change that might be observed *in vivo*. Increased firing was specified for periods of 1 s, recognizing that many electroenzymatic sensors have reported response times of ~1 s and that large-scale, stimulated releases of Glut in the brain could easily last for this time period and result in the responses that have been observed experimentally.

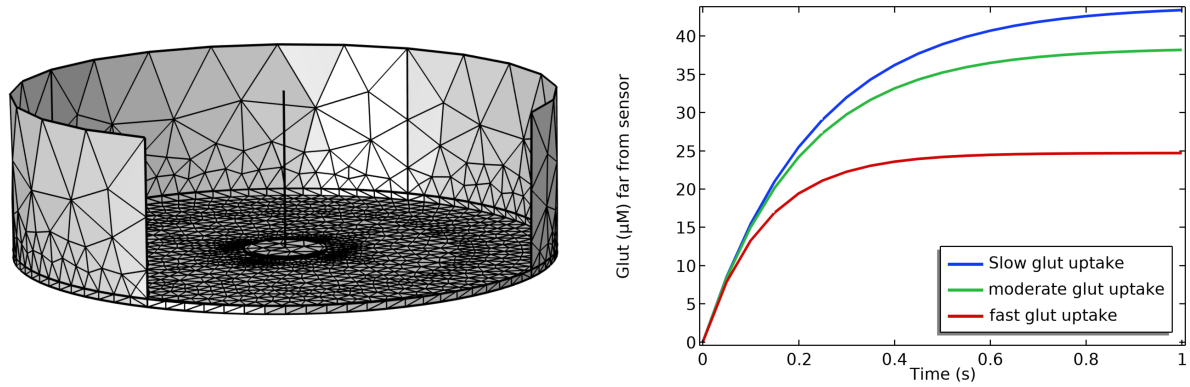

Figure 7.2. Overall geometry and mesh used in single-site, 3-D calculations. The Glut concentrations shown over time (at a distance where the sensor does not affect results) is shown on the right for averaged, large-scale Glut release at a frequency of 10 Hz above baseline firing frequencies: final Glut concentrations are 24.7 μM, 38.2 μM, or 43.4 μM for different rates of glut uptake.

7.2.3 Modeling Glut release from a single synaptic vesicle

Release from a single synaptic vesicle was modeled as an initial condition for solving the sets of partial differential equations, specifying that inside a synaptic volume (2.87×10^{-5} μm^3) a vesicle-sized number of Glut molecules (~3640) is present the extracellular space, after which it is free to diffuse and react as defined by the governing equations (effective diffusivity and reaction rates are assumed to be the same in this region as specified for the rest of the ECS, where volume-averaged rates describe reactions and effective diffusivities.

The large difference between vesicle size and electrode surface resulted in poorly meshed domains or too many volume elements for reasonable calculation times and memory usage. To improve the meshing, an isolated system was modeled for a few tenths of a millisecond and repeated for three possible Glut uptake rates. The average concentration after 3-4 ms within a 1 μm sphere was ultimately used as the initial condition for bolus release models. Before incorporation into the model, the accuracy of this simplification was determined by monitoring the concentrations at 1 and 2 μm from the release site for both the simplified model (initial concentration specified in 1 μm radius sphere) and the initial system (initial

concentration specified in 19 nm radius sphere). Concentrations at 1 or 2 μm from the center of release of the simplified (larger) system conformed to within 90% of the actual system within <1 ms, showing this simplification is suitable. Since varying the location of the bolus Glut release changes the meshing, initial concentrations were integrated over the ECS volume and modified to ensure the same number of molecules were being released in each simulation regardless of meshing.

7.2.4 Modeling Glut release from clusters of neurons at an increased firing frequency for a brief time period

For modeling an increase in the firing rate of a specific number of neighboring glutamatergic neurons, the same release function described in 7.2.2 was applied within a volume of space related to the number of excited neurons being modeled. The volume necessary was calculated based on the average density of glutamatergic synapses in the rat neocortex (6.3×10^8 synapses/mm^3),[10] assuming 90% of the synapses are glutamatergic. The volume was specified as a cylinder with a height, h (= r/2), located with its lower, circular side parallel to the sensor at varied distances from the enzyme layer. Dimensions for the number of synapses used are provided in Table 1, along with the maximum Glut concentrations within this volume resulting from 0.5 s of a 10 Hz increase in firing frequency.

7.2.5 Numerical solutions

Solutions were generated using COMSOL Multiphysics (COMSOL Inc., Los Angeles), with coefficient form PDEs as governing equations being solved by time-dependent solvers. Parametric sweeps were specified in the solver inputs to compare changing variables. The large number of specified PDEs required use of the fully coupled solver. Time steps were reduced along with variable tolerances until smooth solutions were found. Meshing (see Fig 7.2) was built from the domains with the highest aspect ratios first; for the sensor coatings, the electrode

surface was meshed first and extended vertically using a swept mesh of 3 layers. Since parameter sweeps require re-meshing, some mesh modifications were made manually for large enzyme overlap models; in these cases, a free tetrahedral mesh produced good results.

7.3 Results:

7.3.1 Response of sensors with varied sizes and enzyme coverages to large-scale Glut release

Since the scale of Glut release required for electroenzymatic detection is currently unclear, it is logical to begin by modeling the sensors within the context of the most Glut a sensor could be expected to encounter, and compare sensor designs in detecting Glut under these conditions. Within the context of large-scale Glut release where the firing rates of all nearby glutamatergic neurons increases from 0 to 10 Hz for 1 s, sensor response was simulated for sensors of 5, 10, and 25 μm radii and for 40 × 150 μm sensors with different extents of enzyme coverage (overlap), with basic model parameters as defined in Fig. 7.3. After 1 s of increased firing rates, Glut concentrations rise to the values shown in Figure 7.2 in the deeper spaces of the brain where there is no sensor influence and no diffusive dissipation since such a large region is releasing Glut. The range of values shown results from different first-order Glut uptake rate constants, as measured by fluorescence imaging and as used in previous, 1-D simulations (see section 7.2.1).

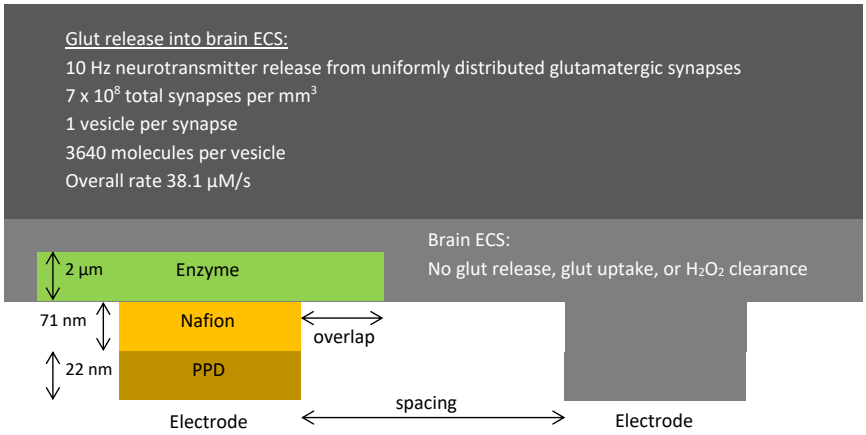

Fig 7.3. Method for testing effects of enzyme overlap (for enzyme stamping) and analysis of spacing requirements to prevent crosstalk. Simulations used both circular and rectangular electrode shapes.

As could be expected, increased immobilized enzyme layer overlap of the surrounding probe surface results in an increase in Glut consumption and H_2O_2 production, leading to higher concentrations of H_2O_2 in the sensor coatings and surrounding brain extracellular space (Figure 7.4), which also means an increased sensor response. For different overlap lengths (after 1 s of increased stimulation), the maximum H_2O_2 concentration within the enzyme coating can vary from 7 to 9 µM at the middle of the sensor and from 12.5 to 24 µM in the middle of the overlap region, depending on the overlap and not on the sensor's electrode size. Along the centerline, Glut concentrations reach 90% of the maximum bulk value at distances of 22.45 and 22.8 µm from the electrode surface (depending on the overlap), indicating that a sensor site could influence local Glut concentrations under these release conditions within ~20 µm; this could be an important value in determining the optimal sensor spacing on a probe, although it will depend on the local rate of Glut uptake in the brain. By stamping enzyme only over the electrode, response will be reduced due to the lower amount of H_2O_2 generated but the sensor will have a minimized effect on the surrounding tissue.

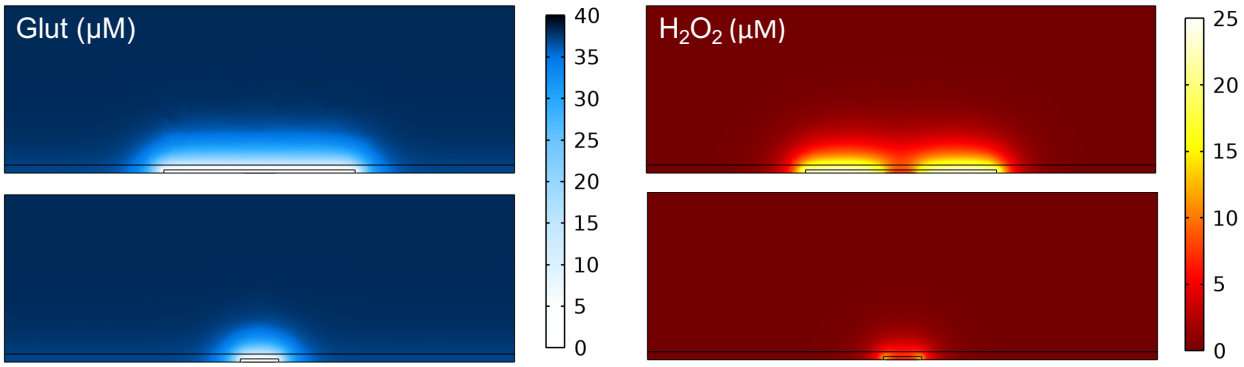

Figure 7.4. Cross-sectional concentration profiles of Glut and H_2O_2 at the center of the cylindrical domain after 1 s of 10 Hz increased neuron firing frequency. Above, results are for 50 μm of overlap; below are the profiles resulting from 2 μm of overlap.

Sensor response for various electrode sizes and overlap distances was found by integrating over the electrode surface in each case, and the resulting responses over time are shown in Figure 7.5. Possible variations in response due to differences in Glut and H_2O_2 clearance or uptake rates (shown by the error bars) are seen to be roughly consistent on a log scale. The biological factors of Glut and H_2O_2 clearance or uptake, which retain an unknown level of uncertainty, are shown to potentially have a larger effect on sensor response than the amount of enzyme overlap. Yet as expected, the increased production of H_2O_2 observed with greater overlap does lead to an increased sensor response. For the smallest sensor size (5 μm radius) sensor response with the 50 μm overlap was 1.225 times that of the 2 μm overlap. Similar trends are evident in all sensor sizes, with sensor response generally following a linear relationship with electrode area. Noticeable positive deviations from linearity are present for all three circular sensors, which is expected since their characteristic dimensions drop below ~25 μm.[13] For example, 5 μm radius sensors with 2 μm of enzyme overlap record a response of 8.15 pA while the linear trend would predict 3.97 pA.

Normally a calibration factor is used to relate sensor response to a bulk Glut concentration. Calibration factors used here are based on simulations of the same 40 × 150 μm

sensors *in vitro*, for highly optimized Glut sensors with a sensitivity of 364.2 nA μM^{-1} cm^{-2} (in agreement with observed sensitivities of 320 ± 19.6 nA μM^{-1} cm^{-2}).[4] Since this conversion factor is determined *in vitro*, where stirring results in rapid convective mass transfer that clears H_2O_2 away from the sensor (and reduces the possible sensor response), it is not necessarily an accurate conversion for sensor response *in vivo*, where μM concentrations of H_2O_2 can accumulate due to a lack of convective clearance (this buildup effectively boosts sensor response, as shown in Chapter 6). For the rectangular 40 × 150 μm sensors of Figure 5, the simulated calibration factor is 21.8 pA/μM, and for the circular sensors off radii 5, 10, and 25 μm the calibration factors are 0.286, 1.24, and 7.15 pA/μM, respectively (all use the same sensitivity of 364.2 nA μM^{-1} cm^{-2}). This calculation is made assuming that during a calibration *in vitro* (with high external mass transfer) all sensors will have the sensitivities of the macro-sized 40 × 150 μm sensor; smaller sensors would not benefit from increased diffusive flux due to 3-D transport from this calculation since mass transfer to the larger sensor is described by 1-D transport. This may help small sensors appear to perform better *in vivo*, should they be developed and used.

Applying the simulated *in vitro* calibration factor to the linear regime of the simulation data (for moderate uptake and clearance rates) gives concentrations that would be measured when the enzyme overlap is 2 or 50 μm: 13.81 and 15.16 μM, respectively. These “measured” concentrations are much lower than the actual bulk concentration that is reached far from the sensor (38.2 μM), although the measured values exactly match the concentrations at distances of 6.2 and 6.8 μm from the electrode surface along the sensor’s centerline. These values are directly dependent on the conditions of Glut release and are expected to vary for actual neuron and synapse firing frequencies and spatial distributions. Since these concentrations and distances use moderate rates of Glut and H_2O_2 clearance or uptake, differences and inconsistencies in rates may also affect these results.

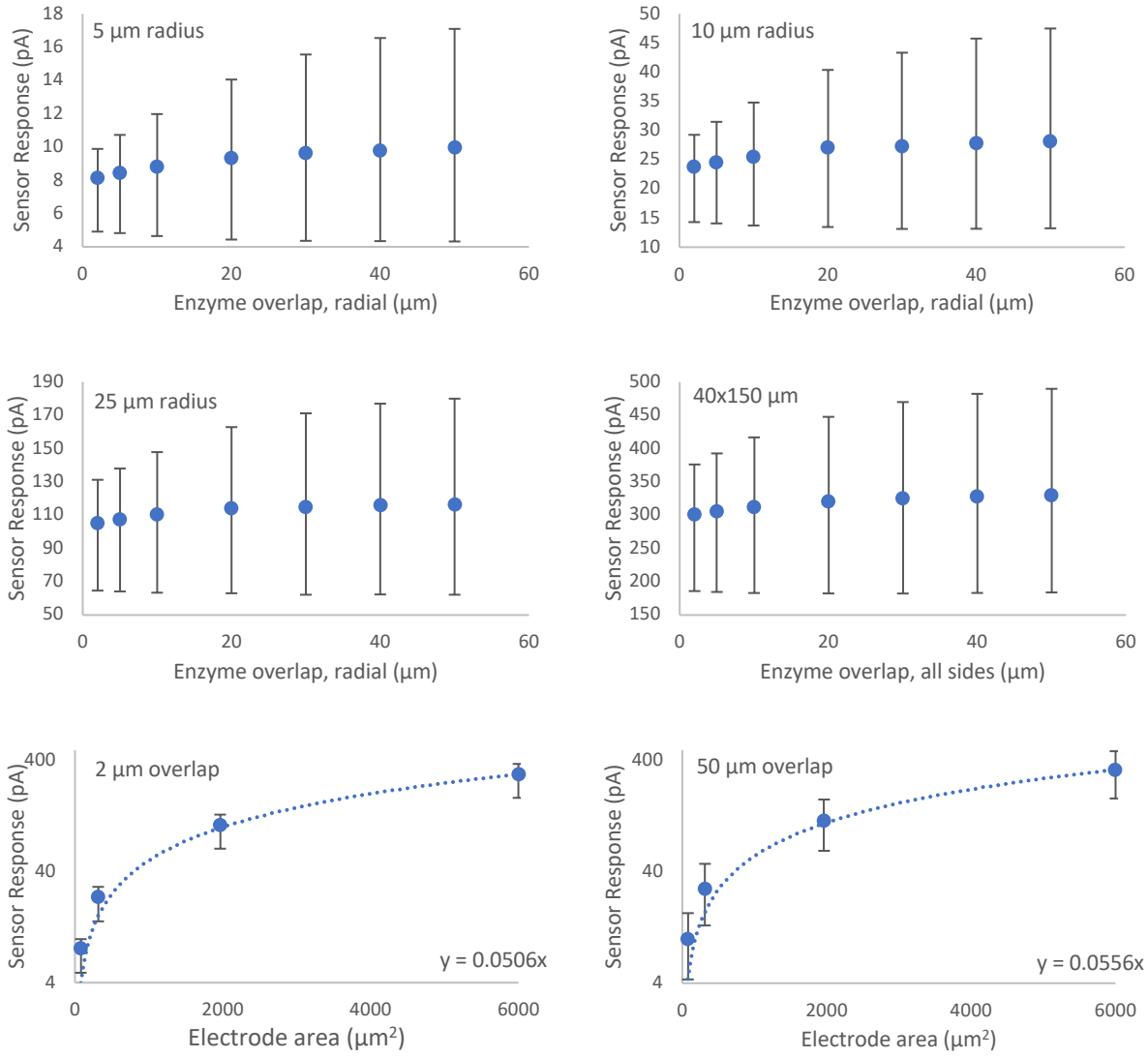

Figure 7.5. Sensor responses to large-scale Glut release for varied sensor sizes and enzyme overlap lengths. Error bars show dependence on Glut and H_2O_2 uptake and clearance rates, where larger response corresponds to slower uptake and clearance. Plots of response *vs* electrode area are drawn on a log scale to improve clarity; equations for linear fits are given.

7.3.2 Determination of minimum spacing distances for detecting large-scale Glut release

To determine minimum spacing distances between sensor sites, a set of simulations were performed with 2 sensor sites of various spacing distances and electrode radii of 10 or 20 µm (enzyme overlap was set to 2 µm). The same large-scale Glut release used for the

simulations in section 3.1 were used. Initially, the second site was given the same permselective films and diffusive resistance of an immobilized enzyme layer (the second enzyme layer was given no reaction term, representing an enzyme for a different substrate such as choline).[4] Even for a minimal spacing distance of 3 μm (a spacing of 2 μm would result in enzyme layers in contact with each other) the response of the second sensor was < 10^{-30} pA (for both 10 and 20 μm radii), meaning it is not likely for there to be any noticeable crosstalk between fully modified electroenzymatic sensor sites no matter how closely they are spaced, even if electrodes are miniaturized to 20 μm diameters. Sensors with less mass transfer resistance within the sensor coating can be shown to be more sensitive to neighboring sensor sites.

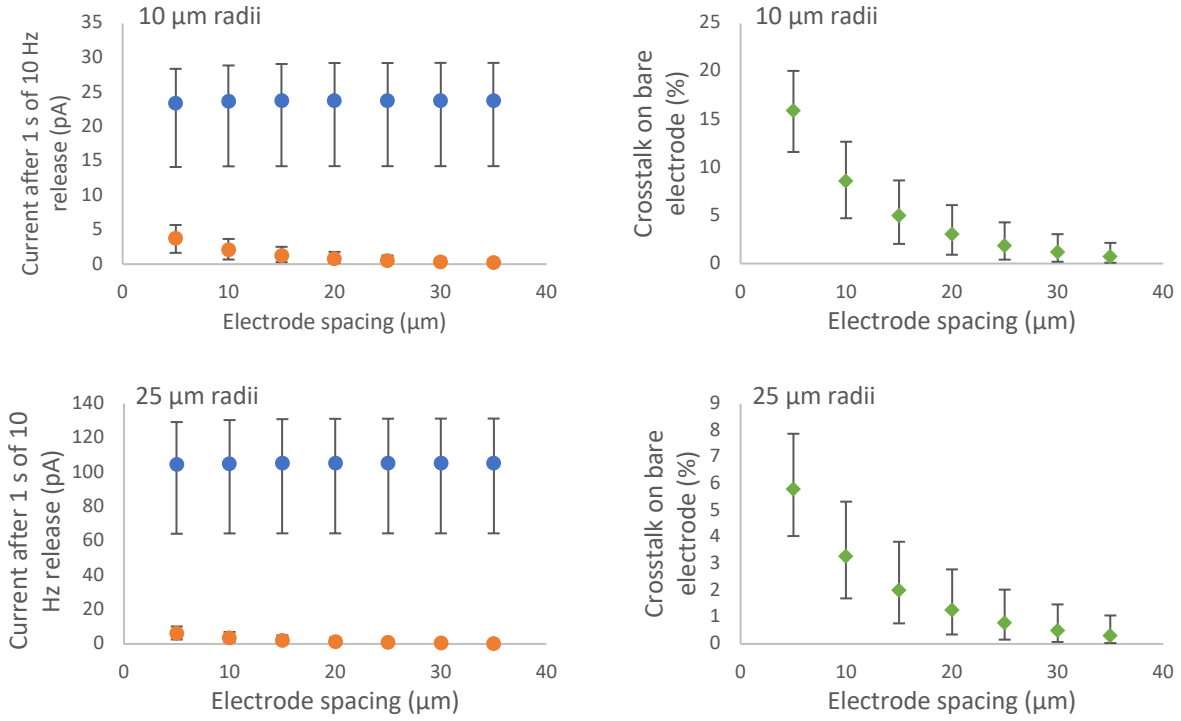

Fig 7.6. Crosstalk with bare electrode: on the left, response of the fully coated sensor site (blue circles) is plotted with the response at a bare, neighboring site (orange circles). The ratio of the bare site response relative to the fully coated site response is shown on the right (green diamonds). Error bars represent possible variations in Glut and H_2O_2 uptake or clearance rates.

A similar set of simulations were performed for a bare secondary site, representing cases where an on-probe reference electrode is used (see Fig. 7.2 for a model diagram).[14] If the reference electrode is affected by the H_2O_2 produced by the neighboring electroenzymatic sensor, there will be interference and the overall sensor response will likely be reduced. Simulations to investigate this possibility and elucidate what spacing distances would be safe for such sensor designs led to the plots of electroenzymatic sensor response and bare sensor response in Figure 7.6. Since the magnitude of the bare sensor responses remain below ~5 or ~10 pA for 10 and 20 μm radius sensors, the bare sensor response was also plotted relative to the Glut sensor response. These results show that the relative magnitude (thus the significance) of the neighboring bare site's response is a function of both electrode size and sensor spacing. For an array where multiple neighboring sites are present, crosstalk increases proportionately. Error bars again represent possible variations in Glut and H_2O_2 uptake or clearance rates, where faster rates lead to lower sensor response.

7.3.3 Sensor response to bolus Glut release from a single vesicle

For sensor responses to be related to specific Glut release events, it may be helpful to consider sensor response to a single vesicle releasing its neurotransmitter contents into the ECS, even though it is highly unlikely that such a small release of Glut would be observed. It is predictable that response (and measured concentrations) will be affected by the size of the electrode used and the amount of enzyme coverage on the sensor site. However, under these conditions (see section 7.2.3), such little Glut is released that simulations showed there is no difference in sensor response for enzyme coverages of 2 μm and 50 μm for any sensor size considered. To compare the performance of electroenzymatic sensors of standard minimum dimensions (40 μm wide ~50 μm diameter)[4] with a much further miniaturized sensor, simulations were performed of sensors of 5 μm and 25 μm radii responding to a single vesicle release of Glut (~3640 molecules) into the ECS. For any release distances simulated the

response was extremely small (femto amps) and would not be observable without an unprecedented reduction in noise. In both of these cases, the larger sensor showed little improvement in overall current generated, with both recording ~ 10 fA. However, if an apparent concentration is calculated (as in section 7.3.1) from the fA response using *in vitro* calibration factors, the smaller sensor showed a much higher measurement, although the value remained indistinguishable (on the order of nano molar). The shape of the response is characteristic of observed sensor responses, with rise times of ~5-10 ms and decays ~4× as long as the rise time. However, it is clear that many releases in close proximity to the sensor will be required for detection, for any sensor that is used.

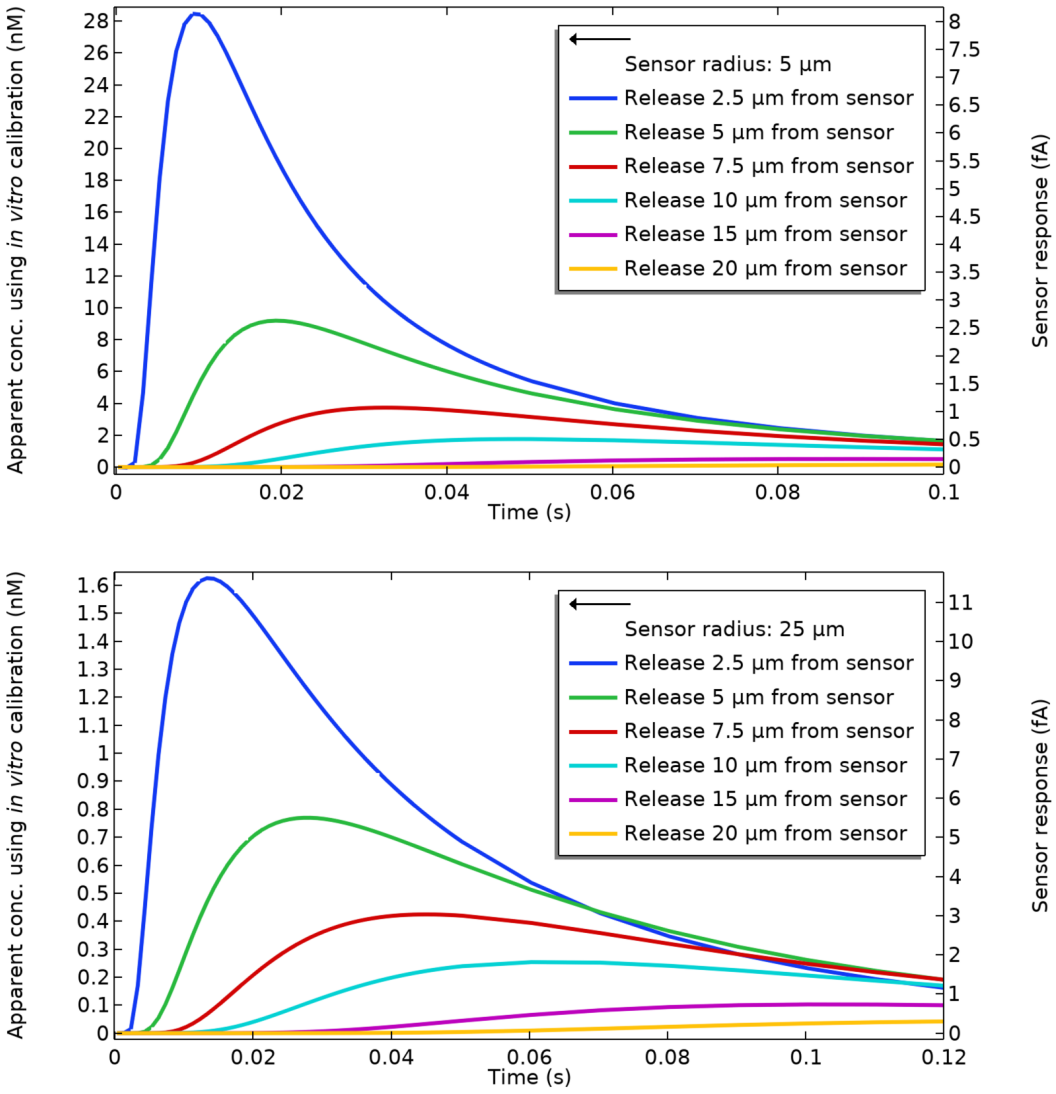

Fig 7.7. Simulated sensor response to a single vesicle bolus release at varied distances. Apparent concentrations are calculated using an *in vitro* calibration sensitivity of 364.2 nA/µM/cm^2, determined from *in vitro* simulations,[4] corresponding to calibration factors of 0.286 and 7.15 pA/µM for sensor radii of 5 and 25 µm, respectively.

7.3.4 Sensor response to Glut released from clusters of synapses with a 10 Hz increase in firing rate for 0.5 s

The maximum sensor response to a single vesicle releasing Glut, even for release directly above a sensor with a 5 µm radius, is over 2 orders of magnitude too low to be detected

(assuming the 0.7 μM detection limit that has been observed for larger sensors is maintained, which may overestimate the detection limit in this case).[4] Simulating release >2 orders of magnitude higher requires consideration of many synapses, which would occupy a relatively large volume of space compared to the sensor and would result in overlapping signals (even if all releases occur at the same point in time, which is not realistic). For this reason, sensor response to releases from a cluster of synapses was modeled as a constant source of Glut over time within the appropriate volume of space (see 7.2.4). A “hockey puck” shape was chosen as the release region to roughly optimize the amount of Glut detected and maintain the specified distance between the puck and the enzyme layer, no matter how large the puck was (*i.e.*, how many synapses were modeled to have an increased firing rate). Simulations were performed using varied puck sizes, or numbers of excited synapses, for two sensor sizes, with 5 and 25 μm radii, to represent a highly miniaturized sensor and one similar to existing electroenzymatic glucose sensors[7] (or the smaller dimension of existing rectangular Glut sensors). The dimensions of the puck regions and synapse numbers are provided in Table 7.1. The table also lists the change in Glut concentration from baseline levels at the center of the puck that would result from the same synapses firing at 10 Hz increased frequency for 0.5 s without any sensor present. Variations shown for each puck size depend on the rate of Glut uptake modeled in the brain. In comparing the puck maximum concentrations to the results of Fig. 2 (24.7 μM, 38.2 μM, or 43.4 μM for different uptake rates), the concentrations reached within the puck regions are noticeably lower.

Table 7.1. Dimensions and number of synapses for the specified “puck” regions of increased glutamatergic synapse firing frequency, as well as the maximum concentrations reached within the puck after 0.5 s of firing at a rate increased by 10 Hz from baseline values (in an isolated brain region with no sensor consumption or influence). Concentrations reached depend on the local rate of Glut uptake, modeled as a range of predicted values.

Number of Synapses	Diameter (μm)	Height (μm)	Max Glut after 0.5 s, 10 Hz (μM)		
			4.33 s^{-1}	4.95 s^{-1}	7.7 s^{-1}
50	7.4	1.8	1.15	1.14	1.08
150	10.7	2.7	2.22	2.17	2.02
350	14.1	3.5	3.54	3.45	3.14
1,000	20.1	5.0	6.09	5.89	5.17
2,500	27.2	6.8	9.33	8.94	7.59
5,000	34.3	8.6	12.5	11.8	9.75
10,000	43.2	10.8	16.1	15.1	12.1
20,000	54.5	13.6	19.9	18.7	14.5
50,000	73.9	18.5	25.1	23.3	17.5
75,000	84.6	21.2	27.3	25.2	18.7
100,000	93.2	23.3	28.6	26.3	19.3

The responses of a 5 μm radius sensor and a 25 μm radius sensor to puck-shaped regions of increased glutamatergic synapse firing frequency are shown in Fig 7.8 and naturally depend on both the number of synapses modeled with increased firing rates as well as the distance of these synapses from the enzyme surface. Three distances, 1 μm, 5 μm, and 10 μm were simulated, where the first μm of this distance is considered as damaged tissue where molecules have the same diffusivities as in the rest of the brain but no uptake or clearance of Glut or H_2O_2 occurs (see section 7.2.1). Solid lines represent moderate rates of Glut uptake and H_2O_2 clearance and dashed lines represent slow or fast rates, as explained in section 7.2.1, where fast rates result in lower sensor response and slow rates result in higher sensor response. In the legends of each plot, the concentration provided is the value for an isolated puck of the same dimensions and rates corresponding to moderate Glut uptake.

The numbers of synapses used were chosen to result in puck sizes similar to the sensor, larger than the sensor, and much larger (with sensor response to larger amounts of excited synapses shown for release at greater distances). For releases as close as possible to the sensor (1 μm is the minimum distance due to the “damaged tissue” region) the apparent concentrations measured can approach the actual concentrations reached within the puck if the puck diameter is greater than the sensor’s (7.8A for >1,000 synapses), although this is not replicated for the larger sensor (7.8B) since the maximum concentration reached within the puck is also a function of the puck height and the larger diameter results in a taller puck. The

variations in these two results highlights an important difference between sensors of different radii: a sensor with a larger radius will not record apparent Glut measurements at observable magnitudes unless much larger regions of nearby brain tissue display increased firing frequencies for a significant period of time, and if a large region is stimulated (above its normal firing frequency) it is likely that a significant part will be farther from the sensor. Regions of increased neurological activity of lower aspect ratios or that are not ideally oriented around the sensor will result in actual concentrations much higher in the brain than a sensor would measure. Ultimately, it is evident that use of calibration factors can be misleading in large sensors in a way that is not evident in smaller sensors.

Although the sensor's current response is a much better indicator of nearby Glut release, it would be difficult to associate a response amplitude with an actual Glut concentration without detailed simulations as performed here, which rely on simplifications that limit their accuracy (see the large number of overlapping lines, particularly the dotted lines in Fig. 7.8C and 7.8E-F, resulting from the assumptions and simplifications used in describing the uptake and clearance of Glut and H_2O_2). Measuring with small sensors and calibration factors appears to be the better approach for measuring the concentration changes specified, assuming that noise does not obscure the responses. If noise is problematic, as it likely is, the larger sensors show a clear advantage in recording response from the same conditions of neurotransmitter release: the 25 μm radius sensor records ~85 pA response to 2,500 synapses while the 5 μm sensor records ~2.5 pA (solid purple lines in 7.8A and 7.8D), and similar trends are shown in the black lines (10,000 synapse) in Fig 7.8C and 7.8F for releases 10 μm from the sensor.

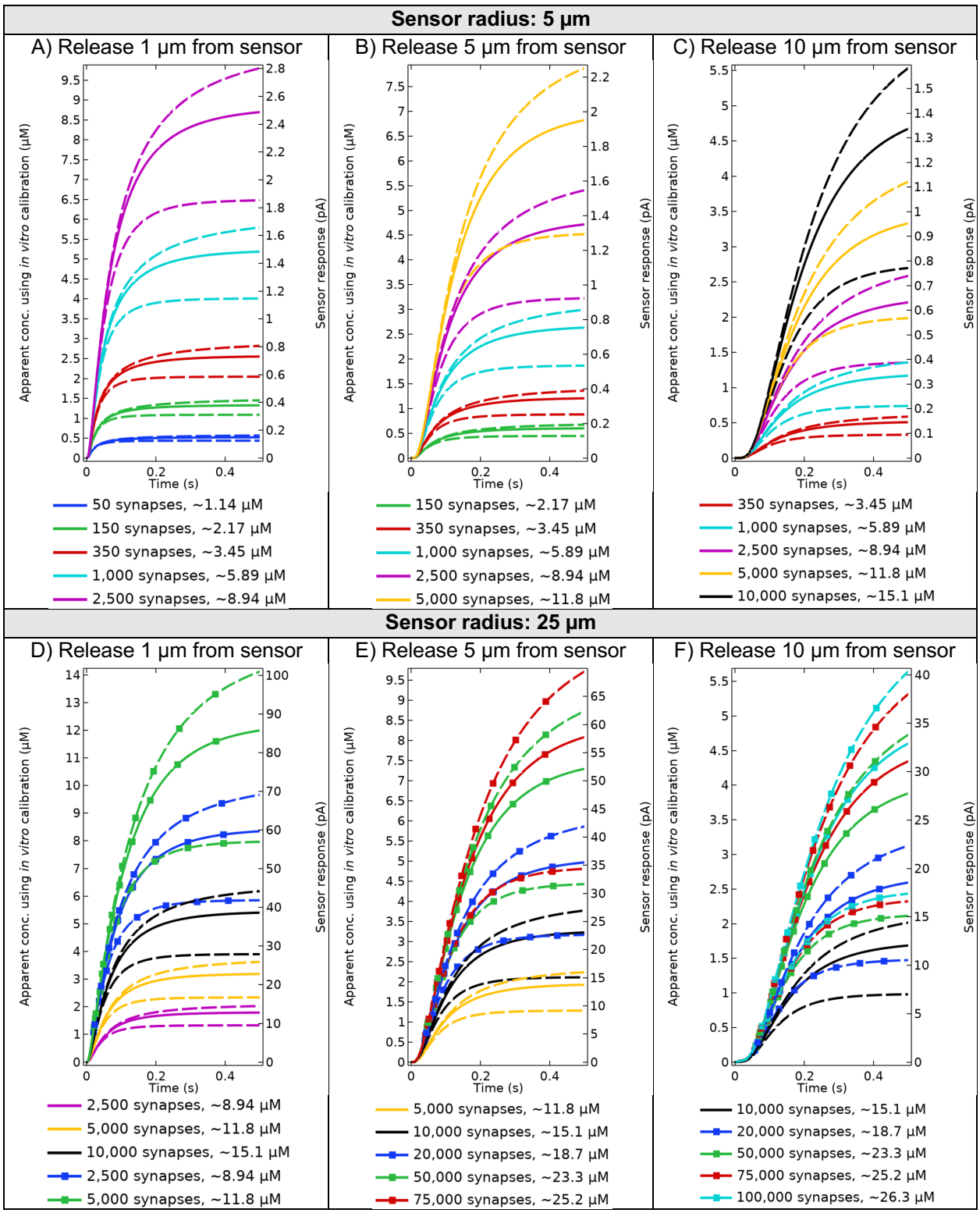

Figure 7.8. Sensor response to 10 Hz increase in glutamatergic synapse firing frequency within puck-shaped regions (depending on the number of synapses and average synapse density) containing various numbers of synapses at distances of 1, 5 and 10 µm from the sensor's enzyme surface. Dashed lines

show fast (lower sensor response) and slow (higher sensor response) rates of Glut and H_2O_2 uptake and clearance. Concentrations given in the legends are for moderate uptake rates in simulations with no sensor. Calibration factors used for calculating the apparent Glut concentrations were 0.286 and 7.15 pA/μM for 5 μm and 25 μm sensors, as discussed in 7.3.1.

7.4 Discussion

Results from the simulations of a large-scale, 10 Hz increase in glutamatergic synapse firing frequency for 1 s show that Glut levels will reach ~38.2 μM in the brain and H_2O_2 can reach ~25 μM within large enzyme overlap regions of the sensor. These Glut concentrations are higher than is often measured, which might initially suggest that the 10 Hz increase in firing rate is a bad model for Glut release. However, when the *in vitro* calibration factor is used to translate the pA response of the sensor to a concentration measurement, reasonable values of 13-15 μM are found. This suggests that although experimental measurements of Glut concentrations using electroenzymatic sensors may record concentrations on the order of 10 μM, it is reasonable to assume that concentrations may reach 2-3 times that value farther from the sensor and that this could be caused by a large-scale increase in the glutamatergic synapse firing frequency on the order of 10 Hz. Recent Glut measurements taken in rats during periods of addictive behavior[15] were able to record concentration changes on the magnitude of simulated 10 Hz firing rate increases, with experimental measurements of up to ~40 μM with sensor responses of ~50-200 pA (noise of < ~20 pA). This experimental observation lends credence to the accuracy of these simulations and may justify a significant miniaturization of Glut sensing sites due to the relatively low noise produced.

It is interesting to note that the Glut concentration reached within a small region of the brain due to an increase in firing frequency is largely determined by the size of the stimulated region. Miniaturized, closely packed sensors would be much more capable for making conclusions in cases of small-scale Glut release since their calibration factors are representative

of a smaller quantity of molecules and since increases in sensitivity are observed for sensors below ~25 μm in radius due to diffusion in 3 dimensions. Smaller sensors will also respond equally well to large-scale Glut release (noise permitting), and their smaller footprint allows for more precise determinations of the volume of space experiencing excited firing if more sites are positioned on each probe.

The low simulated crosstalk calculated between sensor sites is very promising for choosing electrode spacings in that it indicates that realistic conditions may allow for even more tightly packed sensor sites in an array. However, the ~20 μm distance in which a sensor affects the Glut concentration (see Figure 7.4) seems to suggest that a larger spacing is needed for similarly modified sensing site neighbors. In considering this effect that a sensor site has on local Glut, it is helpful to realize that the presence of similar neighboring sites will result in a larger enzyme coverage on the sensor probe; any loss in local Glut concentration due to a neighboring site is likely to be mitigated into insignificance by the H_2O_2 produced by it. Noise permitting, miniaturization and close packing is feasible considering that the risk of potential crosstalk between sensor sites obscuring results is minimal.

Ultimately, it is most interesting to compare electroenzymatic sensors with competing technologies including fluorescence detection, which can boast a very useful field of view and spatiotemporal resolution.[2, 16] Fluorescence detection is limited by light absorption and scattering, but appears to be a useful technique in many future applications once multi-photon techniques circumvent a power dissipation problem for large-scale, deep-brain imaging or other methods are developed to resolve fluorescing signals above background light scattering.[16] Electroenzymatic sensors have room for improvement as well, although these modeling results bring some very useful information into consideration: these sensors do a very good job of monitoring for large-scale increases in glutamatergic activity over a relatively large number of synapses (possibly up to 100,000 as shown in Fig 7.1F) within a fairly short distance from the sensor surface. This range of sensing makes the technique less affected by background

signals, which are known to require special treatment in fluorescence imaging including dual-photon systems and miniscope devices.[17]

The results presented from these simulations are perhaps most intriguing within the context of more recent probe designs, including the recent development of silicon/PDMS probe arrays with 4 sensing sites (one as an on-probe reference electrode to reduce noise and insertion damage) and a microfluidic channel used to deliver fluids for calibrations *in vivo* or drug delivery.[12] Applying 3-D models to the data collected from these studies provides an opportunity to precisely test the diffusion and reaction rates in the probe vicinity for multiple relevant neurochemicals, including Glut and H_2O_2. Preliminary results reported from these sensors, designed for glucose detection, showed that sensor response to sustained injections of 4 mM glucose (at 20 psi) showed a maximum response for injections sustained for more that 1.2 s. It can be assumed that after this time, glucose concentrations reach a steady state in the sensor vicinity. This time to reach a steady state from a sustained release of molecules is consistent with the simulation data for sustained Glut release >10 μm from the sensor surface. Further modeling of this system could be accomplished with only minor alterations to the models presented here, and this begins to show the value of simulating diffusion and reaction in the vicinity of neurochemical sensors for the analysis of sensor data.

7.5 Conclusion

Simulations of electroenzymatic Glut sensor performance in the brain using 3 dimensional models provided a unique opportunity to consider new probe design modifications to improve sensor performance. Simulation results can be used to guide significant miniaturization and advise for tightly packing sensing sites on the probe, despite the long history of the conventional approach, where much larger sensors are used with large spacings between sensor sites. For guiding miniaturization, the results of Fig. 7.5 are intended to be instructive in determining the relative magnitude of expected sensor response *in vivo*, which could be

compared to experimental magnitudes of noise that may be expected; sensors must have a response that is clearly distinguishable above the noise. Miniaturization shows clear benefits in sensitivity, deviating from the linear trend of response to electrode size by a factor of 2 for sensors with 5 μm radii, and shows that stamping enzyme precisely onto probe locations is beneficial for electroenzymatic sensing relative to large-scale deposition onto the probe surface: although large amounts of enzyme overlap can increase sensor response, a good stamping method that prints enzyme layers with 2 μm overlap results in similar sensitivities and may be preferable because it allows for different enzymes to be stamped onto different sensor sites, affects natural Glut levels less, and reduces H_2O_2 concentrations in the brain. Overall, when choosing an ideal electrode size and spacing, noise concerns must be addressed, although this can be difficult to predict since sensors require a number of coatings that may affect the noise.

Simulations of sensors responding to smaller scale Glut releases further showed the potential benefits of miniaturization, providing much more accurate detection of smaller amounts of Glut release and similar functionality for larger scale release. In considering smaller scale release, models explicitly defined the number of synapses exhibiting an increased firing rate within their representative volumes, showing the number of synapses that are generally being monitored by 5 μm and 25 μm sensors. Although simplifications were made in designating these regions of increased activity (namely that the aspect ratio of this region was preserved for varied synapse numbers) the results are informative and indicate how the shape of a region experiencing increased neural activity can also define the neurotransmitter concentrations that are reached within that space. It would be interesting to model regions of differently shaped systems of excited synapses to determine normal concentration gradients reached for more specific activities or stimulations. The more immediate further use of these models should be for the further analysis of real sensor data, particularly within the context of controlled injections so that model parameters in the brain (within the immediate vicinity of a particular location in the brain) can be narrowed and models can make more specific predictions.

7.6 References

1. Clark, H.; Monaghan, J.; Yang, H. R.; Xia, J. F.; Mu, M.; Lovely, A.; Micovic, N., SPARC_A DNA-based optical nanosensor for in vivo imaging of acetylcholine in the peripheral nervous system. *Faseb J* **2020,** *34*.
2. Marvin, J. S.; Borghuis, B. G.; Tian, L.; Cichon, J.; Harnett, M. T.; Akerboom, J.; Gordus, A.; Renninger, S. L.; Chen, T. W.; Bargmann, C. I.; Orger, M. B.; Schreiter, E. R.; Demb, J. B.; Gan, W. B.; Hires, S. A.; Looger, L. L., An optimized fluorescent probe for visualizing glutamate neurotransmission. *Nat Methods* **2013,** *10* (2), 162-170.
3. Weltin, A.; Kieninger, J.; Urban, G. A., Microfabricated, amperometric, enzyme-based biosensors for in vivo applications. *Anal Bioanal Chem* **2016,** *408* (17), 4503-4521.
4. Huang, I. W.; Clay, M.; Wang, S.; Guo, Y.; Nie, J.; Monbouquette, H. G., Electroenzymatic glutamate sensing at near the theoretical performance limit. *Analyst* **2020,** *145* (7), 2602-2611.
5. Hong, G. S.; Lieber, C. M., Novel electrode technologies for neural recordings (vol 20, pg 330, 2019). *Nat Rev Neurosci* **2019,** *20* (6), 376-376.
6. Clay, M.; Monbouquette, H. G., A Detailed Model of Electroenzymatic Glutamate Biosensors To Aid in Sensor Optimization and in Applications in Vivo. *ACS Chem Neurosci* **2018,** *9* (2), 241-251.
7. Buk, V.; Pemble, M. E., A highly sensitive glucose biosensor based on a micro disk array electrode design modified with carbon quantum dots and gold nanoparticles. *Electrochim Acta* **2019,** *298*, 97-105.
8. Nicholson, C.; Hrabetova, S., Brain Extracellular Space: The Final Frontier of Neuroscience. *Biophys J* **2017,** *113* (10), 2133-2142.
9. Burmeister, J. J.; Davis, V. A.; Quintero, J. E.; Pomerleau, F.; Huettl, P.; Gerhardt, G. A., Glutaraldehyde Cross-Linked Glutamate Oxidase Coated Microelectrode Arrays:

Selectivity and Resting Levels of Glutamate in the CNS. *Acs Chemical Neuroscience* **2013,** *4* (5), 721-728.

10. Schuz, A.; Palm, G., Density of Neurons and Synapses in the Cerebral-Cortex of the Mouse. *J Comp Neurol* **1989,** *286* (4), 442-455.
11. Riveros, N.; Fiedler, J.; Lagos, N.; Munoz, C.; Orrego, F., Glutamate in Rat-Brain Cortex Synaptic Vesicles - Influence of the Vesicle Isolation Procedure. *Brain Res* **1986,** *386* (1-2), 405-408.
12. Wang, B.; Wen, X.; Cao, Y.; Huang, S.; Lam, H. A.; Liu, T. L.; Chung, P. S.; Monbouquette, H. G.; Chiou, P. Y.; Maidment, N. T., An implantable multifunctional neural microprobe for simultaneous multi-analyte sensing and chemical delivery. *Lab Chip* **2020,** *20* (8), 1390-1397.
13. Bard, A. J., and Faulkner, L. R., *Electrochemical Methods: Fundamentals and Applications*. 2nd ed. ed.; Wiley: New York, 2001.
14. Tolosa, V. M.; Wassum, K. M.; Maidment, N. T.; Monbouquette, H. G., Electrochemically deposited iridium oxide reference electrode integrated with an electroenzymatic glutamate sensor on a multielectrode array microprobe. *Biosens Bioelectron* **2013,** *42*, 256-260.
15. Wassum, K. M.; Tolosa, V. M.; Tseng, T. C.; Balleine, B. W.; Monbouquette, H. G.; Maidment, N. T., Transient Extracellular Glutamate Events in the Basolateral Amygdala Track Reward-Seeking Actions. *J Neurosci* **2012,** *32* (8), 2734-2746.
16. Marblestone, A. H.; Zamft, B. M.; Maguire, Y. G.; Shapiro, M. G.; Cybulski, T. R.; Glaser, J. I.; Amodei, D.; Stranges, P. B.; Kalhor, R.; Dalrymple, D. A.; Seo, D.; Alon, E.; Maharbiz, M. M.; Carmena, J. M.; Rabaey, J. M.; Boyden, E. S.; Church, G. M.; Kording, K. P., Physical principles for scalable neural recording. *Front Comput Neurosci* **2013,** *7*, 137.

17. Aharoni, D.; Khakh, B. S.; Silva, A. J.; Golshani, P., All the light that we can see: a new era in miniaturized microscopy. *Nat Methods* **2019,** *16* (1), 11-13.

Chapter 8: Recommendations for future work

8.1 Experimental investigation of sensor response time

As outlined in Chapter 4, it would be of great value to confirm experimentally the cause of the differences between simulated and observed glutamate (Glut) sensor response times. A precise understanding of how the sensor responds to transient Glut is necessary for proper data analysis and an accurate understanding of neurochemical dynamics, as highlighted in Chapters 2, 6, and 7. Confirmation of the hypothesized phenomenon of noncatalytic adsorption of Glut onto the surfaces of the proteins in the enzyme layer (and its significance) will lead to sensor models that are fully consistent with existing electroenzymatic Glut sensors. Furthermore, after confirming the cause of an order-of-magnitude increase in response time, methods can be developed to mitigate the undesired effects and reduce experimental response times to the theoretical limit of ~8 ms at optimal sensitivity. This may require a simple change in protocol for measuring response times, if it is shown that sugars and other amino acids found in the brain reduce the delay in response time as hypothesized in Section 4.4, or an additional step in sensor fabrication to prevent Glut from binding to the proteins in the enzyme layer.

Choline sensor simulations showed a similar disparity between simulated and observed response times, and a modification of the choline sensor model (originally presented in Chapter 5) to include adsorption of choline to the exposed amino acids in the enzyme layer may similarly resolve the observed response time discrepancy. Improvements to sensor models, including the level of detail required to model response time with full accuracy and the types of parameter verifications presented in Chapter 3, dramatically improve the value of simulations in further work. With additional experimental verifications of the mathematical sensor models, the models become more useful in testing the less well understood dynamics of the brain.

Should these suggested experiments prove fruitful, they may be useful in modeling diffusion more accurately within similar biological domains, such as the brain extracellular space (ECS). This would be particularly useful for modeling diffusion near and within misfolded protein

aggregates in the brain. These types of aggregates are characteristic of a number of neurodegenerative diseases including Alzheimer's disease, Parkinson's disease, Huntington's disease, and Amyotrophic lateral sclerosis (ALS), which continue to be important directions of medical and scientific research.[1]

8.2 Further simulations of electroenzymatic sensors *in vivo*

The simulations of Glut sensors in 3 dimensions (Chapter 7) should mark the beginning of a new era in the analysis of sensor data collected *in vivo* by providing a means to simulate sensor response to precise distributions of activated neurons (and their synapses). With such models, sensor response can be interpreted in terms of the possible numbers, distributions, and firing frequencies of synapses within ~20 μm of the sensor. More detailed models of neurotransmitter release will be required to make these approximations. For example, it may be more realistic to represent neurotransmitter release from many synapses as a number of separately defined source functions applied at each synapse location: by dividing the brain domain into a grid of points, each point could represent a synapse and be given its own equation to describe the neurotransmitters it releases as a function of time. With this approach, release could be simulated as bolus releases at realistic firing patterns and distributions; these methods are likely to reveal the consequences of the simplifications made in Chapter 7, where an average release rate of neurotransmitters was modeled within a volume of space.

The application of such models for real data analysis has been limited thus far, but it is clearly useful in the interpretation of collected data. By coupling these models with experiments designed to test our assumptions about the rates of diffusion, Glut uptake, and H_2O_2 clearance (see Chapters 6 and 7 for the significance of these assumptions), models can be further specialized for the analysis of specific biosensor data (*i.e.*, considering the local diffusion and clearance rates of compounds in the particular region of the brain where a sensor is located). This is a very plausible and exciting future direction thanks to the recent development of

electroenzymatic sensor probes with built-in microfluidic channels for drug (or other chemical compound) delivery at the probe location.[2] Not only does this provide a much less destructive method for chemical delivery directly to the brain by circumventing the need of a separate injection probe, but it gives precise control of the location of the injection, which is vital for determining diffusion and clearance rates.

The model of the brain region alone (without an electroenzymatic sensor) was designed as a simplified system, in both the 1-D and 3-D models, to provide more immediate answers to questions concerning biosensor performance. However, as mentioned in Chapter 7, increased neuronal activity for a brief (or extended) period of time within a particular volume of the brain (not necessarily a cylindrical region, as used in Chapter 7) will result in a local neurotransmitter concentration change that is highly dependent on the size of the region or distribution of excited synapses. The relationship between these distributions and local changes in local neurotransmitter concentrations could be further investigated using images of real neuronal structures (to realistically specify synapse locations within modeled domains). Within these more realistic conditions, we could come to understand much more about how neural firing patterns in distinct regions of the brain produce and regulate important neurochemicals, in states of health, during specific activities (such as addictive or depressed behavior), and in cases of disease and neurological damage.

All of the models presented in this dissertation could also be adapted to represent electroenzymatic sensors for other neurochemicals, with only minor modifications to the relevant parameters (diffusivities, reaction rates, sensor dimensions, and rates of biological clearance mechanisms in the case of *in vivo* simulations). The choline sensor model has already been constructed in one dimension to simulate performance *in vitro* and has proved efficacious for choline sensor optimization (Chapter 5). The application of these methods to glucose sensors (or the elusive electroenzymatic GABA sensor, which first requires the identification of a suitable enzyme) should prove equally useful. It is also reasonable that these methods could aid the

analysis of data collected from other types of sensors, including fluorescence data obtained *via* miniscope devices[3] using genetically encoded indicators or fluorescing nanoparticle sensors.[4-6]

8.3 Probe design modifications and noise limitations

In Chapter 7, simulations showed that sensor miniaturization will lead to more accurate measurements of Glut concentrations in the brain, noise permitting, by increasing the sensitivity (defined in units of nA/μM/cm^2) *in vivo* and improving spatial resolution (smaller sensors are more accurate in detecting Glut released from smaller regions of space in the brain). It was also importantly shown that sensors can be situated very closely on a probe (potentially < 5 μm apart) with little risk of crosstalk between sensor sites. Hopefully, these model results will lead to the experimental development of probes containing many, smaller electroenzymatic sensing sites, as has proven feasible for glucose sensors,[7] but with more closely packed sensing sites to optimize the probe's spatial resolution.

However, the miniaturization of electroenzymatic sensors is limited by the presence of noise, since the amplitude of microsensor response is often a function of electrode size and it must be large enough to be distinct from the background noise. It follows that consideration of noise must become a topic of much greater significance in both sensor development and use. The development of an on-probe iridium oxide reference electrode has significantly reduced experimental noise and should see widespread use; with the miniaturization of sensing sites it will be easier to include a reference electrode on the same probe without significantly reducing the number of sensing sites.

A relatively large body of work regarding the noise of electrochemical sensors has been published by others,[8, 9] but it is possible that the sensor coatings affect the noise of the sensor and it may be best for this optimization to be performed primarily through experiments. Whether through experimental methods or theoretical estimations, it is vital to understand in greater detail the limits that noise imposes on sensor minimization. Further reductions in noise may be

possible with noise filtering techniques, although care must be taken to avoid the loss of important data.

8.4 References

1. Lim, J.; Yue, Z., Neuronal aggregates: formation, clearance, and spreading. *Dev Cell* **2015,** *32* (4), 491-501.
2. Wang, B.; Wen, X.; Cao, Y.; Huang, S.; Lam, H. A.; Liu, T. L.; Chung, P. S.; Monbouquette, H. G.; Chiou, P. Y.; Maidment, N. T., An implantable multifunctional neural microprobe for simultaneous multi-analyte sensing and chemical delivery. *Lab Chip* **2020,** *20* (8), 1390-1397.
3. Aharoni, D.; Khakh, B. S.; Silva, A. J.; Golshani, P., All the light that we can see: a new era in miniaturized microscopy. *Nat Methods* **2019,** *16* (1), 11-13.
4. Clark, H.; Monaghan, J.; Yang, H. R.; Xia, J. F.; Mu, M.; Lovely, A.; Micovic, N., SPARC_A DNA-based optical nanosensor for in vivo imaging of acetylcholine in the peripheral nervous system. *Faseb J* **2020,** *34*.
5. Di, W. J.; Clark, H. A., Optical nanosensors for in vivo physiological chloride detection for monitoring cystic fibrosis treatment. *Anal Methods-Uk* **2020,** *12* (11), 1441-1448.
6. Lin, M. Z.; Schnitzer, M. J., Genetically encoded indicators of neuronal activity. *Nat Neurosci* **2016,** *19* (9), 1142-1153.
7. Buk, V.; Pemble, M. E., A highly sensitive glucose biosensor based on a micro disk array electrode design modified with carbon quantum dots and gold nanoparticles. *Electrochim Acta* **2019,** *298*, 97-105.
8. Hong, G. S.; Lieber, C. M., Novel electrode technologies for neural recordings (vol 20, pg 330, 2019). *Nat Rev Neurosci* **2019,** *20* (6), 376-376.
9. Marblestone, A. H.; Zamft, B. M.; Maguire, Y. G.; Shapiro, M. G.; Cybulski, T. R.; Glaser, J. I.; Amodei, D.; Stranges, P. B.; Kalhor, R.; Dalrymple, D. A.; Seo, D.; Alon,

E.; Maharbiz, M. M.; Carmena, J. M.; Rabaey, J. M.; Boyden, E. S.; Church, G. M.; Kording, K. P., Physical principles for scalable neural recording. *Front Comput Neurosci* **2013,** *7*, 137.

Appendix A: COMSOL inputs for simulating 1-D Glut sensors *in vitro*

The follow appendices outline how to implement the mathematical sensor models in COMSOL Multiphysics, with explanations of particular model parameters used and precise details of how to input the desired set of simulation conditions (including varied sensor parameters or boundary conditions that change partway through the simulation). Example model input screens are shown in Figures A.1, B.1, and C.1.

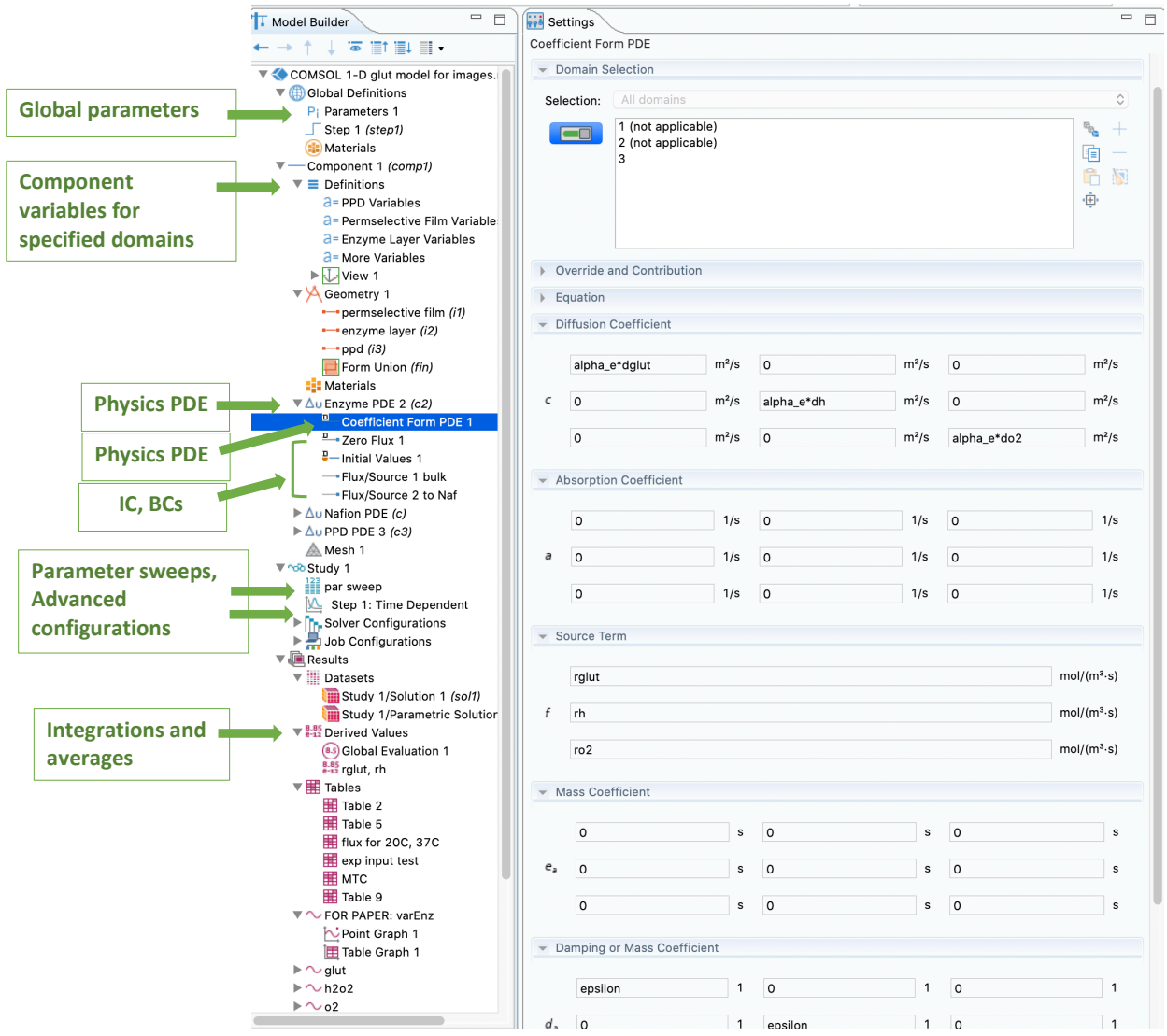

Figure A.1. Example COMSOL interface for 1-D glut sensor simulations *in vitro*. These are the COMSOL windows where model specifics are entered; other windows that will appear include the geometry/plotting window and one for messages/logs/progress/tables.

A.1 COMSOL Physics equations, boundary conditions, and initial conditions

A “coefficient form PDE” physics was added to the model for each sensor coating in these models (for example, “Enzyme PDE 2 (c2) in Fig. A.1); it is also possible to use a single coefficient form PDE physics with additional PDE nodes inset to the physics to describe domains with different diffusion coefficients and porosities. Other physics equations can be added by right-clicking on the file node (“COMSOL 1-D model for images” in Fig. A.1) Including all PDEs within a single physics node will automatically equate fluxes and concentrations at internal boundaries, which is beneficial in the case where no partition coefficients are needed to describe solubility differences in one layer relative to another.

The PDE physics node is where the number and names of dependent variables is specified. Within each PDE sub-node, parameter names or values for diffusion coefficients, etc. can be specified. With multiple variables, parameter inputs will appear as a matrix of inputs; use the diagonals only unless anisotropic conditions must be used. Many of the variables are not needed and can be “zeroed-out” (see the “equation” drop-down menu within the physics specification node to see what each variable refers to in the overall equation).

Initial conditions are straight-forward with no added complications, as long as the correct domains are selected within the “initial values” section. Each physics PDE also requires boundary conditions to be specified; the default setting is a zero flux condition at all external boundaries. For *in vitro* models, the flux to the enzyme is given by a mass transfer coefficient relation, so a flux/source boundary condition is used in COMSOL, which has he form $g - q\mathrm{u}$ where u is the set of dependent variables. In this case, g is the flux coming in and q is what leaves the domain (flux = $gc_i - qu$ for each c_i). In boundary condition equations, dependent variables from the other side of the boundary can be used (i.e., glut_e = glut_naf). If BCs are required between coatings described by a different PDE physics node, it is best to use a flux boundary condition on the outer physics and a Dirichlet BC on the inner one to maintain equal

concentrations and fluxes (this will likely not be necessary in future versions of COMSOL or when using a specialized software package).

Note: it is useful to add a variables list for each domain that has different variable names (i.e. glut_all = glut_enz, h_all = h_enz, o2_all = o2_enz for the enzyme domain) so that results can plot “glut_all” to show glut concentrations in multiple regions. Otherwise, each domain will need its own plot group (see section A.3 Results for more information on plotting results).

To model sensor response to a gaussian-shaped concentration over time at the sensor surface, as was done in Chapter 2, the time dependent equation was used directly as a Dirichlet (constant concentration) boundary condition as defined in Section A.2.

A.2 Parameters and variables

The following parameters, values, and descriptions were used in COMSOL to model 1-D Glut sensors *in vitro* (Chapters 2 and 3), including those used for the models describing noncatalytic Glut adsorption to proteins in the enzyme layer (Chapter 4). They were specified under the “Global Definitions” node in COMSOL (see Fig. A.1). Parameter justifications and references are given in Chapters 2 and 3.

k_glut	0.001 “partition into Nafion”
k_o2	1 “partion”
k_h	1 “partition”
lt	2[μm] "enz thickness"
lf	.071[μm] “Nafion thickness”
lppd	".022 [μm]" “PPD thickness”
glutblk	10[μmol/L]
o2blk	230[μmol/L]
kcat	(1+1.5/.23)*53.2[1/s] “glutox kinetics”
kmglut	(1+1.5/.23)*0.173e-3[mol/L]
kmo2	1.5e-3[mol/L]
ce	"1410*fglutox/70000*(1-epsilon) [mol/L]" “enzyme conc.”
mh	"(0.05) [cm/s]"
F	9.64853e4[C/mol]
area	6000[μm^2]
epsilon	.33
dglut	t37c*7.6e-6[cm^2/s] “diffusivity corrected for 37 C”
do2	t37c*1.92e-5[cm^2/s]
dh	t37c*1.43e-5[cm^2/s]

k1	.357[m^3/mol] “electrooxidation kinetics H_2O_2 on Pt”
k2n	0.00101[mol/(m^2*s)]
k4	.149[m^3/mol]
alpha_p	1/96.1 "permselective film D modification"
glutox	70000
bsa	66500
fglutox	.1 "mass fraction glutox"
nafeps	0.3
pteps	.4
alpha_e	epsilon^2
alpha_ppd	1/735
t37c	1.3355 “correction factor for diffusivity from 20 to 37 C”
enzT	1 ".4 at 20C, .6 at 25C, for modeling enzyme rate at room temp"
kon	"10^6 [1/(mol/L)/s]"
koff	kon*test[mol/L] "was 1.439e7"
aaratio	10 "21 lys, 53 arg, 18 hist"
deltaG	"-18.28 [kJ/mol]"
ceBSA	"1410*(1-fglutox)/bsa*(1-epsilon) [mol/L]"
cetot	ceBSA+ce
p1exp	(t-p1center)^2/(2*sigma^2)
pulsedirichlet	glutblk*(1-pulseon)+pulseon*glutblk*(exp(1)^(-p1exp))
pulseon	1 “used to toggle between a pulse BC and a step-change at t = 0 BC”
glutstickrate	rglut-kon*glut_e*(aaratio*cetot-stuckg)+koff*stuckg
glutunstick	kon*glut_e*(aaratio*cetot-stuckg)-koff*stuckg
aaratio	10
deltaG	-18.28 [kJ/mol]
ceBSA	1410*(1-fglutox)/bsa*(1-epsilon) [mol/L]
cetot	ceBSA+ce

The following were defined as variables within the “Component 1” node. These could also be defined under the “Global Definitions” node, but defining them within the component node allows for different sets of variables to be assigned to different domains, which is useful for setting a local Glut concentration equal to a glut_all variable so that plots of glut_all will provide all of the calculated results for Glut.

rglut	-(enzT)*kcat*ce*glut_e*o2_all/(kmo2*glut_e+o2_e*(glut_e+kmglut))
ro2	rglut
rh	-rglut
mglut	(dglut/dh)^(2/3)*mh
mo2	(do2/dh)^(2/3)*mh
Electroox	pteps*k2n*k1*h_ppd/(1+k1*h_ppd+k4*o2_ppd)
Current	2*F*area*Electroox

A.3 Methods for varying parameters and model configurations

The simplest method for testing how varying 1-2 parameters affects results is to use the parametric sweep (it can be added to study nodes). More parameters can be swept, but results become challenging to display in plots because each set of parameter combinations will need to be specified individually. Sweeps can combine specific combinations of parameter values or every combination. If a sweep changes a parameter used to construct the geometry it will automatically re-mesh, which can be problematic. Sweeps cannot vary component variables, and if a sweep changes the values of something defined as a component variable then the solutions will only keep track of the latest set of parameters.

Another way to change aspects of a simulation (like toggle between boundary conditions) is to use the “modify model configuration for study step” button found in study -> step 1: time dependent. Another node within this section allows for the initial dependent variables to be defined by a previous study step.

A.4 Results and numerical solutions

Creating plots of results is intuitive and details are available within the COMSOL documentation. Right-click on the “Results” node and add the desired plot type. It is then necessary to add a plot group to this new plot node. Multiple plot groups can be added, allowing different visual styles to be completely controlled within each plot group.

A number of notation configurations allow for derivatives of dependent variables to be plotted: for example, f(variable,t) will give the time derivative of a variable and if “glut” is a variable then “glutx” gives the derivative with respect to x. To save a plot for papers and presentations, there are a number of options including the snapshot button. Snapshots can be saved to the clipboard or as a file, and the plot and font sizes can be specified here along with the DPI (image size) and font size. Correctly sizing images can be a guess and check process since image sizes are not always pasted into word documents at the specified dimensions.

To plot, it is necessary to select a data set or table. Data sets are generated automatically, and from these initial results additional sets can be made (for example, a 3-D model can be simplified to a 2-D cross section if a 2-D plot of that cross section is desired).

Tables can be input from outside COMSOL and plotted, as was done in Chapters 3 and 5 to compare theoretical and experimental results, or created within COMSOL. To create a table within COMSOL, right-click on the “Derived Values” node and add the desired type of calculation needed for your table. Settings will appear allowing tabulations of the desired row and column organization.

A.5 Troubleshooting

If there appears to be noise or strange values, refine the mesh or decrease the global tolerance of variables. To change tolerances, go to study -> solver configurations -> time dependent solver.

With multiple, inter-related physics equations it can be necessary to specify that a fully coupled solver is used This is also found within the time dependent solver node.

Some of the steps are simplified if built-in packages are used; note that the free versions can have limited functionality or modifications available. Some processes are very difficult to model without using a software package, including Nernst-Plank-Poisson equations where diffusion, reactions, and electrophoretic mobility can be modeled. Fluid flow with mass transfer is also difficult to model with the mathematical PDEs provided in the basic package.

Appendix B: COMSOL inputs for simulating choline sensors *in vitro*

The same model implementation, solution methods, and results formatting from Appendix A also apply to the 1-D choline sensor simulations used in Chapter 5. New variables and parameters were needed to model choline diffusion and the reaction catalyzed by choline oxidase within the enzyme layer, as follows:

kcatA	(1+kmo2A/207[µmol/L])*16.3 [1/s]
kmA	(1+kmo2A/207[µmol/L])*.87e-3[mol/L]
kmo2A	1e-3 [mol/L]
ce	(1000*1.41*fcholox*(1-enzeps)/chox) [mol/L]
dchol	t37c*1.36e-5[cm^2/s]

Parameter justifications and references are given in Chapter 5. The enzyme reaction rate was specified as a variable with the following input:

rchol	-kcatA*ce*chol_e*o2_e/(chol_e*kmo2A+kmA*o2_e+chol_e*o2_e)
ro2	2*rchol
rh	-2*rchol

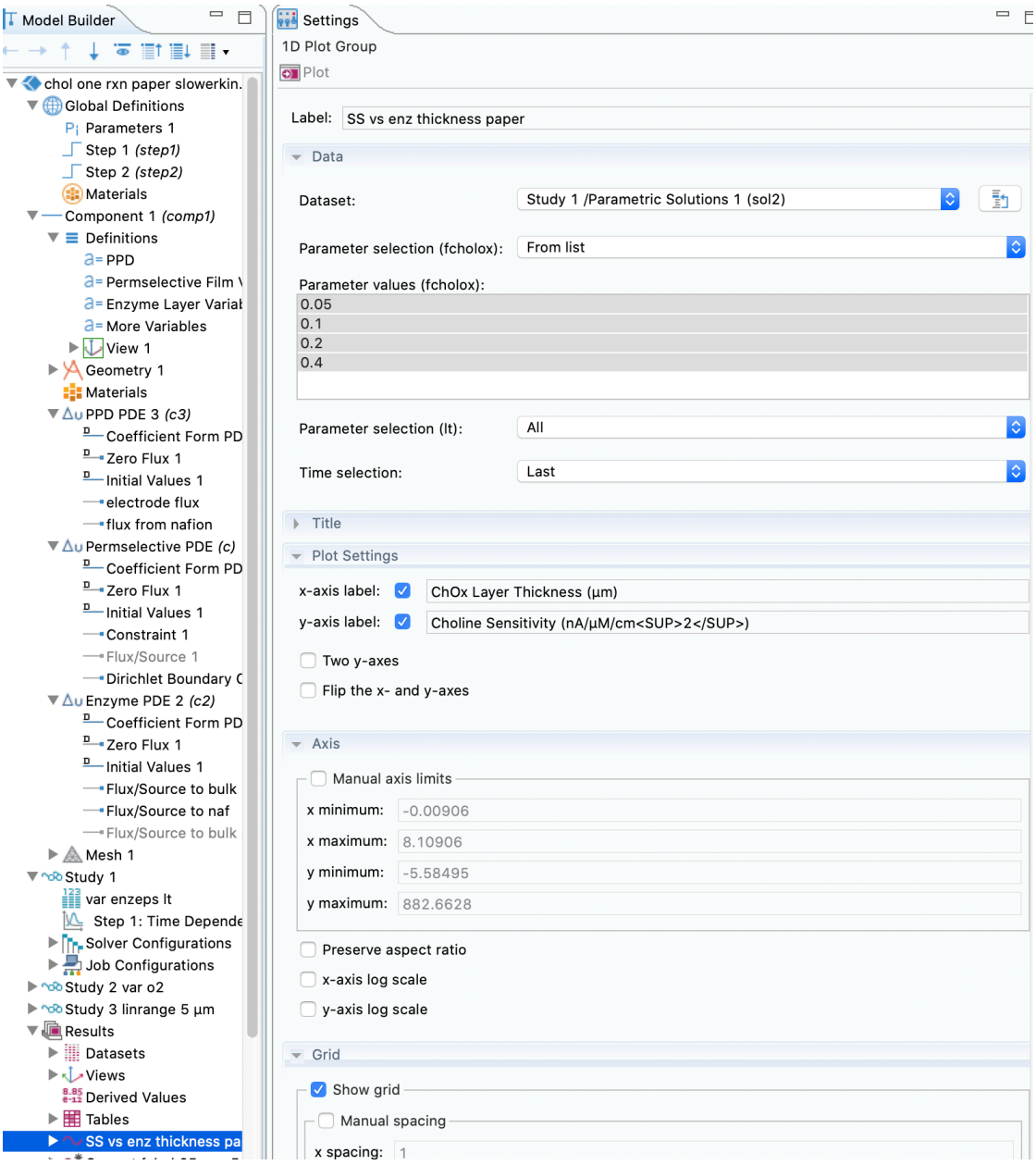

Figure B.1. Physics and condition nodes used to simulate choline sensors *in vitro*. Nodes in light gray are disabled and not used.

Appendix C: 1-D *in vivo* simulations

C.1 New parameters

As detailed in Chapters 6 and 7, a number of new parameters are needed to model diffusion and reactions within the brain ECS. As was done for the other models (see Appendices A and B), parameters were defined under “Global Definitions.”

The new parameters used, including important geometric definitions, are as follows:

alphab	beps/2.56	"modification to diffusivity in the brain"
beps	.2	"void fraction in brai tissue"
vg	4.33[1/s]	"glut uptake rate in the brain"
vh	".0116 [1/s]"	"h2o2 clearance rate in the brain"
glutrelzone	(synapses*1.5873/(pi/2))^(1/3)[µm]	"defines zone of release (Ch 7)"
glutreldist	1[µm]	"distance from sensor to glut source"
rbrain	rsensor+overlap+50[µm]	“radius of brain region domain"
overlap	2[µm]	"for 3-D models. See Chapter 7"
correction	6.0445	"Used in 3-D models to correct the initial concentration for bolus release"
Hz	"10 [1/s]"	
reldens	"(6.3e14*3640/(6.022*10^23)) [mol/L]"	"synapse density*molecules per vesicle*molconversion"
synapses	25	
glutsourceterm	-vg*glutb*beps+reldens*Hz	

C.2 1-D models

Models of sensors *in vivo* in 1-D were constructed from the 1-D model files (see Appendix A) with the addition of another physics domain representing the brain. Descriptions of the equations used are provided in Chapter 6. To model response to a constant Glut concentration at a specified distance, a Dirichlet (constant concentration) boundary condition was used. In the simulations where this boundary was present for a limited time, the simulation was run until the condition needed to be removed. This result was stored as the result from “Study 1”. A second study was added to carry out simulations for the following time period, where the Dirichlet condition was removed. This was done by modifying the model for the study step, as described in Section A.3.

C.3 3-D models

COMSOL models in 3 dimensions must be specified upon creating a file, and will automatically suggest physics equations that use those dimensions. In 3-D, some of the model parameters will be in the form of a matrix, including the dependent variables (defined in Fig. C.1 as glutb, o2b, and hb). In these models, the solver would not converge with each domain being represented by a separate physics, but when the enzyme PDE was incorporated into the brain PDE physics node, “Brain PDE 4 (c4)” the solver had no trouble.

Correctly meshing the sensor and brain is vital to prevent mathematical artifacts from obscuring results in strange places (for example a dip into negative concentrations for the 3rd though 6th time steps) and for reasonable calculation times. Incorrect meshing will result in an end to the simulation; this may occur during a parameter sweep if the sweep changes a geometric parameter and causing re-meshing.

When inputting mesh instructions, the default setting will mesh every domain with the specified element sizing (fine, normal, coarse, etc.). For customized meshing, the online videos from COMSOL are helpful for particular situations. Custom meshing instructions perform the mesh commands sequentially from the top. For the simulations performed in Chapter 7, the thin sensor coatings needed special meshing instructions due to their extreme aspect ratio. This is best done by meshing these regions first, by a triangular mesh on the electrode surface followed by a sweeping mesh upwards, through the sensor coatings. This meshes with the desired mesh density on the base and a desired number of elements going vertically (I used 3 vertical elements per swept domain).

Some parameter changes required different meshes. For example, for modeling sensors with a large “overlap” parameter, the swept mesh didn’t work. In these cases a free tetrahedral mesh through this domain solved the meshing issue without adding too many elements.

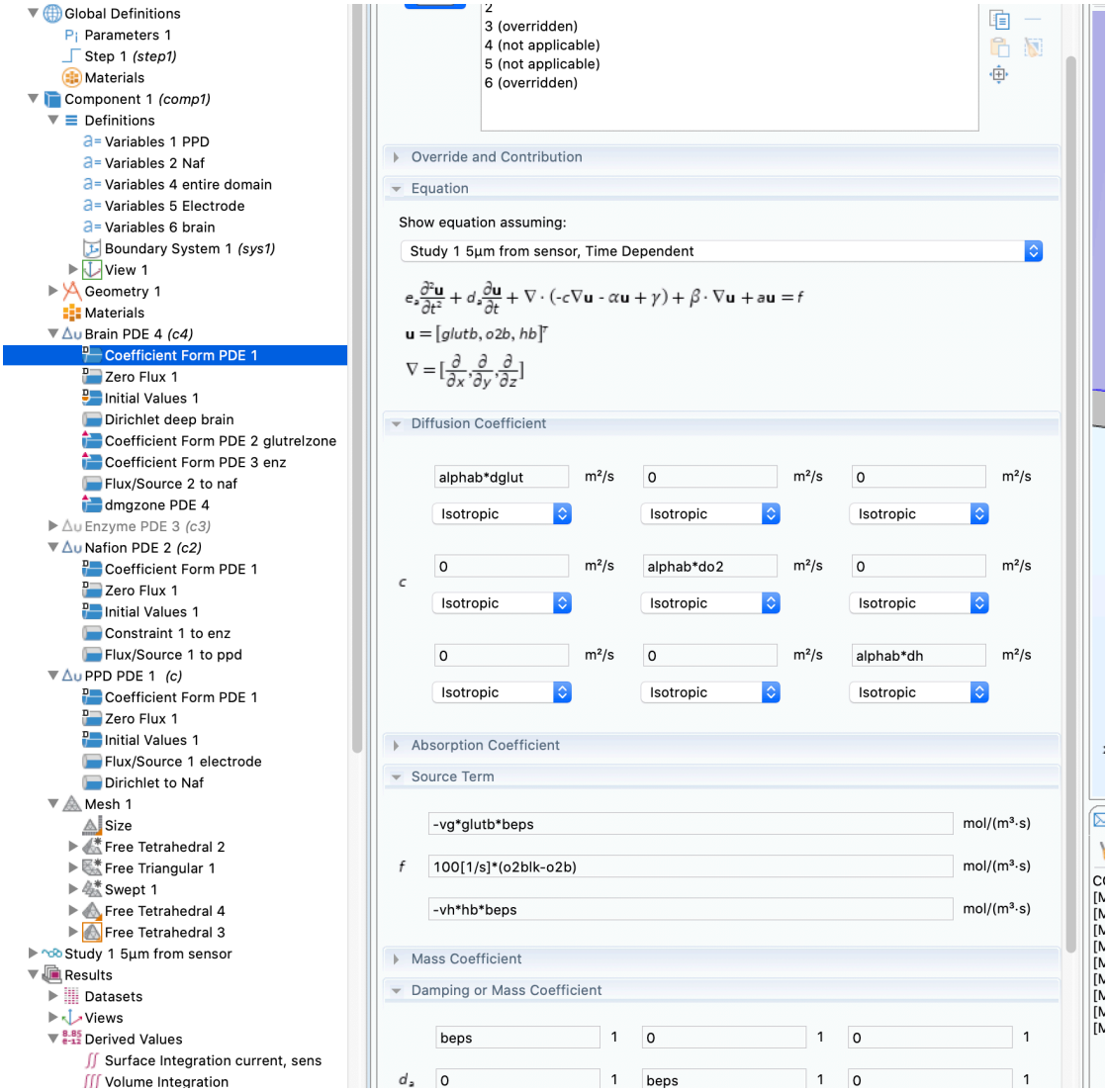

Figure C.1. Sample COMSOL input screen for 3-D simulations *in vivo*.